

UiO : **University of Oslo**

Faculty of Mathematics and Natural Sciences
Department of Physics

Structural investigation of a Ni-Nb-O
phase by electron diffraction
Therese Sørheim Stokkan

Thesis submitted for the degree of
Master of Science in Materials, Energy and
Nanotechnology
December 8th 2011



Preface

This thesis is submitted to the Department of Physics, University of Oslo, in partial fulfilment of the requirements for the degree of Master of Science in Materials, Energy and Nanotechnology. The work was carried out at the Department of Physics, University of Oslo, during the period august 2008 to December 2011, including one year of maternity leave. A six months extension was also granted because of the new family situation.

First of all I would like to thank my main supervisor, Anette E. Gunnæs, for guidance and motivation. This thesis would not have been finished without her. I would also like to thank my two co-supervisors, Despoina Maria Kepaptsoglou for help with TEM work and Anna Magrasó for providing the sample and the basis for the thesis. Thanks also to Ole Bjørn Karlsen for technical support regarding the TEM, Arne Olsen for help with crystallography and Davina Bayless and Charlotte Kristensen for translating German articles.

A special thanks to my parents, Katy Sørheim and Bjørnar Stokkan, for their unconditional love and support through my years of education.

Last but not least, thanks to my two boys. Thank you Magnus for your support and encouragement, and for taking care of home and child during the last period before deadline. Thank you Odin for tolerating so well that “mummy needs to work a lot”. Now I’m finished, darling.

Therese Sørheim Stokkan

Oslo, December 8th 2011.

Abstract

Recent studies by Magrasó et al. show that phase segregation occurs in LaNbO₄-NiO composites due to a reaction between NiO and either of the non-stoichiometric phases of LaNbO₄, La₃NbO₇ or LaNb₃O₉. It was shown that when annealed at temperatures above 1300 °C, LaNb₃O₉ reacts with NiO to form a Ni-Nb-O phase with Ni:Nb ratio between 2 and 3. Based on EDS and XRD analysis, the structure Ni₄Nb₂O₉ with space group *Pcan* was suggested for this phase. However, the refinement of this structure did not fully match the observed XRD pattern, and further investigations were necessary to determine the structure of the phase.

In the present project samples from reaction-sintered pellets of LaNb₃O₉ and NiO annealed at 1300 °C were examined by selected area electron diffraction and EDS. Apart from the phases of NiO and LaNbO₄ that are present in the sample, all the grains analysed have composition Ni-Nb-O with Ni:Nb ratio 2-3. This seems to be uniform throughout the sample, suggesting a single Ni-Nb-O phase. However, three orthorhombic structures have been identified by SAD tilt series analysis:

Structure A: Lattice parameters $a = 5.04 \text{ \AA}$, $b = 9.00 \text{ \AA}$ and $c = 14.20 \text{ \AA}$. Possible space groups *Pmm2* and *Pmmm*.

Structure B: Lattice parameters $a = 10.14 \text{ \AA}$, $b = 14.17 \text{ \AA}$ and $c = 17.51 \text{ \AA}$ according to tilt series B. However, the reciprocal lattice may be a combination of more than one single crystal sharing some of the same lattice points. This phase appeared to be the most abundant.

Structure C: Lattice parameters $a = 5.51 \text{ \AA}$, $b = 7.61 \text{ \AA}$ and $c = 11.30 \text{ \AA}$. Possible space groups: *Pmc2₁*, *Pma2* and *Pmma*.

Neither structure agrees with *Pcan*.

List of Abbreviations

Å	Ångström
At%	Atomic percentage
BSE	Back Scattered Electrons
CBED	Convergent Beam Electron Diffraction
DP	Diffraction Pattern
ED	Electron Diffraction
EDS	Energy Dispersive Spectroscopy
EELS	Electron Energy Loss Spectroscopy
EPMA	Electron Probe Micro Analysis
FCC	Face Centred Cubic
FEG	Field Emission Gun
FOLZ	First Order Laue Zone
HOLZ	High Order Laue Zone
HRTEM	High Resolution Transmission Electron Microscopy/Microscope
JEM	JEOL Electron Microscope
JEOL	Japanese Electron Optics Laboratory Co., Ltd
LCNO	$\text{La}_{0.995}\text{Ca}_{0.005}\text{NbO}_4$
NSS	Noran System Six
PC-SOFC	Proton-Conducting Solid Oxide Fuel Cell
rpm	Revolutions per minute
S/cm	Siemens/cm
SAD	Selected Area Diffraction

SADP	Selected Area Diffraction Pattern
SAED	Selected Area Electron Diffraction
SE	Secondary Electrons
SEM	Scanning Electron Microscopy/Microscope
SOFC	Solid Oxide Fuel Cell
SOLZ	Second Order Laue Zone
TEC	Thermal Expansion Coefficient
TEM	Transmission Electron Microscopy/Microscope
XRD	X-Ray Diffraction
XRDP	X-Ray Diffraction Pattern
ZOLZ	Zero Order Laue Zone

Table of Contents

Preface.....	iii
Abstract.....	v
List of Abbreviations.....	vii
Table of Contents.....	ix
List of Figures	xiii
List of Tables.....	xvii
1 Introduction	1
2 Background and motivation	7
2.1 Compatibility between NiO and niobate phases	7
2.2 Reported structures for Ni ₄ Nb ₂ O ₉	12
2.3 Preliminary electron diffraction analysis.....	15
3 An introduction to crystallography.....	17
3.1 Lattice properties of crystals	17
3.1.1 Vector lattice.....	17
3.1.2 Point lattice.....	18
3.1.3 Unit cell.....	18
3.1.4 The reciprocal lattice	19
3.2 Classifications of space groups	20
3.2.1 Symmetry	20
3.2.2 Space groups, point groups and Bravais lattices	21
3.2.3 Reflection conditions	25
3.2.4 Space group notation	27
3.3 Lattice planes and directions	29
4 Diffraction by X-rays and electrons	31
4.1 The Laue equations and Bragg's law.....	32
4.2 The Ewald sphere.....	35

4.3	Kinematic and dynamic intensities	37
4.3.1	Umweganregung	38
5	Experimental techniques and procedure.....	39
5.1	Transmission Electron Microscopy (TEM).....	39
5.1.1	Diffraction techniques	41
5.1.1.1	Selected area electron diffraction.....	42
5.1.2	SAD tilt series	43
5.1.2.1	Calculating tilt angles.....	44
5.1.3	Sample preparation	45
5.1.3.1	Crushing	46
5.1.3.2	Ion milling	46
5.1.4	Instrumentation	46
5.1.5	Silicon as a standard	47
5.1.5.1	Calibration	47
5.1.5.2	Tilt series	48
5.1.6	Electron diffraction of NiLN3-1300.....	55
5.2	Compositional analysis with TEM and SEM.....	55
5.2.1	EDS spot analysis and element mapping with SEM.....	56
5.2.2	EDS spot analysis with TEM.....	58
6	Results and discussion.....	60
6.1	Compositional analysis.....	60
6.2	Identifying the lattice - tilt series analysis	64
6.2.1	Tilt series A	64
6.2.2	Tilt series B	69
6.2.3	Tilt series C.....	73
6.3	Discussion.....	77
7	Conclusions.....	83
8	Suggestion for further work	84
9	References	85
	Appendix A: Structural data.....	89
A.1	<i>Cc2e</i> (no. 42).....	89
A.2	<i>Fdd2</i> (no. 43).....	91

A.3 <i>Pbcn</i> (no. 60).....	93
A.4 <i>Ccme</i> (no. 64)	95
Appendix C: Quantitative EDS data from TEM.....	97

List of Figures

Figure 1.1: Concept diagram of conventional SOFC with oxygen ion conducting electrolyte [3].	2
Figure 1.2: Concept diagram of a proton-conducting SOFC [3].	3
Figure 1.3: Total conductivity of $\text{La}_{0.99}\text{Ca}_{0.01}\text{NbO}_4$ in various atmospheres as a function of $1/T$ [7].	5
Figure 2.1: (a) SEM micrograph of the electrode rim; the inset shows magnification of the secondary phase, (b) photograph of a screen-printed NiO-LCNO composite on a LCNO electrolyte support annealed at 1250 °C, and (c) SEM micrograph of the NiO-LCNO composite [12].	7
Figure 2.2: XRD patterns of single phase LaNb_3O_9 (i) and reaction sintered LaNb_3O_9 and NiO annealed at 1200 °C (ii) and 1300 °C (iii).	9
Figure 2.3: SEM micrographs of reaction sintered LaNb_3O_9 and NiO after annealing at 1200 °C (a), 1300 °C (b) and 1400 °C (c).	9
Figure 2.4: $\text{La}_2\text{O}_3 - \text{NiO} - \text{Nb}_2\text{O}_5$ phase diagram at 1250 °C, modified from Tolchard et al. [9].	10
Figure 2.5: Close-up section of the XRD pattern of reaction sintered LaNb_3O_9 and NiO annealed at 1300 °C. Top: The observed peaks are shifted relative to the Bragg position of the 200 and 130 peaks for the refined structure. Bottom: Extra peaks at $d = 3.022 \text{ \AA}$ and $d = 3.069 \text{ \AA}$.	11
Figure 2.6: Phase diagram of the Nb_2O_5 -NiO system [16]. The structure of $\text{Ni}_4\text{Nb}_2\text{O}_9$ forms in a wide temperature range (1275 °C – 1510 °C), and has a compositional range of about 3 mol% (shaded).	12
Figure 2.7: Ball-and-stick models [19] of the structures for $\text{Ni}_4\text{Nb}_2\text{O}_9$ reported by Wichmann et al.: I- $\text{Ni}_4\text{Nb}_2\text{O}_9$ (left) [17] and II- $\text{Ni}_4\text{Nb}_2\text{O}_9$ (right) [18].	14
Figure 2.8: The diffraction pattern of Ni-Nb-O phase (middle) indexed according to $\text{Ni}_4\text{Nb}_2\text{O}_9$ with space group Fd2d (a) and Pcan (b). The corresponding simulated diffraction patterns along the [100] zone axis (right) reveals reflections that are absent in the experimental pattern. The figures on the left indicate in which directions R_1 , R_2 and R_3 were measured.	16
Figure 3.1: Unit cell with base vectors a , b and c and inter-axial angles α , β and γ indicated.	19
Figure 3.2: Planes with their respective Miller indices.	29
Figure 4.1: Schematic drawing of two-slit diffraction with visible light [23].	31
Figure 4.2: Schematic drawing of a plane wave, with wave length λ , scattered by two atoms (B and C) a distance a apart. The wave is incident at an angle θ_1 and scattered at an angle θ_2 , and the path difference between the waves is $AB - CD$.	33
Figure 4.3: Schematic illustration of the Bragg diffraction of a plane wave with wavelength λ , incident at an angle θ_B to atomic planes of spacing d .	34
Figure 4.4: The Ewald sphere intersecting an array of reciprocal lattice points. The incident and diffracted wave are represented by the wave vectors \mathbf{k}_0 and \mathbf{k} , respectively. The difference	

between these two vectors is \mathbf{g} , the reciprocal lattice-vector, when Bragg's law is satisfied. The lattice points of higher order Laue zones intersected by the face of the sphere are circled. The angle of 2θ is greatly exaggerated for the sake of illustration..... 36

Figure 4.5: A part of the Ewald sphere intersecting elongated reciprocal lattice points, and the resulting diffraction pattern beneath. The elongation of the points and the size of the sphere make intersection of many points and also points from higher order Laue zones possible..... 37

Figure 5.1: Diagram of the Transmission Electron Microscope [26]. 40

Figure 5.2: Simplified ray diagram in a Transmission Electron Microscope. 41

Figure 5.3: Example of selected area diffraction spot pattern from the Si [110] zone axis. 42

Figure 5.4: Illustration of the geometric relation between the camera length L , the measured distance R and the Bragg angle θ_B 43

Figure 5.5: Schematic diagram showing the relative positions of the axes in the two axial systems [27]. The circle indicates the specimen plane..... 44

Figure 5.6: Diffraction patterns of the [100] and [110] planes of silicon. 47

Figure 5.7: SADPs with common row 00/. The kinematically forbidden diffraction spots, 002 and 002 (circled), are visible in some projections due to dynamical effects (multiple scattering). The conditions of Umweganregung for the 002 reflection are shown in the figure in the lower right corner..... 50

Figure 5.8: Relative rotation of diffraction patterns [100] to [110]. 51

Figure 5.9: Tilt series of silicon confirming a cubic structure with space group $Fd\bar{3}m$ and lattice parameter $a = 5.43 \text{ \AA}$ 52

Figure 5.10: Procedure of constructing a model of the reciprocal lattice in Google Sketchup. . 53

Figure 5.11: 3D models of the reciprocal lattice for silicon in (a) parallel view, (b) perspective view and (c) parallel view along the \mathbf{a}^* and \mathbf{b}^* axes. The kinematically forbidden diffraction spots that appeared in the tilt series are coloured black. The grey box marks the outline of the reciprocal unit cell. 54

Figure 5.12: Principle of EDS (left) and example of EDS spectre (right) [30]. 56

Figure 5.13: Schematic figure of excitation volume in the SEM. The general penetration depth of the beam is in the range $1\text{-}5 \mu\text{m}$ [31]. 57

Figure 5.14: BSE image showing the NiLN3-1300 TEM sample. 58

Figure 6.1: BSE image surrounded by colored elemental contrast images of the same area. The brighter the color the more concentration of the specified element. The numbers in the BSE image indicate positions for spot analysis. 61

Figure 6.2: TEM image (a) of area containing spot analysis positions 1 and 2, and SEM BSE image (b) of area containing spot analysis positions 1, 2 and 3. The bright white line is the TEM indicator pointing at position 2. 62

Figure 6.3: SADPs from spot position 1 (a) and 2 (b), and from the [321] zone axis from tilt series B (c). The last pattern is rotated to match the orientation of the other two. The arrows in b indicate the measured distances R_1 , R_2 and R_3 used in the calculation of d-values. 63

Figure 6.4: Tilt series A, revealing an orthorhombic lattice with lattice parameters $a = 5.04 \text{ \AA}$, $b = 9.00 \text{ \AA}$ and $c = 14.20 \text{ \AA}$. Diffraction patterns along the same dashed line are tilted about the same axis, which in turn is indicated by a solid line.	66
Figure 6.5: Top: Model of the reciprocal lattice from tilt series A. The blue box indicates the smallest unit in the orthorhombic lattice. Bottom three from left to right: Parallel view of the lattice along the a^* , b^* and c^* axes.	67
Figure 6.6: The diffraction patterns reveal no systematic extinctions, although many of them are very weak. The lines indicate which patterns are tilted about the same row.	68
Figure 6.7: Left: Diffraction pattern from the $[443]$ zone axis. Some of the FOLZ reflections are circled. Right: View along the $hh0$ row (110 , 220 , etc.) of the $[443]$ zone axis (black dots) in a lattice with parameters $a = 5.04 \text{ \AA}$, $b = 9.00 \text{ \AA}$ and $c = 14.20 \text{ \AA}$	69
Figure 6.8: Tilt series B, consistent with an orthorhombic lattice with lattice parameters $a = 10.14 \text{ \AA}$, $b = 14.17 \text{ \AA}$ and $c = 17.51 \text{ \AA}$. Diffraction patterns along the same dashed line are tilted about the same axis, which in turn is indicated by a solid line.	70
Figure 6.9: Top: Perspective view of the model of the reciprocal lattice from tilt series B. The grey box indicates the smallest unit in the orthorhombic lattice. Bottom three from left to right: Parallel view of the lattice along the a^* , b^* and c^* axes.	71
Figure 6.10: Indexed patterns from tilt series B according to a primitive lattice with lattice parameters $a = 10.14 \text{ \AA}$, $b = 14.17 \text{ \AA}$ and $c = 17.51 \text{ \AA}$	72
Figure 6.11: Tilt series C, revealing an orthorhombic lattice with lattice parameters $a = 5.51 \text{ \AA}$, $b = 7.61 \text{ \AA}$ and $c = 11.30 \text{ \AA}$	74
Figure 6.12: 3D models of the reciprocal lattice based on tilt series C, at slightly different angles. Kinetically forbidden diffraction spots that appeared in the tilt series are coloured black, and kinetically forbidden spots that did not appear are colored dark grey. The lines mark the edges of the reciprocal unit cell.	75
Figure 6.13: Indexed SADPs of the diffraction patterns from the $[010]$ and $[100]$ zone axes. The patterns are tilted about the $00l$ -row, and the absent reflections along this row are indicated with x in $[100]$	76
Figure 6.14: Left: Diffraction pattern from initial electron diffraction analyses. Right: Diffraction pattern from the $[100]$ zone axis of tilt series B. The d -values from the two patterns coincide.	78
Figure 6.15: The diffraction pattern from zone axis $[111]$ from tilt series A. The red arrows represent reciprocal lattice vectors for reflections violating reflection conditions for space group $Pcan$	81
Figure 6.16: Principle of three-fold twinning of orthorhombic crystal. Projection along $[001]$. The short and long side of the rectangles are proportional to 5.0 \AA and 8.8 \AA , respectively.	82

List of Tables

Table 2.1: Characteristic space groups and lattice parameters for I-Ni ₄ Nb ₂ O ₉ and II-Ni ₄ Nb ₂ O ₉ as reported by Wichmann et al. [17, 18].....	13
Table 2.2: <i>d</i> -values from diffraction pattern and corresponding hkl indices for Ni ₄ Nb ₂ O ₉ (Fd2d) and Ni ₄ Nb ₂ O ₉ (Pcan).	15
Table 3.1: Crystal families, crystal systems, conventional coordinate systems and crystallographic point groups.....	23
Table 3.2: The relation between crystal families and crystal systems together with the 14 Bravais lattices. H-M symbols are given in parentheses for the Bravais lattices.....	24
Table 3.3: Conditions limiting possible reflections in the orthorhombic and cubic crystallographic coordinate systems. Conditions that apply only to the cubic one are marked as such, the rest apply to both systems.	26
Table 3.4: Miller notation for planes and directions in real space and reciprocal space	30
Table 5.1: Calibrated camera lengths.....	48
Table 5.2: Calculated and experimental angles between the diffraction planes of the silicon tilt series.	49
Table 6.1: Quantified results from SEM EDS analysis.	61
Table 6.2: Quantified results from TEM EDS analysis.	62
Table 6.3: Measured R-values and lattice distances, <i>d</i> , from spot positions 1 and 2 and from the [321] zone axis from tilt series B.	63
Table 6.4: Calculated and experimental angles between the zone axes in tilt series A.	65
Table 6.5: Calculated and experimental angles between the zone axes in tilt series B.	69
Table 6.6: Calculated and experimental angles between the zone axes in tilt series C.	73
Table 6.7: Lattice parameters from tilt series A, B and C.	77
Table 6.8: Experimental lattice parameters from TEM (structures A and B) and XRD studies of the NiLN3-1300 sample, and the lattice parameters reported for Ni ₄ Nb ₂ O ₉ by Wichmann et al. [18] and Magrasó et al. [12].	79

1 Introduction

The world's population is rapidly increasing and so are the living standards all over the planet, especially in developing countries. One of the challenges we are facing as a result of this is the rapid increase in energy demand. Since approximately 1850, fossil fuels (coal, oil and gas) have been our main source of energy: In 2008 it accounted for 85 % of the total global primary energy supply [1]. Burning of fossil fuels releases large amounts of carbon dioxide (CO₂). Although there is an on-going debate about whether or not human-induced increase in greenhouse gas concentrations contributes to climate change, a lot of effort is put into reducing the emission of such gases (a “better safe than sorry” approach). What is certain is that fossil fuels are limited resources, and that the conventional methods of energy conversion of these sources are highly pollutive. It is therefore clear that we need to develop more efficient and environmentally friendly power generation methods both to exploit the fossil fuels we have left in a better way, as well as to be able to utilize sustainable energy sources such as wind, wave, solar and geothermal power for electricity generation and heating.

The fuel cell is a promising environmentally friendly energy converter. Like a combustion engine, it utilizes chemical fuel to generate electricity, but with higher efficiencies and lower emissions. The higher efficiency is a result of direct conversion of the fuel to electricity and heat, without the combustion step. Fuel cells operate on hydrogen-containing fuel gases (such as pure hydrogen, natural gas, butane, propane, ethanol, diesel etc.), and provide the lowest emissions of any non-renewable power generation method [2]. If the fuel cell is run on pure hydrogen, the only emission is water and heat. This makes the fuel cell an important part of a potential future “hydrogen society”, where hydrogen gas may be produced by the means of solar energy. Unlike electricity, hydrogen gas may be stored until needed. This is a very useful feature, as the daily and annual peaks of energy production and demand seldom coincide.

The main components of a fuel cell are the electrodes (anode and cathode) and the ion-conducting electrolyte. Fuel cells are usually classified by the type of electrolyte in the cell, as this is the main component for determining the operation temperature, type of fuel and hence electrical generation efficiencies.

One of the most promising types of fuel cells, the Solid Oxide Fuel Cell (SOFC), has the potential to be used for commercial electricity-generation as well as for off-grid applications. SOFCs consist of a solid ceramic electrolyte sandwiched between solid electrodes. In classical SOFCs, the electrolytes conduct oxygen ions. Oxygen gas from the air is reduced on the cathode side, and the oxygen ions migrate across the electrolyte to the anode side where they combine with hydrogen from the fuel to form water. The released electrons from the oxidized hydrogen fuel travel through an outer circuit back to the cathode, thereby providing useful electrical power and at the same time maintaining the charge balance (see Figure 1.1).

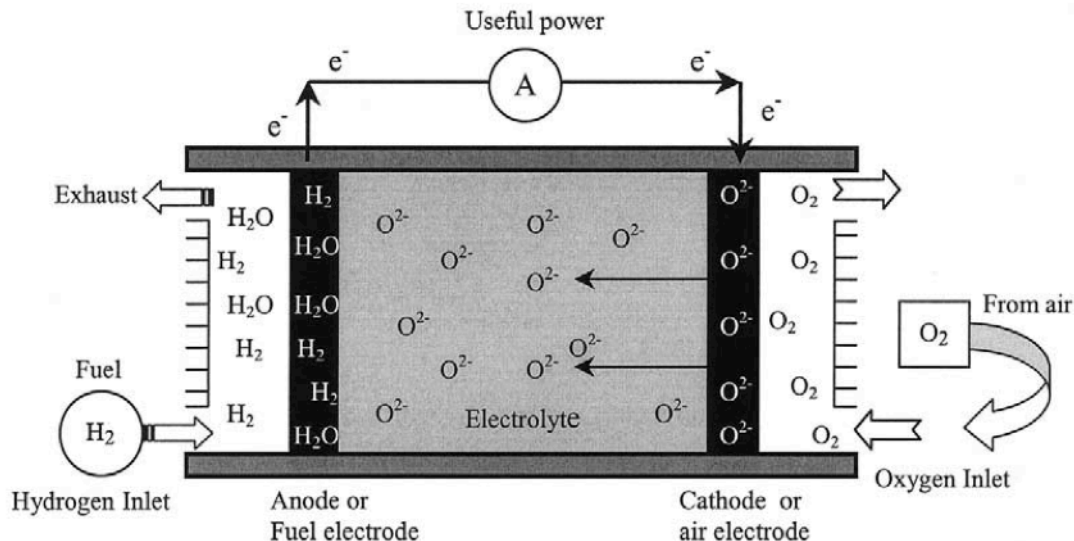


Figure 1.1: Concept diagram of conventional SOFC with oxygen ion conducting electrolyte [3].

Because of the high activation energy of oxygen ion migration and electrode reactions, classical SOFCs need to operate at high temperatures (600-1000 °C). This enables them to reform fuels of heavier hydrocarbons directly in the cell, and due to this they are among the most efficient of the fuel cells with possibilities to reach 70 % efficiency (plus an additional 20 % with heat recovery) [2]. However, the high temperatures lead to problems concerning material stabilization, reducing thus the cell lifetime and increasing the cost of materials. Lowering the operation temperature is therefore a key factor for lowering the cost of the cells. Also, as water is produced at the fuel (anode) side it dilutes the fuel and thereby severely reduce the fuel efficiency, and for nickel-containing anodes there is a risk of it oxidizing the nickel which will reduce the anode lifetime [4].

Proton conducting SOFCs (PC-SOFCs) have emerged as a possible alternative to conventional SOFCs. As the name suggests, the electrolyte in these cells conduct protons (H^+). Hydrogen in the fuel is oxidized at the anode side, travel through the electrolyte and combine with oxygen from air on the cathode side to form water. As with conventional SOFCs, the electrons travel in an outer circuit from the anode to the cathode (Figure 1.2).

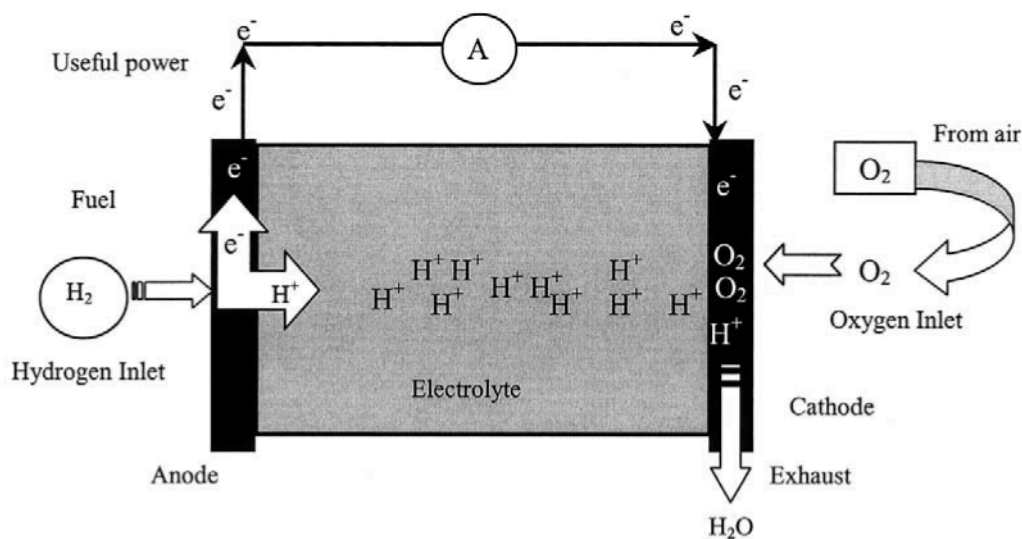


Figure 1.2: Concept diagram of a proton-conducting SOFC [3].

The lower activation energy for the mobility of the protons facilitates lower operation temperatures ($\sim 400\text{--}800\text{ }^{\circ}\text{C}$), and there is no risk of oxidizing the anode or diluting the fuel as water is produced at the cathode side. However, these features lead to other challenges: High porosity of the cathode is needed in order to enable fast gas diffusion to remove the water. Also, as internal reforming requires water at the fuel (anode) side of the cell, this can't be done in a PC-SOFC and carbonaceous fuels need to be pre-reformed. Despite this, PC-SOFCs can compete with SOFCs run on carbonaceous fuels (reference [4] and references therein).

For a PC-SOFC to operate on a long-term basis with reasonable efficiency, the proton-conducting electrolyte should exhibit high proton conductivity, none (or low) electronic conductivity and long-term stability with respect to operating temperatures, atmosphere and adjacent cell components. It also needs to be dense to prevent gas diffusion. The materials showing the best proton conductivities ($\sim 10^{-2}\text{ S/cm}$) are acceptor-doped perovskites with Ba or Sr as main component. Y-doped BaCeO_3 is the so-called benchmark proton conductor, but like the other proton conducting perovskites it suffers from poor chemical stability in CO_2 -containing atmospheres and cannot be used in commercial PC-SOFCs (see reference [5] and references therein). It is therefore of great interest to find more chemically stable proton-conducting materials.

Haugsrud and Norby have investigated acceptor-doped rare-earth ortho-niobates and ortho-tantalates as proton-conducting materials [6, 7]. The highest proton conductivity was found for Ca-doped LaNbO_4 , with a maximum of $\sim 10^{-3}\text{ S/cm}$ at $950\text{ }^{\circ}\text{C}$ for $\text{La}_{0.99}\text{Ca}_{0.01}\text{NbO}_4$ (see Figure 1.3). Although this is an order of magnitude less than for Y-doped BaCeO_3 , LaNbO_4 is stable in CO_2 -containing atmospheres. With these characteristics the material is a good candidate for electrolytes in PC-SOFCs, as long as the electrolyte film thickness is in the order of a few micrometres to minimize electrolyte resistance.

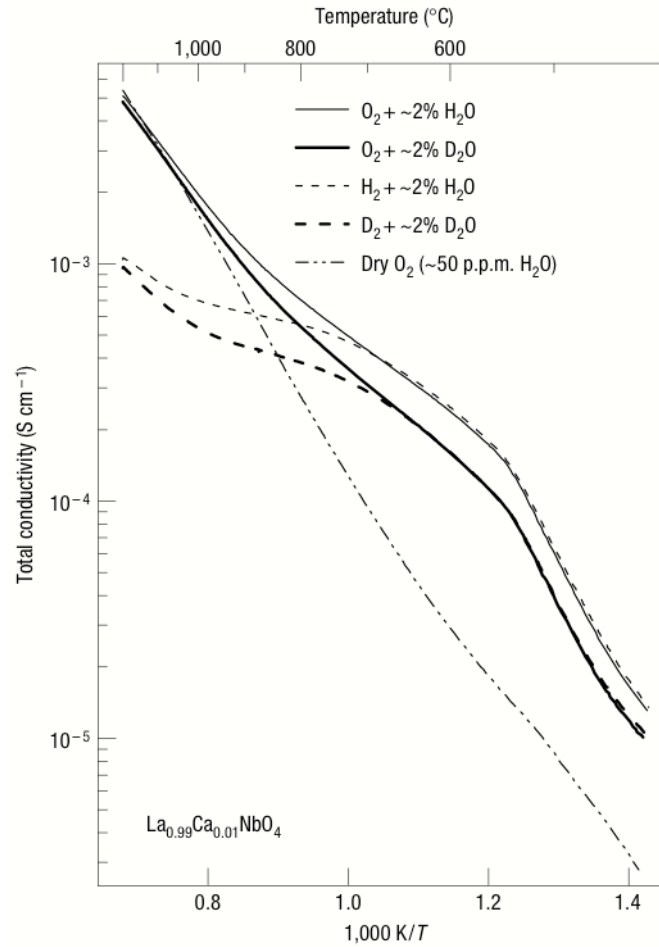


Figure 1.3: Total conductivity of $\text{La}_{0.99}\text{Ca}_{0.01}\text{NbO}_4$ in various atmospheres as a function of $1/T$ [7].

The electrolyte in a fuel cell needs to be compatible with the electrodes with respect to thermal expansion and chemical reactions. As the background for this thesis is the electrolyte compatibility with the anode, only this electrode will be described further. Nickel exhibits the highest electrochemical activity towards oxidation of H_2 , and is thus often used as the main anode component. To match the thermal expansion coefficient (TEC) of the electrolyte and prevent sintering of the metal particles, the anodes are usually ceramic-metallic (cermet) composites of the electrolyte material and nickel. NiO is used during manufacture of the cell, and is reduced to metallic nickel prior to operation [3].

Studies [8-10] show that Ca-doped LaNbO_4 doesn't react with NiO or Ni in the temperature range required for PC-SOFCs. However, LaNbO_4 is a so-called line compound, easily forming La-rich or Nb-rich phases (La_3NbO_7 and LaNb_3O_9 , respectively) [11]. Addition of dopants (such as Ca and Sr) may also lead to formation of secondary phases, and it is important that neither of these phases react with Ni or NiO.

2 Background and motivation

2.1 Compatibility between NiO and niobate phases

The compatibility between NiO and niobate phases in self-supported $\text{La}_{0.995}\text{Ca}_{0.005}\text{NbO}_4$ (LCNO) electrolytes with screen-printed LCNO:NiO electrode composites have recently been studied by Magrasó et al. [12]. The studies showed that phase segregation occurs at the rim of the screen-printed NiO-LCNO composite (see Figure 2.1). To support the investigation and identify the reaction products, reaction sintered pellets of NiO and single phase La_3NbO_7 or LaNb_3O_9 were made and annealed at different temperatures. In this project the focus will be on the high temperature reaction product of LaNb_3O_9 and NiO.

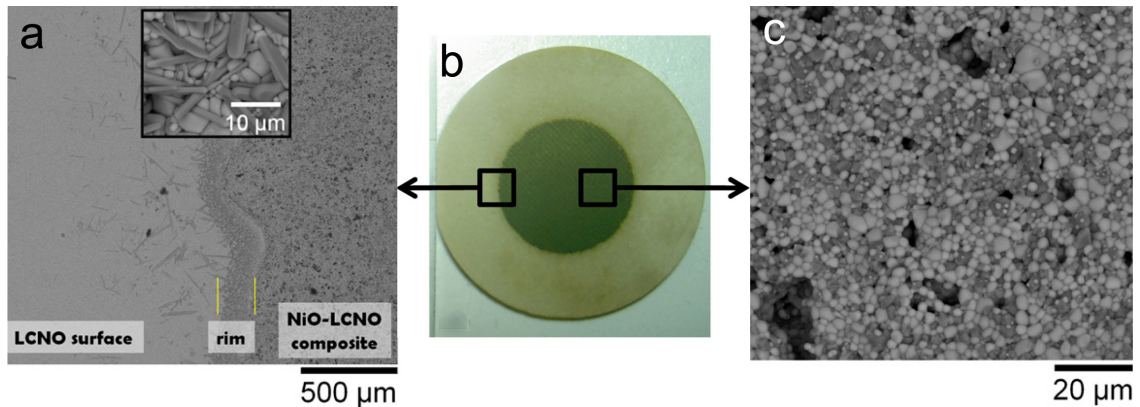


Figure 2.1: (a) SEM micrograph of the electrode rim; the inset shows magnification of the secondary phase, (b) photograph of a screen-printed NiO-LCNO composite on a LCNO electrolyte support annealed at 1250 °C, and (c) SEM micrograph of the NiO-LCNO composite [12].

Pellets of LaNb_3O_9 -NiO were made by reaction sintering of NiO powder (purchased from GFS Chemical) and LaNb_3O_9 (synthesised by solid-state reaction as described in [13]): 50 wt% each of NiO and LaNb_3O_9 were ball-milled in isopropanol for 1 hour at 250 rpm. The powders were then dried, pressed into

pellets and annealed in air at 1200, 1300, 1400 and 1500 °C for 5 h, with both heating and cooling rate of 200 °C/h. The samples were examined by a field emission gun scanning electron microscope (SEM; FEG Quanta 200 FEI) equipped with X-ray energy dispersive spectroscopy (EDS; EDAX) and by X-ray diffraction (XRD; SIEMENS D5000) with monochromatic Cu $K\alpha_1$ radiation. Lattice parameters were obtained by the Le Bail refinement method.

Examinations of the pellets showed the formation of two new secondary phases, one at 1200 °C and another above 1300°C. In the pellet sintered at 1200 °C the phases present were identified by XRD as $NiNb_2O_6$ and $LaNbO_4$ [see Figure 2.2 (ii)]. Above 1300 °C another phase formed, as seen in Figure 2.2 (iii). The XRD analysis was in close agreement with $Ni_4Nb_2O_9$ with space group Pcan (cf. Section 2.2). SEM analysis showed the presence of several phases of different morphologies in each of the samples. In Figure 2.3 (a) the spherical shaped grains correspond to NiO, while the grains with acicular shape contains most Ni and Nb. EDS analysis of these grains gave an Ni:Nb ratio of about 0.5-0.7 (consistent with $NiNb_2O_6$). In Figure 2.3 (b) and (c) the darker phase corresponds to NiO, the white phase to $LaNbO_4$ and the grey phase contain most Ni and Nb, with a Ni:Nb ratio of 2-2.5 (close to $Ni_4Nb_2O_9$) from EDS analysis.

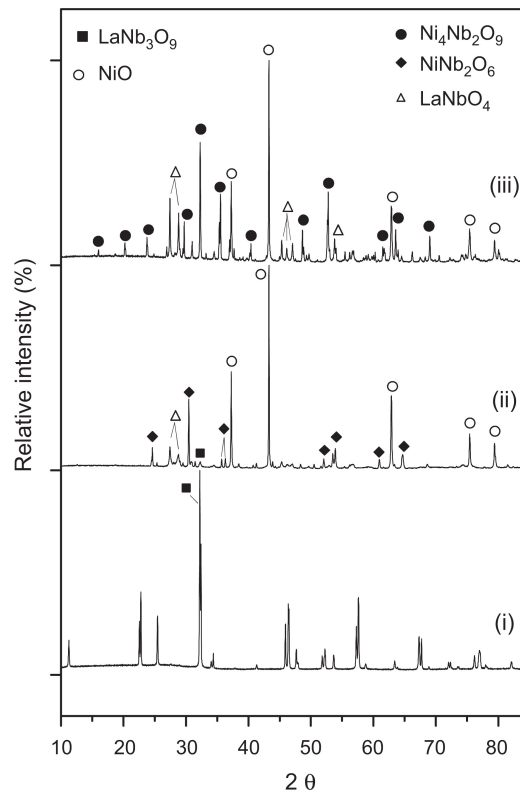


Figure 2.2: XRD patterns of single phase LaNb_3O_9 (i) and reaction sintered LaNb_3O_9 and NiO annealed at 1200 °C (ii) and 1300 °C (iii).

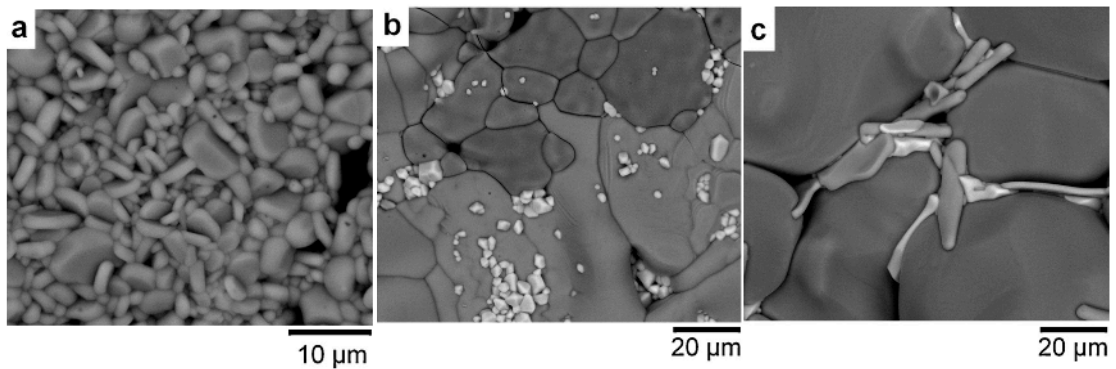


Figure 2.3: SEM micrographs of reaction sintered LaNb_3O_9 and NiO after annealing at 1200 °C (a), 1300 °C (b) and 1400 °C (c).

Based on these results, possible reactions in the LaNb_3O_9 -NiO pellets at the different temperatures are:

At 1200 °C: $\text{LaNb}_3\text{O}_9 + \text{NiO} \rightarrow \text{NiNb}_2\text{O}_6 + \text{LaNbO}_4$

Above 1300 °C: $\text{NiNb}_2\text{O}_6 + 3\text{NiO} \rightarrow \text{Ni}_4\text{Nb}_2\text{O}_9$

These reactions are in accordance with the ternary phase diagram (at 1250 °C) in Figure 2.4.

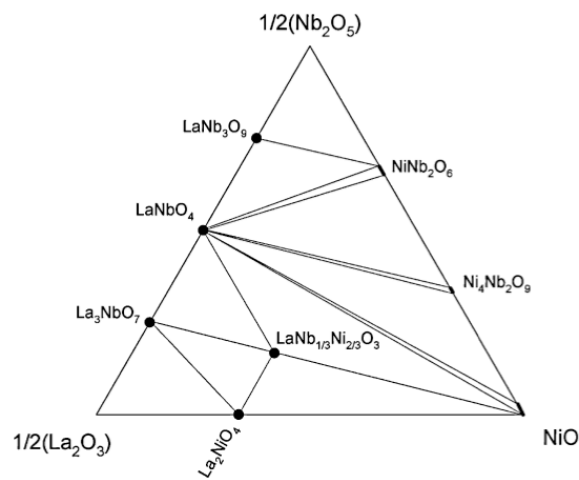


Figure 2.4: La_2O_3 – NiO – Nb_2O_5 phase diagram at 1250 °C, modified from Tolchard et al. [9].

Although the Pcan structure of $\text{Ni}_4\text{Nb}_2\text{O}_9$ seems to be the closest match for the nickel-rich reaction product, the refinement could not completely match the experimental pattern with the theoretical structure. The reported structure has lattice parameters $a = 5.0545 \text{ \AA}$, $b = 8.7688 \text{ \AA}$ and $c = 14.3041 \text{ \AA}$ (cf. Section 2.2), while the lattice parameters from the refinement were determined to be $a = 5.026 \text{ \AA}$, $b = 8.758 \text{ \AA}$ and $c = 14.340 \text{ \AA}$. Close inspection of the XRD pattern shows a poor fit between the observed peaks and the bragg positions of the refined structure. Several peaks are shifted relative to these positions, some expected peaks are absent and there are extra peaks that cannot be assigned to either of the refined structures. Figure 2.5 shows a section of the pattern with

the shifted (200) and (130) peaks, and another section where two extra peaks are visible.

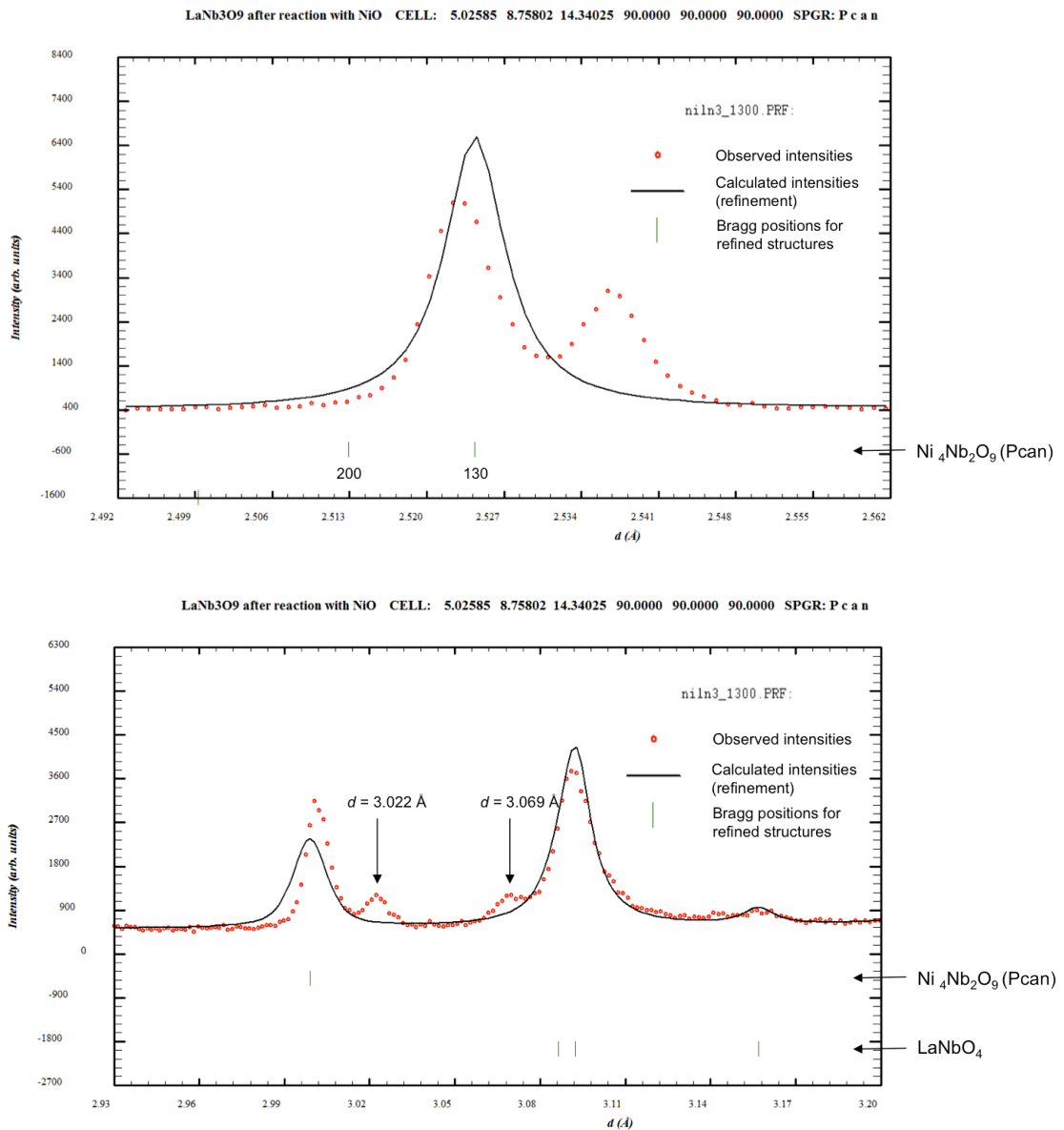


Figure 2.5: Close-up section of the XRD pattern of reaction sintered LaNb₃O₉ and NiO annealed at 1300 °C. Top: The observed peaks are shifted relative to the Bragg position of the 200 and 130 peaks for the refined structure. Bottom: Extra peaks at $d = 3.022 \text{ \AA}$ and $d = 3.069 \text{ \AA}$.

In order to determine the structure of the Ni-Nb-O phase, the sample needs to be examined further. Ni₄Nb₂O₉ is the only reported composition that comes close to the composition of the Ni-Nb-O phase in the sample, and the reported structures for Ni₄Nb₂O₉ are presented in the following section.

2.2 Reported structures for $\text{Ni}_4\text{Nb}_2\text{O}_9$

In 1960 and 1961, Bertaut et al. [14, 15] studied the structures of $\text{A}_2\text{M}_4\text{O}_9$ ($\text{A} = \text{Nb, Ta}$; $\text{M} = \text{Mn, Fe, Co, Ni, Mg}$) by X-ray diffraction. All structures but $\text{Ni}_4\text{Nb}_2\text{O}_9$ were assigned to the hexagonal crystal system. $\text{Ni}_4\text{Nb}_2\text{O}_9$ was described as orthorhombic, with lattice parameters $a = 10.144 \text{ \AA}$, $b = 17.468 \text{ \AA}$ and $c = 14.318 \text{ \AA}$, but was not investigated any further. A few years later, Burdese et al. [16] released an article on the “Systems between niobium and the oxides of nickel and cobalt”, with a phase diagram showing how $\text{Ni}_4\text{Nb}_2\text{O}_9$ forms just below $1300 \text{ }^\circ\text{C}$ (Figure 2.6), in agreement with the findings of Margasó et al. The lattice parameters described for $\text{Ni}_4\text{Nb}_2\text{O}_9$ here are similar to those reported by Bertaut et al.

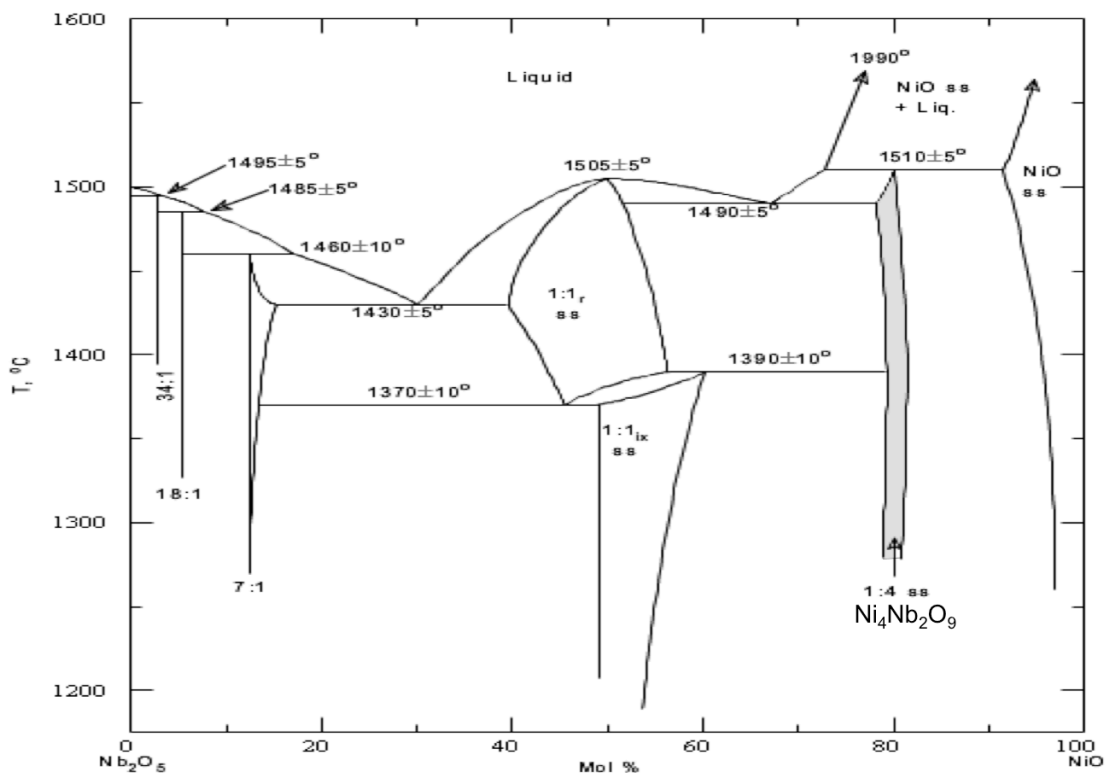


Figure 2.6: Phase diagram of the Nb_2O_5 - NiO system [16]. The structure of $\text{Ni}_4\text{Nb}_2\text{O}_9$ forms in a wide temperature range ($1275 \text{ }^\circ\text{C} - 1510 \text{ }^\circ\text{C}$), and has a compositional range of about 3 mol% (shaded).

In 1985 and 1986, Wichmann et al. described two structures of $\text{Ni}_4\text{Nb}_2\text{O}_9$: I- $\text{Ni}_4\text{Nb}_2\text{O}_9$ [17], and II- $\text{Ni}_4\text{Nb}_2\text{O}_9$ [18], with lattice parameters and characteristic space groups as listed in Table 2.1. The lattice parameters were determined by XRD on single-crystals of $\text{Ni}_4\text{Nb}_2\text{O}_9$, and the characteristic space groups were determined from conditions limiting possible reflections (cf. Section 3.2.1 and 3.2.2) in the diffraction patterns. Ball-and-stick models of the structures are shown in Figure 2.7.

Table 2.1: Characteristic space groups and lattice parameters for I- $\text{Ni}_4\text{Nb}_2\text{O}_9$ and II- $\text{Ni}_4\text{Nb}_2\text{O}_9$ as reported by Wichmann et al. [17, 18].

Structure	Space group	Lattice parameters [Å]		
		a	b	c
I- $\text{Ni}_4\text{Nb}_2\text{O}_9$	Fd2d	10.101(13)	17.5126(51)	28.6364(87)
II- $\text{Ni}_4\text{Nb}_2\text{O}_9$	Pcan	5.0545	8.7688	14.3041

In the study by Wichmann et al., the lattice parameters of II- $\text{Ni}_4\text{Nb}_2\text{O}_9$ were at first found to be consistent with those found by Bertaut et al. and Burdese et al. The conditions limiting possible reflections [(hkl) with $h+k = 2n$, (0kl) with $k = 2n$ and $l = 2n$, (h0l) with $h = 2n$ and (hk0) with $h = 2n$ and $k = 2n$] narrowed it down to the characteristic space groups Ccma and Cc2a (cf. Section 3.2, Classifications of space groups). However, Patterson synthesis with direct methods and Fourier synthesis lead to a crystal structure with unexplainably short metal-metal distances and with unusually strongly distorted octahedrons around these positions. The study concluded that the isolated crystals were threefold twins, with the twin parts rotated 120° relative to each other. To analyze individuals of the twinned crystal, non-superimposed reflections were sorted out from the data set. The axes were corrected to the values in Table 2.1, and the conditions limiting possible reflections for the “pure” crystal [(0kl) with $l = 2n$, (h0l) with $h = 2n$, (hk0) with $h+k = 2n$] lead to the characteristic space group Pcan. The study further concluded that the lattice constants determined by Bertaut et al. shows that their examinations also concerned twinned crystals, and consequently that the only possible space groups for $\text{Ni}_4\text{Nb}_2\text{O}_9$ are I- $\text{Ni}_4\text{Nb}_2\text{O}_9$ (F2d2) and II- $\text{Ni}_4\text{Nb}_2\text{O}_9$ (Pcan).

The difference in the two space groups of $\text{Ni}_4\text{Nb}_2\text{O}_9$ were explained by Wichmann et al. by the different cooling rates of the reaction mixes: Crystals of I- $\text{Ni}_4\text{Nb}_2\text{O}_9$ were prepared by heating pellets of Nickel-oxalate (reduces to reactive NiO) and Nb_2O_5 to 1380 °C and slowly cooling them to room temperature. II- $\text{Ni}_4\text{Nb}_2\text{O}_9$ was prepared from the same reactants, but the pellets were heated to 1400 °C followed by rapid cooling. The study therefore suggested that II- $\text{Ni}_4\text{Nb}_2\text{O}_9$ is a high-temperature polymorph of I- $\text{Ni}_4\text{Nb}_2\text{O}_9$.

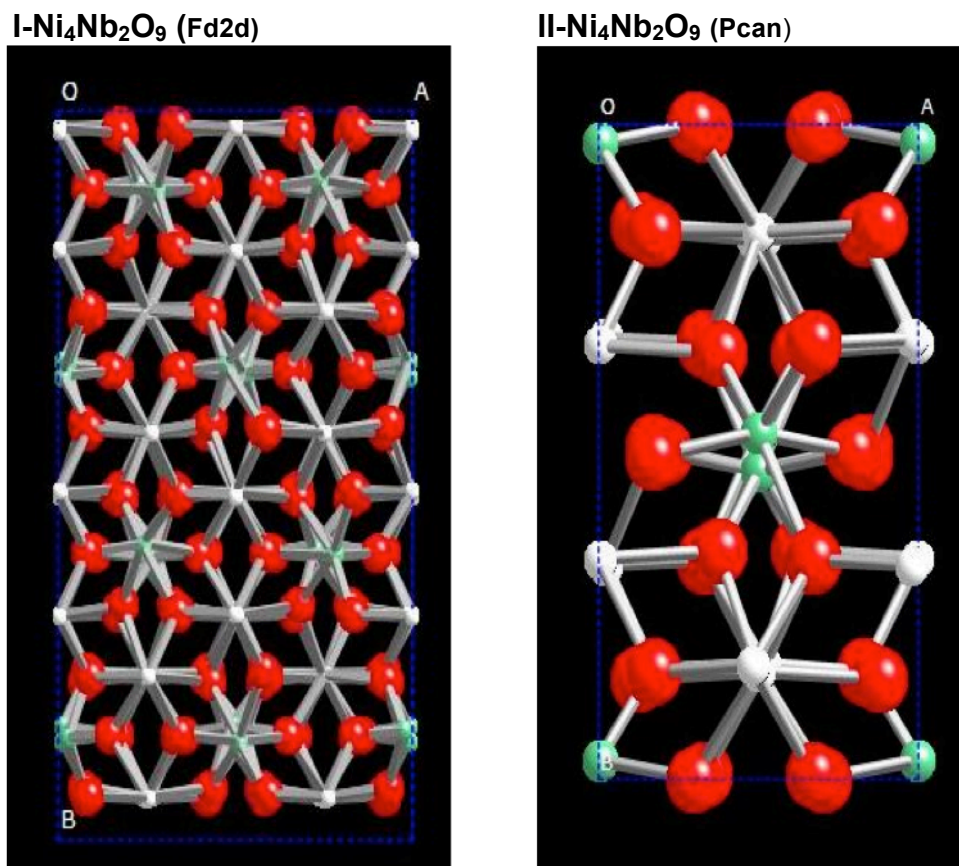


Figure 2.7: Ball-and-stick models [19] of the structures for $\text{Ni}_4\text{Nb}_2\text{O}_9$ reported by Wichmann et al.: I- $\text{Ni}_4\text{Nb}_2\text{O}_9$ (left) [17] and II- $\text{Ni}_4\text{Nb}_2\text{O}_9$ (right) [18].

2.3 Preliminary electron diffraction analysis

In the present project preliminary electron diffraction analysis were performed on the reaction-sintered pellet annealed at 1300 °C, in order to determine if the electron diffraction patterns from the Ni-Nb-O phase agreed with either suggested space groups of $\text{Ni}_4\text{Nb}_2\text{O}_9$. Selected area electron diffraction (cf. Section 5.1.1.1) was performed on a single grain of the sample, and several diffraction patterns were recorded. Figure 2.8 shows one of the diffraction patterns indexed according to both Fd2d (a) and Pcan (b). The distances R_1 , R_2 and R_3 measured in the diffraction pattern corresponds to the lattice spacings $d_1 = 4,4 \text{ \AA}$, $d_2 = 7,1 \text{ \AA}$ and $d_3 = 3,7 \text{ \AA}$, respectively (cf. Section 5.1.1.1). These values correspond to the indices 040, 004 and 044 for Fd2d, and 020, 002 and 022 for Pcan (see figures). The values are listed in Table 2.2.

Table 2.2: d -values from diffraction pattern and corresponding hkl indices for $\text{Ni}_4\text{Nb}_2\text{O}_9$ (Fd2d) and $\text{Ni}_4\text{Nb}_2\text{O}_9$ (Pcan).

d -values from diffraction pattern		hkl Fd2d	hkl Pcan
d_1	4.4 Å	040	020
d_2	7.1 Å	004	002
d_3	3.7 Å	044	022
Zone axis		[100]	[100]

The patterns correspond to the [100] zone axis (cf. section 3.3) in both cases. The simulation program WebEMAPS [20] was used to simulate diffraction patterns of the [100] planes of Fd2d and Pcan to compare with the experimental patterns. For both space groups there were extra reflections in the simulated patterns (see Figure 2.8), indicating a mismatch between the lattice of the sample and those of the reported phases of $\text{Ni}_4\text{Nb}_2\text{O}_9$.

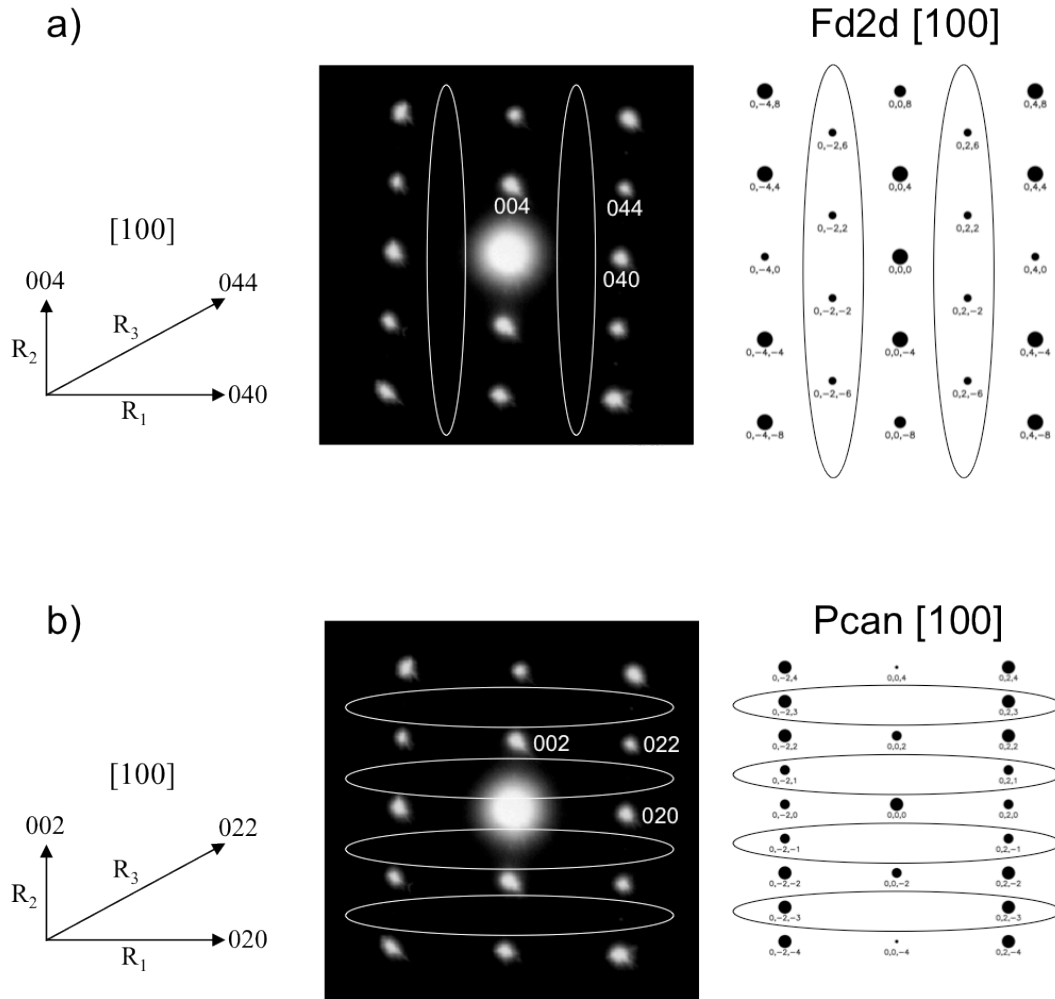


Figure 2.8: The diffraction pattern of Ni-Nb-O phase (middle) indexed according to $\text{Ni}_4\text{Nb}_2\text{O}_9$ with space group Fd2d (a) and Pcan (b). The corresponding simulated diffraction patterns along the [100] zone axis (right) reveals reflections that are absent in the experimental pattern. The figures on the left indicate in which directions R_1 , R_2 and R_3 were measured.

The focus of this project will be the investigation of the crystal structure of the Ni-Nb-O phase forming as a reaction product of LaNb_3O_9 and NiO by the means of electron diffraction and EDS. The sample used is a piece of the pellet of reaction sintered LaNb_3O_9 and NiO annealed at 1300 °C, and it will from here on be referred to as NiLN3-1300.

3 An introduction to crystallography

The theory for crystallography refers to *The International Tables for Crystallography, Vol. A* [21], unless specified otherwise.

3.1 Lattice properties of crystals

A crystal is characterized by its periodic and systematic arrangement of atoms in three dimensions, called a *crystal lattice*. The crystal structure may be described by repeating an element, called a motif, in all three dimensions. In the mathematical treatment of crystals this motif is replaced by a point, and the crystal structure is idealized as an infinite perfect three-dimensional structure called a *crystallographic pattern*, or *crystal pattern* for short. This model describes the crystal in *point space* (E^n , n = dimension), also called *direct space* or *crystal space*, and it corresponds to the real space we live in. Closely connected with the point space is the *vector space* (\mathbf{V}^n), which is used to describe crystals in terms of face normals, translation vectors etc. Metric relations are transferred from vector space onto point space, thus enabling calculation of distances and angles in point space.

3.1.1 Vector lattice

For every three-dimensional crystal pattern there exist three non-zero linearly independent translation vectors, \mathbf{t}_1 , \mathbf{t}_2 and \mathbf{t}_3 . Any linear (integral) combination of the translation vectors is a new translation vector, and the infinite set of all translation vectors of a crystal pattern is called the *vector lattice* \mathbf{L} of this crystal pattern. In principle, any three linearly independent translation vectors may be used as a basis for the vector space \mathbf{V}^3 , but in order to simplify the survey of a given lattice, certain *crystallographic bases* are chosen. A basis of the vectors \mathbf{a} , \mathbf{b} and \mathbf{c} of \mathbf{V}^3 is a crystallographic basis of the vector lattice \mathbf{L} if every integral linear combination of these vectors is a lattice vector of \mathbf{L} (see equation (3.1)).

$$\mathbf{t} = u\mathbf{a} + v\mathbf{b} + w\mathbf{c} \quad (3.1)$$

In a *primitive crystallographic basis* all lattice vectors have integral coefficients. In non-primitive crystallographic bases, the coefficients of the lattice vectors must be either integral or rational. These are conventionally used to describe “centred lattices”, see section 3.2. For every vector lattice it is possible to select a unique reduced primitive base in order to unambiguously describe that lattice. However, conventional coordinate systems with non-primitive crystallographic bases are in many cases chosen, as this simplifies the matrix description and visualization of (non-translational) symmetry operations.

3.1.2 Point lattice

A point lattice can be visualized as a set of end-points of all the lattice vectors of \mathbf{L} , or as the replacement of the repeating motif with a point. Every point in the point lattice has the same atomic environment. The point lattice belongs to point space.

3.1.3 Unit cell

The unit cell of a crystal structure contains all the information needed in order to describe the entire structure. It is defined by the structure’s *lattice parameters* or *lattice constants*, namely the base vectors \mathbf{a} , \mathbf{b} and \mathbf{c} from vector space, or the length of these vectors and the angles between them, α , β and γ (see Figure 3.1). By infinite repetition along each of the base vectors, the entire point lattice in point space is built.

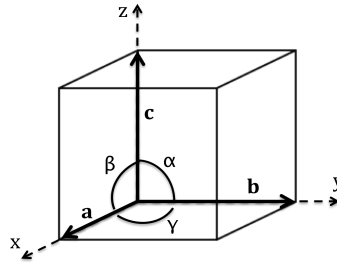


Figure 3.1: Unit cell with base vectors **a**, **b** and **c** and inter-axial angles α , β and γ indicated.

The positions of atoms in the unit cell can be described by the vector **r**:

$$\mathbf{r} = x\mathbf{a} + y\mathbf{b} + z\mathbf{c} \quad (0 \leq x, y, z < 1) \quad (3.2)$$

The unit cell is called primitive if the crystallographic basis is primitive. If the basis is non-primitive, the unit cell is called centred (cf. Section 3.2).

3.1.4 The reciprocal lattice

The reciprocal lattice is a mathematical construction in reciprocal space. This lattice is very important for the interpretation of diffraction patterns as it gives a physical picture of diffraction geometries. Each point in the reciprocal lattice represents a set of equivalent planes in the crystal. Mathematically it is defined by the reciprocal lattice vectors, **a***, **b*** and **c***. The directions of these vectors are defined by the relations

$$\mathbf{a}^* \cdot \mathbf{b} = \mathbf{b}^* \cdot \mathbf{c} = \mathbf{c}^* \cdot \mathbf{a} = \mathbf{a}^* \cdot \mathbf{c} = \mathbf{b}^* \cdot \mathbf{a} = \mathbf{c}^* \cdot \mathbf{b} = 0 \quad (3.3)$$

That is, **a*** is normal to **b** and **c**, **b*** is normal to **a** and **c** and **c*** is normal to **a** and **b**. This means that **a*** is only parallel to **a** if **a** is normal to **b** and **c** (similar for **b*** and **c***). The lengths of the vectors are given by

$$\mathbf{a}^* \cdot \mathbf{a} = \mathbf{b}^* \cdot \mathbf{b} = \mathbf{c}^* \cdot \mathbf{c} = 1 \quad (3.4)$$

As the volume of the unit cell (in real space) is given by $V = \mathbf{a} \cdot \mathbf{b} \times \mathbf{c}$ etc., the following expressions hold for the reciprocal lattice vectors:

$$\mathbf{a}^* = \frac{\mathbf{b} \times \mathbf{c}}{V} \quad \mathbf{b}^* = \frac{\mathbf{c} \times \mathbf{a}}{V} \quad \mathbf{c}^* = \frac{\mathbf{a} \times \mathbf{b}}{V} \quad (3.5)$$

The lattice spacing d is given by $d_{hkl} = 1/|\mathbf{g}_{hkl}|$, where $|\mathbf{g}_{hkl}|$ is the length of the reciprocal lattice vector. This vector is normal to the plane hkl , and is defined as

$$\mathbf{g}_{hkl} = h\mathbf{a}^* + k\mathbf{b}^* + l\mathbf{c}^* \quad (3.6)$$

h , k and l are integers and define the plane (hkl) , see section 3.3.

3.2 Classifications of space groups

3.2.1 Symmetry

The classifications of crystal patterns are based on symmetry. A *symmetry operation* of an object is defined as a motion that maps the object onto itself in point space. The motion is a *crystallographic* symmetry operation if it is a symmetry operation for a crystal pattern. These include rotation, inversion, reflection, screw motion, glide reflection and lattice translation. The first four have at least one fixed point (i.e. a point that is not affected by the operation), and the last three have no fixed points as they include translations. The *space group* of a three-dimensional crystal pattern is the set of all symmetry operations of that pattern.

The *symmetry elements* of a symmetry operation are defined as the set of its fixed points (e.g. axis, plane or single point) and a description of its motion (e.g. rotation angle, reflection or inversion). As the glide reflecting and screw operations don't have fixed points, they are described by the fixed points of the corresponding reflections and rotations, respectively, in addition to their motion. Lattice translations are not described by symmetry elements, but by Bravais lattices (see next section).

In three dimensions, the symmetry elements are: Rotation axes (1, 2, 3, 4 and 6), mirror planes (m), inversion centres ($\bar{1}$), screw axes ($2_1, 3_1, 3_2, 4_1, 4_2, 4_3, 6_1, 6_2, 6_3, 6_4$ and 6_5) and glide planes (a, b, c, n, e and d). The combination of rotation and inversion has its own name, *roto-inversion*, and symbols ($\bar{2}, \bar{3}, \bar{4}, \bar{6}$). Rotation axes, mirror planes and inversion centres are called *macroscopic symmetry elements*, while screw axes and glide planes are called *microscopic symmetry elements*. The letters and numbers in the parentheses are the *Hermann-Mauguin* (H-M) symbols for the symmetry elements. A detailed description of the symmetry elements can be found in the International Tables of Crystallography.

3.2.2 Space groups, point groups and Bravais lattices

There are infinitely many space groups that can describe crystal lattices, but based on symmetry properties they can be sorted into 230 *crystallographic space-group types* (these are normally referred to just as *space groups* as long as there is no risk of misconceptions, and apart from this section this practice is followed in the thesis). This is the most detailed classification commonly used, resulting in the highest number of classes. The space-group types may be further divided into many sub-classes, and the most commonly encountered classifications are listed in Table 3.1 and Table 3.2, along with their H-M symbols.

From the possible combinations of the macroscopic symmetry elements, 32 (crystallographic) point groups are derived. These classify the space-group types according to non-translational symmetry (symmetry elements acting at a point).

As mentioned in the previous section, a crystal may be described by an infinite number of lattice bases. Conventionally, a right-handed set of bases is chosen to simplify the description and best display the symmetry of the space group. If the smallest possible cell is chosen within these restrictions, the basis is called a *conventional (crystallographic) basis*. The metric parameters of this basis are

called *lattice* parameters. Together with a *conventional (crystallographic) origin* the conventional basis defines a *conventional (crystallographic) coordinate system* and a *conventional cell*.

Table 3.1 lists the restrictions of the coordinate systems of each crystal family. Within these restrictions, some lattice points must be described by non-integral coordinates. These are regarded as *centrings* of the conventional cell, and have simple rational coordinates. The following types of centrings are used (H-M symbols in parentheses): No centring/primitive (*P*), body centred (*I*), all-face centred (*F*), one-face centred (*A*, *B*, *C*) and hexagonal cell rhombohedrally centred (*R*). Primitive cells contain one lattice point, and centred cells contain two, three or four lattice points.

14 Bravais lattices

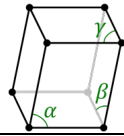
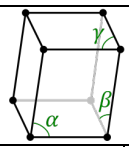
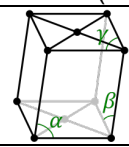
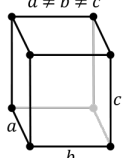
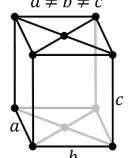
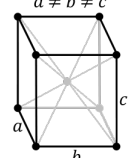
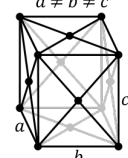
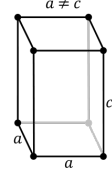
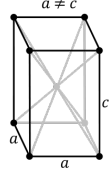
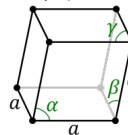
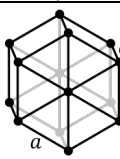
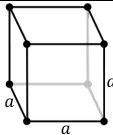
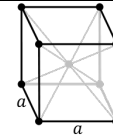
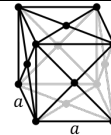
Lattices can be classified according to various criteria. The most important classification is based on the 14 *Bravais (types of) lattices*, which takes the translational periodicity of lattices into account. The Bravais lattices characterize the translational subgroup of a space group. They can be described by a combination of crystal family and lattice centring. Table 3.2 gives an overview of the crystal families, crystal systems and Bravais lattices.

Table 3.1: Crystal families, crystal systems, conventional coordinate systems and crystallographic point groups.

Crystal families	Crystal systems	Conventional coordinate systems			Crystallographic point groups
		Axial system	Restrictions on cell parameters	Parameters to be determined	
Triclinic (anorthic) (a)	<i>Triclinic</i>	<i>Triclinic (anorthic)</i>	None	a, b, c α, β, γ	$1, \bar{1}$
Monoclinic (m)	<i>Monoclinic</i>	<i>Monoclinic</i>	<i>b</i> -unique setting $\alpha = \gamma = 90^\circ$	a, b, c $\beta \ddagger$	$m, 2, 2/m$
			<i>c</i> -unique setting $\alpha = \beta = 90^\circ$	a, b, c $\gamma \ddagger$	
Orthorhombic (o)	<i>Orthorhombic</i>	<i>Orthorhombic</i>	$\alpha = \beta = \gamma = 90^\circ$	a, b, c	$222, mm2, mmm$
Tetragonal (t)	<i>Tetragonal</i>	<i>Tetragonal</i>	$a = b$ $\alpha = \beta = \gamma = 90^\circ$	a, c	$4, \bar{4}, 4/m, \bar{4}2m, 4mm, 422, 4/mmm$
Hexagonal (h)	<i>Trigonal</i>	<i>Hexagonal</i>	$a = b$ $\alpha = \beta = 90^\circ,$ $\gamma = 120^\circ$	a, c	$3, \bar{3}, 32, 3m, \bar{3}m$
		<i>Rhombohedral</i>	$a = b = c$ $\alpha = \beta = \gamma$	a, α	
	<i>Hexagonal</i>	<i>Hexagonal</i>	$a = b$ $\alpha = \beta = 90^\circ,$ $\gamma = 120^\circ$	a, c	$6, \bar{6}, 6/m, \bar{6}2m, 6mm, 622, 6/mmm$
Cubic (c)	<i>Cubic</i>	<i>Cubic</i>	$a = b = c$ $\alpha = \beta = \gamma = 90^\circ$	a	$23, m\bar{3}, 432, 43m, m\bar{3}m$

‡ These angles are conventionally taken to be non-acute, i.e. $\geq 90^\circ$.

Table 3.2: The relation between crystal families and crystal systems together with the 14 Bravais lattices. H-M symbols are given in parentheses for the Bravais lattices.

Crystal families	Crystal systems	The 14 Bravais lattices			
Triclinic (anorthic)	Triclinic primitive (<i>aP</i>)				
	 $\alpha, \beta, \gamma \neq 90^\circ$				
Monoclinic	Monoclinic primitive (<i>mP</i>)	Monoclinic single-face centred (<i>mC*</i>)			
	 $\alpha \neq 90^\circ$ $\beta, \gamma = 90^\circ$	 $\alpha \neq 90^\circ$ $\beta, \gamma = 90^\circ$			
Orthorhombic	Orthorhombic primitive (<i>oP</i>)	Orthorhombic single-face centred (<i>oC*</i>)	Orthorhombic body centred (<i>oI</i>)	Orthorhombic all-face centred (<i>oF</i>)	
	$a \neq b \neq c$	$a \neq b \neq c$	$a \neq b \neq c$	$a \neq b \neq c$	
					
	b	b	b	b	
Tetragonal	Tetragonal primitive (<i>tP</i>)		Tetragonal body centred (<i>tI</i>)		
	 $a \neq c$		 $a \neq c$		
Hexagonal	Trigonal	Hexagonal cell rhombohedrally centred (<i>hR</i>)			
		 $\alpha = \beta = \gamma \neq 90^\circ$			
	Hexagonal	Hexagonal primitive (<i>hP</i>)			
		 a			
Cubic (isometric)	Cubic primitive (<i>cP</i>)	Cubic body centred (<i>cI</i>)	Cubic all-face centred (<i>cF</i>)		
					
	a	a	a		

* C denotes a lattice point on the face normal to the c-axis. Lattice points on the faces normal to the a- and b-axes are denoted by A and B, respectively.

3.2.3 Reflection conditions

Reflection conditions, or, more precisely, *conditions limiting possible reflections*, are conditions of occurrence for reflections. There are two types of reflection conditions, *general* and *special*. The general conditions are due to centred cells, glide planes or screw axes, and are always obeyed regardless of which positions are occupied in the crystal structure. The special conditions occur in addition to the general ones, and are due to atoms located on special positions in the structure.

The conditions for centred cells apply to the whole three-dimensional set of reflections hkl , and are therefore called *integral reflection conditions* (for description of hkl Miller indices, see section 3.3). Glide planes give rise to two-dimensional sets of reflections (such as $hk0$, $h0l$, $0kl$, hhl etc.), and are called *zonal reflection conditions*. For screw axes the conditions are called *serial reflection conditions*, as they apply to one-dimensional sets of reflection (such as $h00$, $0k0$, $00l$, etc.). Note that glide planes also give rise to one-dimensional reflection conditions, as a consequence of the zonal reflection conditions. For example, an a -glide plane normal to $[010]$ gives rise to the condition $h0l$: $h = 2n$. As a consequence, the condition $h00$: $h = 2n$ is also valid, although there is no screw axis present.

The reflection conditions relevant for this study are the ones that apply to the orthorhombic and the cubic crystallographic coordinate systems (cf. section 3.2.2). These are listed in Table 3.3.

Table 3.3: Conditions limiting possible reflections in the orthorhombic and cubic crystallographic coordinate systems. Conditions that apply only to the cubic one are marked as such, the rest apply to both systems.

Effect	Type of reflections	Reflection conditions	H-M symbol	
Centred cell	hkl	None	P	
		$h + k = 2n$	C	
		$k + l = 2n$	A	
		$h + l = 2n$	B	
		$h + k + l = 2n$	I	
		$h + k, h + l$ and $k + l = 2n$ or: h, k, l all odd or all even	F	
Glide plane	$0kl$	$k = 2n$	b	
		$l = 2n$	c	
		$k + l = 2n$	n	
		$k + l = 4n$ ($k, l = 2n$)	d	
	$h0l$	$l = 2n$	c	
		$h = 2n$	a	
		$l + h = 2n$	n	
		$l + h = 4n$ ($l, h = 2n$)	d	
	$hk0$	$h = 2n$	a	
		$k = 2n$	b	
		$h + k = 2n$	n	
		$h + k = 4n$ ($h, k = 2n$)	d	
	$hhl, h\bar{h}l$	$l = 2n$	(cubic)	c, n
		$2h + l = 4n$		d
	$hkk, hk\bar{k}$	$h = 2n$	(cubic)	a, n
		$2k + h = 4n$		d
$hkh, \bar{h}kh$	$k = 2n$	(cubic)	b, n	
	$2h + k = 4n$		d	
Screw axis	$h00$	$h = 2n$	2_1	
		$h = 4n$	4_1 (cubic)	
	$0k0$	$k = 2n$	2_1	
		$k = 4n$	4_1 (cubic)	
	$00l$	$l = 2n$	2_1	
		$l = 4n$	4_1 (cubic)	

3.2.4 Space group notation

The 230 space-group types may be regarded as a combination of the 14 Bravais lattices (lattice translations), 32 point groups (macroscopic symmetry elements) and the two microscopic symmetry elements. The H-M nomenclature for the space-group types is on the form $Xefg$, where X designate the lattice centring, and efg the symbols for the symmetry elements of the group. The positions e , f and g refer to the primary, secondary and tertiary set of lattice symmetry directions, respectively. Symmetry plane normals and symmetry axes are parallel to their symmetry directions, and if they refer to the same direction they are separated by a slash, '/

Space groups may be presented with the *full international symbols*, which include both symmetry axes and symmetry planes for each direction, or the *international short symbol*, in which symmetry axes are suppressed as much as possible. Some space groups may have several settings, which are different ways of assigning the labels a , b , and c . The standard setting for a space group is the one described in the space group tables in the International Tables for Crystallography (ITC), and is indicated by the standard H-M symbol in the headline. Orthorhombic space groups have six settings, which may have different H-M symbols.

Below are explanations of the space groups encountered in section 2.2, as well as the space group for silicon as silicon is used as a standard for calibration. The space group's entry in the ITC is given in parenthesis.

Silicon is assigned the space-group type $Fd\bar{3}m$ (no. 227). This is an all-face centred cubic lattice (cF), with primary symmetry directions $\{\underline{[100]}, [010], [001]\}$, secondary symmetry directions $\{\underline{[111]}, [1\bar{1}\bar{1}], [\bar{1}\bar{1}\bar{1}], [\bar{1}\bar{1}1]\}$ and tertiary symmetry directions $\{[1\bar{1}0], \underline{[110]}, [01\bar{1}], [011], [\bar{1}01], [101]\}$ (cf. Section 3.3). The sets of directions are represented by their respective underlined direction. The full symbol is $F 4_1/d \bar{3} 2/m$, where the fourfold screw axis and the d -glide plane refer to $[100]$, the three-fold roto-inversion axis refer to $[111]$ and the two-fold rotation axis and the mirror plane refer to $[110]$. The face-centred lattice

and the d -glide plane give rise to the conditions limiting possible reflections for the space group (cf. Table 3.3).

For orthorhombic space groups, the primary, secondary and tertiary symmetry directions are $[100]$, $[010]$ and $[001]$, respectively. Neither of the reported space groups for $\text{Ni}_4\text{Nb}_2\text{O}_9$ is described with its standard setting.

$Ccma$ ¹ (no. 64): Full symbol: $C 2/c 2/m 2_1/a$. C -centred orthorhombic Bravais lattice (oC) with a c -glide plane normal to $[100]$, a mirror plane normal to $[010]$ and an a -glide plane normal to $[001]$. The C -centring of the lattice and the c - and a -glide planes give rise to the conditions limiting possible reflections for the space group (cf. Table 3.3).

$Cc2a$ ¹ (no. 41): Full symbol: $Cc2a$. C -centred orthorhombic Bravais lattice (oC) with a c -glide plane normal to $[100]$, a two-fold rotation axis along $[010]$ and an a -glide plane normal to $[001]$. The conditions limiting possible reflections are the same as for $Ccma$.

$Fd2d$ (no. 43): Full symbol: $Fd2d$. All-face centred orthorhombic Bravais lattice (oF) with two d -glide planes, one normal to $[100]$ and the other normal to $[001]$, and a two-fold rotation axis along $[010]$. The F -centring of the lattice and the d -glide planes give rise to the conditions limiting possible reflections for the space group (cf. Table 3.3).

$Pcan$ (no. 60): Full symbol: $P 2/c 2_1/a 2_1/n$. Primitive orthorhombic Bravais lattice (oP) with a c -glide plane normal to $[100]$, an a -glide plane normal to and a two-fold screw axis parallel to $[010]$ and an n -glide plane normal to and a two-fold screw axis parallel to $[001]$. The c -, a - and n -glide planes and the two-fold screw axes give rise to the conditions limiting possible reflections for the space group (cf. Table 3.3).

¹ The space-group symbols were updated in 1992 when the e glide plane was introduced: No. 41 from $Cc2a$ to $Cc2e$, and no. 64 from $Ccma$ to $Ccme$.

3.3 Lattice planes and directions

In order to describe planes and directions in a crystal structure, *Miller indices* are commonly used. The Miller indices of a plane (hkl) intersect the a , b and c axes of the Bravais lattice at $1/h$, $1/k$ and $1/l$, respectively. If the plane is parallel to an axis, the corresponding Miller index is zero. The indices are usually scaled to the smallest possible integers. Figure 3.2 show some planes with their respective miller indices.

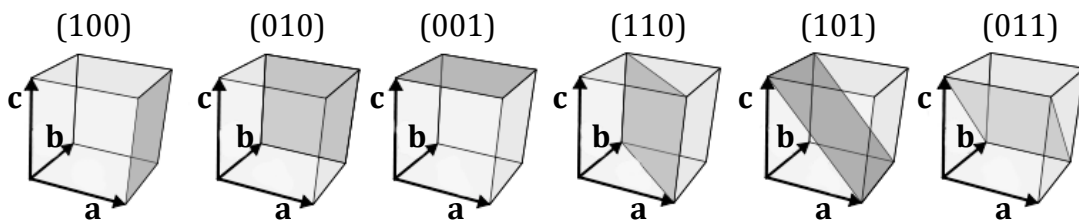


Figure 3.2: Planes with their respective Miller indices.

Due to the translational properties of the lattice, all parallel planes have the same Miller indices. Curly brackets, $\{hkl\}$, designate equivalent planes (e.g. (100) , (010) and (001) in a cubic crystal). Negative indices are usually displayed with a bar above the number, e.g. $(0\bar{1}0)$, $(\bar{2}01)$, etc. Directions in a crystal are described by the Miller indices $[uvw]$ of the translation vector, \mathbf{t} , of the vector lattice (see equation (3.1)). This is called a *zone axis*, and it is parallel with the faces (and thereby orthogonal to the plane-normals) of the planes that are contained in that zone. It may be calculated from the vector cross product of any two planes $h_1k_1l_1$ and $h_2k_2l_2$ in the zone:

$$[uvw] = [h_1k_1l_1] \times [h_2k_2l_2] \quad (3.7)$$

In reciprocal space, (hkl) designates a particular vector normal to the (hkl) plane in real space. $\{hkl\}$ is then equivalent directions in reciprocal space.

$[UVW]$ is a particular plane, and $\langle UVW \rangle$ is the set of equivalent planes. The convention for indexing spots in a diffraction pattern is to leave out the brackets, and just write hkl . In a selected area diffraction pattern, the zone axis is normal to the reciprocal lattice vectors of all the reflections in the pattern (cf. Section 4.2). It can thus be calculated from the vector cross product of any two in-plane reciprocal lattice vectors \mathbf{g} and \mathbf{h} :

$$[uvw] = \mathbf{g} \times \mathbf{h} = [h_1 \mathbf{a}^* k_1 \mathbf{b}^* l_1 \mathbf{c}^*] \times [h_2 \mathbf{a}^* k_2 \mathbf{b}^* l_2 \mathbf{c}^*] \quad (3.8)$$

Table 3.4 lists the Miller notation for planes and directions in real space and reciprocal space.

Table 3.4: Miller notation for planes and directions in real space and reciprocal space

Real Space	Reciprocal space	Notation
Particular direction (zone axis)	Particular plane	$[UVW]$
Equivalent directions	Equivalent planes	$\langle UVW \rangle$
Particular plane	Particular direction	(hkl)
Equivalent planes	Equivalent directions	$\{hkl\}$
Diffracting plane	Indexed reflection	hkl

The angle φ between two planes $h_1 k_1 l_1$ and $h_2 k_2 l_2$ in an orthogonal crystal may be calculated using the following equation [22]:

$$\cos \varphi = \frac{h_1 h_2 a^{*2} + k_1 k_2 b^{*2} + l_1 l_2 c^{*2}}{\sqrt{h_1^2 a^{*2} + k_1^2 b^{*2} + l_1^2 c^{*2}} \sqrt{h_2^2 a^{*2} + k_2^2 b^{*2} + l_2^2 c^{*2}}} \quad (3.9)$$

a^* , b^* and c^* are the reciprocal lattice constants. By exchanging hkl with UVW , and the reciprocal lattice constants with the real space ones (a , b and c), the equation can be used to calculate the angle between zone axes.

4 Diffraction by X-rays and electrons

When propagating waves hit an obstacle with multiple equally spaced slits (a grating), the waves are diffracted. The effect is most pronounced if the wavelength of the waves is in the same order as or smaller than the size of the spacings in the grating. The phenomenon is illustrated by light being diffracted by two slits in Figure 4.1. Monochromatic planar waves are diffracted by the double slits, the diffracted waves interfere with each other and concentrated beams appear in certain directions where the interference is constructive. Between the beams the interference is destructive, and there is little to no intensity.

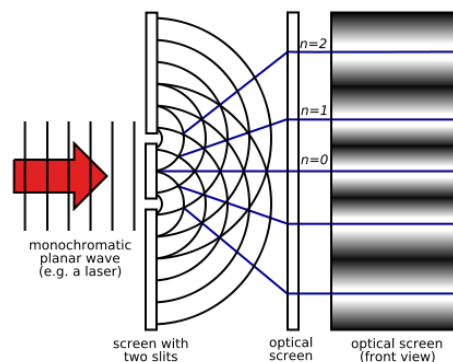


Figure 4.1: Schematic drawing of two-slit diffraction with visible light [23].

The atomic lattice in a solid may be regarded as a grating, and since both electrons and X-rays have wavelengths much shorter than the atomic distances, they can be diffracted by the lattice. However, the mechanisms of the interactions of electrons and X-rays with matter are different, leading to a few differences in the diffraction mechanisms as well.

Electrons interact strongly with matter by electrostatic interactions due to their low mass and negative charge, and are easily deflected by both the atomic nucleus and other electrons in a material. The scattering is either elastic or

inelastic, and it is the elastic scattering that is the main source of contrast in images, as well as much of the intensity in DPs. In an elastic scattering event the electron changes direction but maintains its energy, whereas an inelastic event causes energy loss as well as change in direction. The latter is the source of spectroscopic signals such as characteristic X-rays in the electron microscope, which may be used to analyse the elemental composition of the sample (see section 5.2) [24].

X-rays are not scattered directly as electrons are, and the interactions of X-rays with the material is much weaker than for electrons. In X-ray diffraction, the electrons in the material respond to the electromagnetic field of the incoming X-rays. The electrons oscillate with the period of the X-ray beam, and emit their own electromagnetic field with the same wavelength and phase as the incident X-rays. This field propagates radially from each scattering source, and is called the scattered wave [24].

Although XRD is more accurate than TEM ($\sim 0.001 \text{ \AA}$ vs. $\sim 0.01 \text{ \AA}$) when it comes to determining lattice spacing in crystals, the diffraction results in XRD are averaged over the whole sample. This often results in overlapping peaks in the diffraction pattern when the sample contains several phases. With selected area electron diffraction (SAD, SAED) the area of analysis is typically $\sim 1 \text{ \mu m}$, and with the Convergent beam electron diffraction (CBED) technique it is even possible to analyse areas in the nanometre range [24]. Thus information from individual grains and phases can be obtained in the TEM.

4.1 The Laue equations and Bragg's law

The Laue equations were derived by the German scientist von Laue, who argued that diffracted waves are in phase if the path difference between waves scattered by adjacent scattering centres is a whole number of wavelengths, $n\lambda$ [24]. Figure 4.2 shows a schematic drawing of a plane wave, with wavelength λ , scattered by two atoms (B and C) a distance a apart. The wave is incident at

an angle θ_1 and scattered at an angle θ_2 , and the path difference between the waves, $AB - CD$, can be written

$$a(\cos\theta_1 - \cos\theta_2) = h\lambda \quad (4.1)$$

This is the first Laue equation.

In three dimensions there are two more directions with distances b and c and appropriate angles θ_n , and the Laue equations for these can be written

$$b(\cos\theta_3 - \cos\theta_4) = k\lambda \quad (4.2)$$

$$c(\cos\theta_5 - \cos\theta_6) = l\lambda \quad (4.3)$$

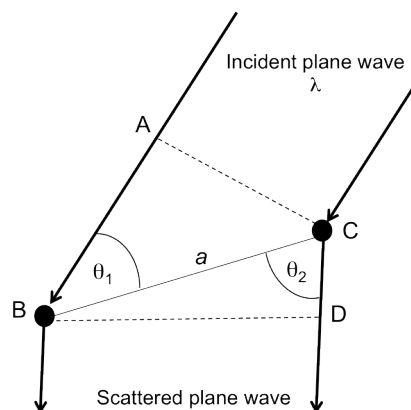


Figure 4.2: Schematic drawing of a plane wave, with wave length λ , scattered by two atoms (B and C) a distance a apart. The wave is incident at an angle θ_1 and scattered at an angle θ_2 , and the path difference between the waves is $AB - CD$.

Another way of describing diffraction is by Bragg's law:

$$2d \sin(\theta_B) = n\lambda \quad (4.4)$$

Where

d is the lattice plane distance

θ_B is the Bragg angle

n is an integer and

λ is the wavelength of the incident electrons

The Bragg equation states that in order for the waves to remain in phase after being reflected off adjacent scattering centres, the path difference, $2d\sin\theta_B$ of the waves must be an integral number of their wavelength (see Figure 4.3). The *Bragg angle*, θ_B , is thus the angle at which one expects maximum diffracted intensity from specific crystal planes.

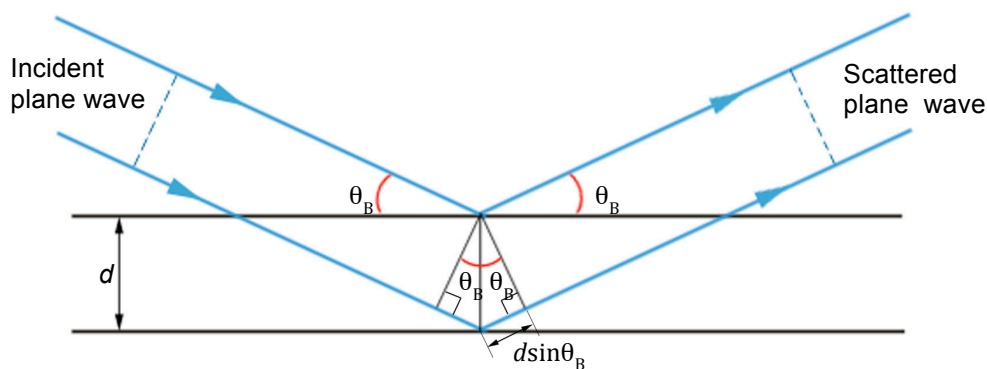


Figure 4.3: Schematic illustration of the Bragg diffraction of a plane wave with wavelength λ , incident at an angle θ_B to atomic planes of spacing d .

Unlike the Laue equations, the Bragg approach is not really a valid treatment of the phenomenon of electron scattering. However, it can be derived as a special form of the Laue equations, and as it gives a very useful mathematical and geometrical description of diffraction. The terms Bragg reflection and Bragg angle are commonly used to describe diffraction in the TEM [24].

4.2 The Ewald sphere

The Ewald sphere is a geometric construction that demonstrates the relationship between the wavelengths of the incident and diffracted beams, the diffraction angle for a given reflection and the reciprocal lattice of the crystal (see Figure 4.4). It is constructed by drawing a vector \mathbf{k}_o with length $1/\lambda$ from the origin O of the reciprocal lattice. About the vector's endpoint a sphere of radius $1/\lambda$ is constructed. The reciprocal lattice points that intersect the face of the sphere are the ones that satisfy the Bragg condition, and thus contribute to the diffraction pattern. The scattered wave is represented by the wave vector \mathbf{k} , at an angle 2θ to \mathbf{k}_o , and also with a length $1/\lambda$. When the Bragg condition is satisfied for a reflection, the difference between the incident and scattered wave is

$$(\mathbf{k} - \mathbf{k}_o) = \mathbf{g} \quad (4.5)$$

Remember from section 3.1.4 that \mathbf{g} is the reciprocal lattice vector with a direction normal to the reflecting plane and with a length $|\mathbf{g}| = 1/d$. Equation (4.5) is another formulation of Bragg's law [24]. The planes of points normal to the incident beam are termed Laue zones. The plane intersecting the origin of the reciprocal lattice is called the zero order Laue zone (ZOLZ). The next two planes (closer to the centre of the sphere) are the first and second order Laue zones (FOLZ and SOLZ), and the rest of the above planes are just called higher order Laue zones (HOLZ) (see Figure 4.4) [24].

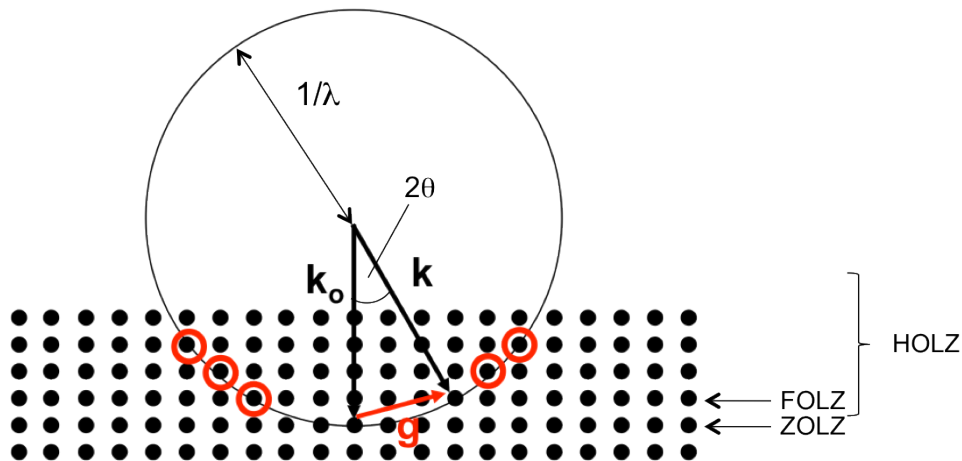


Figure 4.4: The Ewald sphere intersecting an array of reciprocal lattice points. The incident and diffracted wave are represented by the wave vectors k_0 and k , respectively. The difference between these two vectors is g , the reciprocal lattice-vector, when Bragg's law is satisfied. The lattice points of higher order Laue zones intersected by the face of the sphere are circled. The angle of 2θ is greatly exaggerated for the sake of illustration.

Because of the short wavelengths of electrons (~ 3.7 pm for 100-keV electrons), the Ewald sphere is very large compared to the lattice distances. It may therefore be approximated as flat in the area of interest, and it cuts through many lattice points near the origin of the lattice. With very thin specimens (such as in TEM), the intensity distribution around each reciprocal lattice point is spread out in the form of spikes directed normal to the specimen. The result is that many reciprocal lattice points contribute to the diffraction pattern even though they are not at exactly Bragg position (see Figure 4.5). This may also be the case with X-ray diffraction, depending on the size and shape of the sample. However, since the wavelengths of X-rays are in the order of 0.2 nm, the Ewald sphere is quite small relative to the lattice distances and with a large curvature. It can therefore only intersect a small number of lattice points, and it is necessary to rotate the sample or use other means to produce sufficient reflections [24].

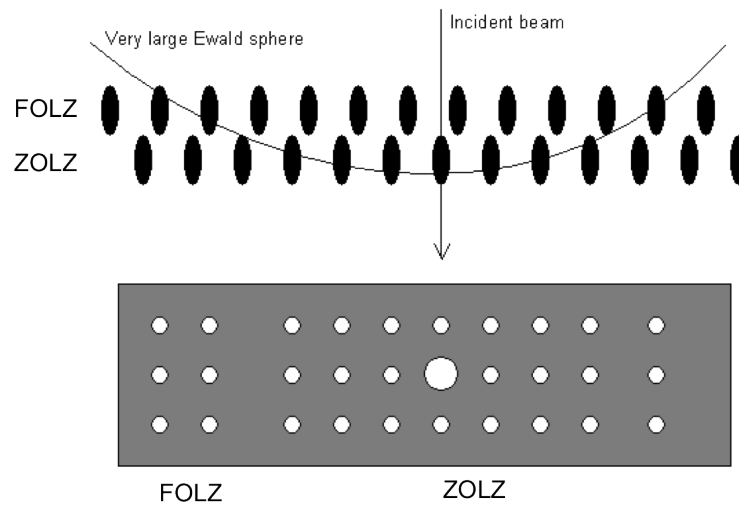


Figure 4.5: A part of the Ewald sphere intersecting elongated reciprocal lattice points, and the resulting diffraction pattern beneath. The elongation of the points and the size of the sphere make intersection of many points and also points from higher order Laue zones possible.

4.3 Kinematic and dynamic intensities

Kinematical scattering is when the incident wave is only scattered once – the diffracted intensities are then truly reflecting the crystal structure. However, when a beam is strongly scattered at the Bragg angle at one scattering centre, it is in the perfect Bragg orientation relative to adjacent scattering centres. The beam may then be diffracted back into the direct beam, or even be scattered multiple times. This is called dynamical scattering, and may occur for electrons because of their strong interaction with matter. The probability of dynamical scattering for electrons increases with the sample thickness, as this also increases the interaction cross section of the electrons. The consequence is that dynamical scattering makes it difficult to obtain correct kinematical intensities directly from a DP. With X-rays, on the other hand, one can assume purely kinematical intensities because of their weaker interaction with the atoms [24]. One way of obtaining close to kinematical intensities in the TEM is by the precession technique, where the incident beam precesses at a certain angle about

a centred zone-axis direction. The diffracted intensities are then integrated through the Bragg condition, and with a large enough angle the dynamical effects are reduced because very few reflections are excited off the zone-axis condition at the same time [24].

4.3.1 Umweganregung

As explained in sections 3.2.1 and 3.2.2, certain symmetry elements and lattice centring give rise to absent reflections compared to a primitive lattice. These are often termed kinematically forbidden reflections, as the conditions apply to the kinematic intensities. However, because of dynamical scattering, some kinematically forbidden reflections still appear in electron diffraction patterns. This may happen when the conditions of *Umweganregung* (multiple diffraction) are satisfied, that is when $\mathbf{g} = \mathbf{g}_1 + \mathbf{g}_2$ and the Bragg condition is satisfied for \mathbf{g}_2 and \mathbf{g}_1 . Here \mathbf{g} is the reciprocal lattice vector for the kinematically forbidden reflection, and \mathbf{g}_1 and \mathbf{g}_2 are the reciprocal lattice vectors for allowed reflections [25]. Kinematically forbidden reflections may typically be identified by their appearance and disappearance when tilting about the row in which they lie. Dynamical scattering is demonstrated both in the tilt series of silicon (cf. Figure 5.7) and in tilt series B and C (cf. Sections 6.2.2 and 6.2.3, respectively).

5 Experimental techniques and procedure

In the following sections some of the most important features and basic principles of Transmission Electron Microscopy (TEM) and Scanning Electron Microscopy (SEM) relevant for this thesis will be outlined, and the specific instruments used and procedures followed in this project will be described.

5.1 Transmission Electron Microscopy (TEM)

The principle of an electron microscope is much the same as for an optical microscope, which uses visible light to image a sample and a set of glass lenses to focus the beam and magnify the image. In the electron microscope, however, the specimen is illuminated with electrons, and the lenses that focus the beam and magnify the image are electromagnetic. In the transmission electron microscope (TEM), the electrons pass through the thin (~100 nm) specimen, and because of the small wavelength (~0.001 nm) and high energy (100-400 keV) of the electrons a wide range of signals are generated. The mainly utilized signals are transmitted electrons for imaging and diffraction, and characteristic X-rays.

The electrons, depending on the type of instrument, are emitted from a filament (tungsten hairpin or LaB₆ crystal) or a field emission gun (FEG) and are accelerated in an anode by a high negative electrical potential (80-1000 kV). In conventional TEMs the electron source is located at the top of the microscope. The electromagnetic lenses above the specimen stage (condenser lenses) focus the beam onto the specimen, and the lenses below (objective lens and projector lenses) focus and magnify the image/diffraction pattern that can be viewed on a phosphorescent screen or recorded on film at the bottom of the column. Apertures are used to limit the amount of electrons passing through it. An aperture can have different uses (depending on its position), such as maintaining the coherence of the electron beam (condenser aperture, below the

condenser lens), controlling image contrast (objective aperture, below the objective lens) and limiting the area from which signals are recorded (selected area aperture, below the objective aperture). Figure 5.1 shows a diagram of the TEM with some of the most important components labelled.

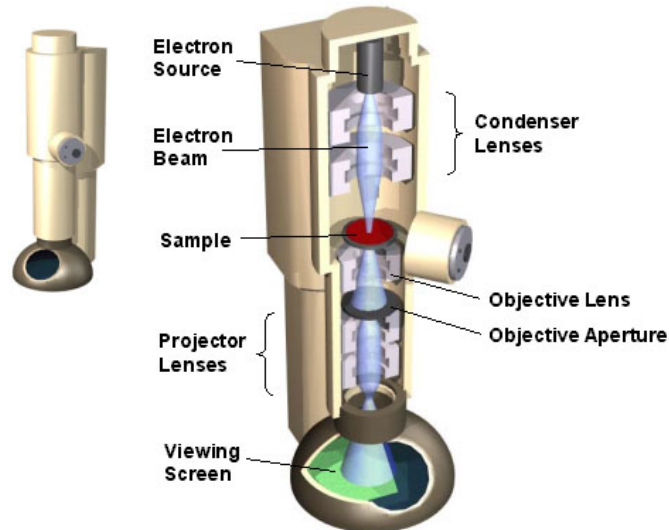


Figure 5.1: Diagram of the Transmission Electron Microscope [26].

The simplified ray diagram in Figure 5.2 illustrates the beam paths after scattering in the specimen. Beams scattered at different angles but from the same point in the sample, meet at the same point in the image plane and thus contribute to the image of the specimen. Beams scattered at the same angles but from different points in the specimen meet at the same point in the back focal (diffraction) plane, forming the diffraction pattern (DP).

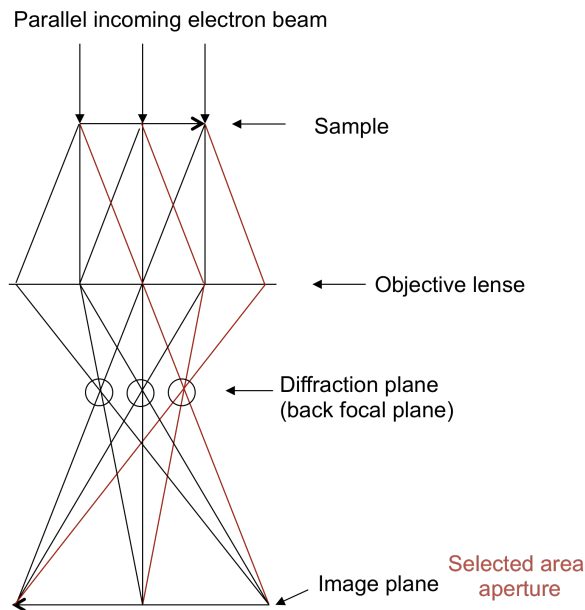


Figure 5.2: Simplified ray diagram in a Transmission Electron Microscope.

5.1.1 Diffraction techniques

Depending on the settings of the microscope, different diffraction techniques are possible in the TEM. The two most common techniques are the selected area electron diffraction (SAD, SAED) and convergent beam electron diffraction (CBED). Although the technique of CBED was not used in this study, a short description is appropriate. CBED is performed with a convergent beam, and the resulting pattern consists of disks. The illuminated area of the sample is determined by the probe size, which is in the order of a few nanometres (~1-100 nm). The spatial resolution of this technique far exceeds that of SAD (see below), and it is in principle possible to use it to examine nano-sized particles [24]. The beam interacts with several Laue zones (cf. Section 4.2), and the diffraction patterns therefore contain three-dimensional crystallographic information about the specimen. This makes it possible to determine properties such as the point group, space group and lattice parameters of the crystal (cf. Section 3.2).

SAD is the technique utilized in this study, and will be described in more detail below.

5.1.1.1 Selected area electron diffraction

SAD is performed by illuminating the sample with a parallel beam, as shown in Figure 5.2. The area of analysis is limited by the *selected area aperture*, and is typically $\sim 1 - 10 \mu\text{m}$ in diameter [24]. The resulting image on the viewing screen in the microscope is a *selected area diffraction pattern* (SADP). If the area of analysis covers only a single-crystal region, the pattern will consist of sharp spots as in Figure 5.3.

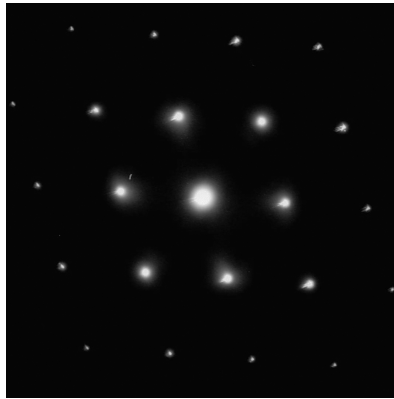


Figure 5.3: Example of selected area diffraction spot pattern from the Si [110] zone axis.

The lattice spacing, d , may be calculated from the measured distance between two spots in a diffraction pattern. As can be seen in Figure 5.4, the measured distance R between two spots is given by

$$\frac{R}{L} = \tan 2\theta_B \sim \theta_B \quad (5.1)$$

The approximation $\tan 2\theta_B \sim \theta_B$ can be made assuming very small scattering angles. L is the effective distance between the specimen and the observed diffraction pattern, and is called the *camera length*. From the Bragg equation (4.4), and using the same approximation as above, we know that $\lambda/d = 2 \sin \theta_B \sim 2\theta_B$. Combining this with equation (5.1), we get

$$Rd = \lambda L \leftrightarrow d = \frac{\lambda L}{R} \quad (5.2)$$

Due to limitations in the microscope and the measuring of distances, the accuracy of calculated d -values are estimated to be $\sim 0.01 \text{ \AA}$.

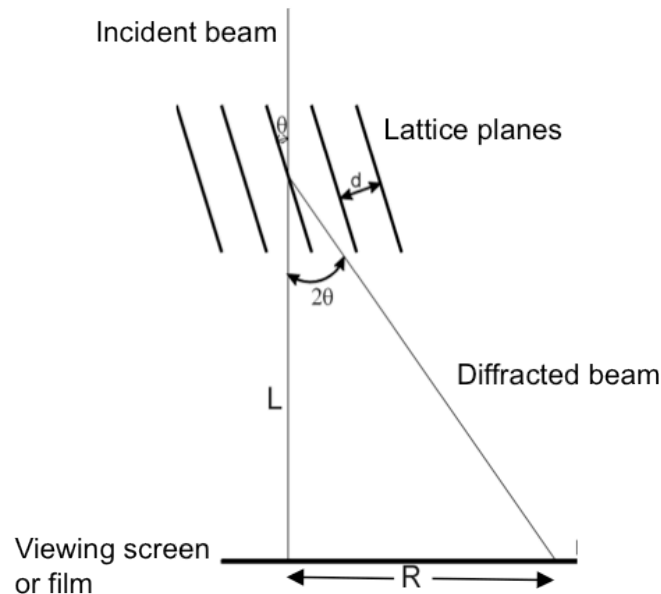


Figure 5.4: Illustration of the geometric relation between the camera length L , the measured distance R and the Bragg angle θ_B .

5.1.2 SAD tilt series

A tilt series consists of several SADPs from zone axes (cf. Section 3.3) with one common row of reflections, all taken from the same grain. By combining these patterns, it is possible to reconstruct the reciprocal lattice and thus the Bravais lattice of the structure. By tilting about a common row it is also possible to detect kinematically forbidden reflections along that row, as they may be visible in some patterns and not in others. Extinction conditions for the crystal pattern may thus be identified, and by combining these with the Bravais lattice it may be possible to limit the possible space groups of the structure. Sometimes it is difficult to reach the exact zone axes by tilting the specimen stage (e.g. at the end of the tilt range of the stage), and the exact position may be

reached by tilting the beam instead of the stage to reach exact Bragg position [24].

All diffraction patterns were obtained with the specimen at eucentric height. This ensures that the image does not move laterally when the specimen is tilted about the holder axis (X-axis, see next section), and is achieved by adjusting the physical height of the specimen to focus the image, while keeping the objective-lens current at a fixed value. This also ensures that all images/diffraction patterns are obtained at the same objective-lens magnification [24].

5.1.2.1 Calculating tilt angles

In this study a side-entry double tilt specimen holder was utilized, facilitating specimen tilting about the X- and Y-axes. For this holder the X-axis is parallel to the specimen holder, while the Y-axis is perpendicular to the holder.

For $X, Y = 0$, both axis are perpendicular to the incident electron beam and lie in the plane of the specimen. When tilting about the X-axis, the Y-axis remains in the plane of the specimen and moves with respect to the beam. When tilting about the Y-axis, the X-axis remains perpendicular to the beam, and thus moves with respect to the plane of the specimen. The schematic diagram in Figure 5.5 illustrates this by defining one axial system for the microscope (X_m, Y_m, Z_m) and one for the specimen (X_s, Y_s, Z_s), where $X_m = X$ and $Y_s = Y$. The tilt angles α_1 and β_1 denote the tilt about the axes X_m (X) and Y_s (Y), respectively.

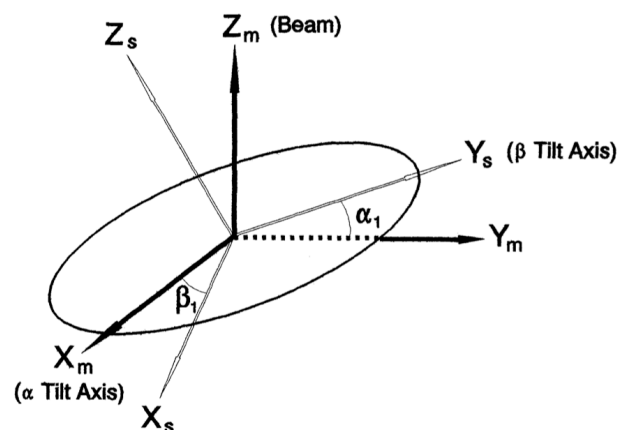


Figure 5.5: Schematic diagram showing the relative positions of the axes in the two axial systems [27]. The circle indicates the specimen plane.

When the specimen is tilted from the position defined by α_1 and β_1 to another position defined by α_2 and β_2 , the overall tilt angle, θ_{12} , may be estimated using the following equation [27]:

$$\cos\theta_{12} = \cos(\beta_2 - \beta_1) \cos\alpha_1 \cos\alpha_2 + \sin\alpha_1 \sin\alpha_2 \quad (5.3)$$

The accuracy of TEM tilt stages is reputed to be $\pm 0.5^\circ$, possibly due to mechanical backlash of the stage. The accuracy can be improved by always moving both tilts in the same direction (either both plus or both minus) [27].

5.1.3 Sample preparation

There are several different methods to achieve the required ~ 100 nm specimen thickness, depending on the material properties of the sample. In the present study two methods were chosen for sample preparation, crushing and ion milling.

Crushing is a fast and easy method requiring very little material, but the analysable areas are quite small. Grains may also overlap or shadow each other, which may be of particular concern when performing EDS analysis (see section 5.2) on multi-phase samples. Ion milling is time consuming and requires more material than crushing, and the heat from the Ar^+ ion beam may damage the specimen (e.g. structural changes, amorphization). However, it produces samples with large analysable areas, and the risk of grains shadowing each other is very small. Lowering the ion beam angles and acceleration voltage will also minimize the amount of amorphization.

The crushing method was chosen for silicon, as this is a known, single-phase structure and there was no need to perform EDS analysis on the sample. The ion milling method was chosen for the NiLN3-1300 sample, as this consists of several phases and it was desirable with large analysable areas. As the sample had been heat treated at high temperatures (>1300 °C), the risk of structural

changes due to argon ion beam heating was considered low, as typical temperatures are about 100 °C. Low angles and acceleration voltage was chosen to minimize the risk of amorphization.

5.1.3.1 Crushing

A small piece of a high-purity wafer of multicrystalline silicone was crushed with ethanol, and a droplet of the suspension was deposited on a holey carbon film supported by a copper grid. As the ethanol vaporized, the fine particles were left on the carbon film.

5.1.3.2 Ion milling

A small piece (about 4x4 mm) of the Ni-Nb-O sample was mounted on a glass rod with crystal bond and mechanically ground by SiC paper to a smooth surface. A copper support ring with a diameter of 3 mm was then glued to that surface for support, and the specimen was again mounted on the glass rod, copper ring facing the rod. After being ground to transparency, the specimen was ion milled in a *Gatan Model 691 precision ion polishing system* with Ar⁺ ion beams at 5.0 keV (6° top angle, 3° bottom angle).

5.1.4 Instrumentation

Two transmission electron microscopes were used in this project: A JEOL 2010F FEG electron microscope, from now on called the 2010F microscope. This microscope is equipped with a Noran Vista EDS system. The instrument was operated at an acceleration voltage of 200kV ($\lambda = 0.00251$ nm). The thin window detector enables detection of light elements (including oxygen). The second microscope is a JEM 2000FX (LaB6) electron microscope, from now on called the 2000FX microscope. This instrument is equipped with a NORAN system six (NSS) EDS system. It was operated at an acceleration voltage of 200 kV ($\lambda = 0.00251$ nm). The camera length of the microscope was calibrated with a silicon standard in order to achieve more accurate d-values from selected area diffraction patterns (cf. Section 5.1.5.1).

5.1.5 Silicon as a standard

As silicon is a well-known structure, it was used to calibrate the camera length in the 2000FX microscope. In addition, the silicon sample was used to check the reliability of the procedure of constructing the Bravais lattice of a crystal from a tilt series of SADPs (also with the 2000FX microscope).

Silicon crystallizes with the cubic space group $Fd\bar{3}m$, with lattice parameter $a = 5.430(54) \text{ \AA}$ [28].

5.1.5.1 Calibration

Diffraction patterns of the Si $[100]$ and $[110]$ zone axes were obtained at 66 cm nominal camera length and at eucentric height (cf. Section 5.1.2). Due to asymmetry in the objective lens, the diffraction patterns in the TEM may be stretched. The calibration was therefore performed for several directions (see Figure 5.6).

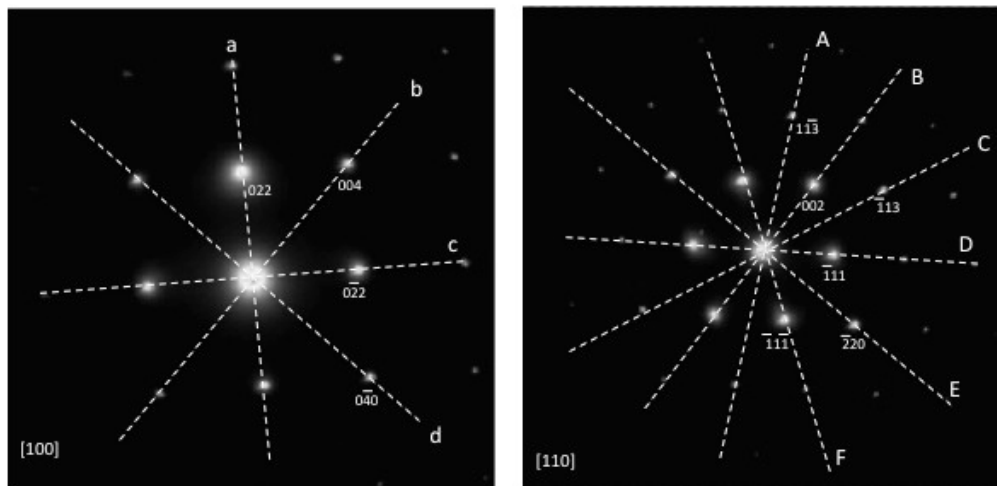


Figure 5.6: Diffraction patterns of the $[100]$ and $[110]$ planes of silicon.

The distances between the central spot and the first spot along each of the directions were measured, and the corresponding camera lengths were calculated according to (5.2). The d -values used for the calculations and the resulting camera lengths are listed in Table 5.1. The calibrated camera lengths

show quite large deviations from the nominal camera length of 66.0 cm. They also vary from 58.6 cm to 60.4 cm depending on the direction measured in the diffraction pattern, confirming that the diffraction pattern is astigmatic. By calibrating the camera length, the calculated d -values are corrected with 0.13 – 0.22 Å, depending on the direction measured on the pattern.

Table 5.1: Calibrated camera lengths.

Direction	Measured distances [cm]	hkl	Literature d -value for silicon [Å]	Calibrated camera length [cm]
a	0.777	022	1.920	59.4
b	1.083	004	1.358	58.6
c	0.776	022	1.920	59.4
d	1.117	040	1.358	60.4
A	0.905	113	1.637	59.0
B	0.543	002	2.716	58.8
C	0.900	113	1.637	58.7
D	0.477	111	3.135	59.6
E	0.788	220	1.920	60.3
F	0.478	111	3.135	59.7

5.1.5.2 Tilt series

The Si [100] zone axis was located and the tilt series in Figure 5.9 was recorded. The experimental overall tilt angle between each two planes was calculated using equation (5.3). Inserting for the zone axes and the lattice parameter, a , equation (3.9) was used to calculate the theoretical angle between the planes. Table 5.2 lists the calculated and the experimental tilt angles between the planes in the tilt series. The effect of the mechanical backlash was experienced for these recordings, although the accuracy of $\pm 0.5^\circ$ applied to the case where both tilts were moved in the same direction (from [100] to [110], and [110] to [332]). When the specimen was tilted in the $-x$ and $+y$ directions (from [100] to [111] along the diagonal), the deviation from the calculated angles ranged from $\pm 0.3^\circ$ to $\pm 2.2^\circ$. When tilting from [332] to [111] the tilts were moved in the $+x$ and $-y$ directions, with a deviation of 0.4° . In some cases it was necessary to tilt a bit back and forth to reach the exact zone axis, and this may be a reason for the larger deviations.

Table 5.2: Calculated and experimental angles between the diffraction planes of the silicon tilt series.

<i>Diffraction planes</i>	<i>Experimental angle</i>	<i>Calculated angle</i>
[100] and [310]	18.8°	18.4°
[310] and [210]	7.9°	8.1°
[210] and [110]	18.7°	18.4°
[110] and [332]	25.3°	25.2°
[332] and [111]	10.4°	10.0°
[111] and [433]	5.4°	8.1°
[433] and [211]	12.4°	11.4°
[211] and [311]	11.2°	10.0°
[311] and [411]	6.1°	5.8°
[411] and [611]	7.0°	6.2°
[611] and [100]	11.1°	13.3°

Another effect observed in the tilt series is an in-plane rotation of the diffraction patterns relative to each other. The tilt series was recorded from [100] via [110] to [111], and then back to [100] along the diagonal in Figure 5.9. The two diffraction patterns of [100] were not rotated relative to each other. The rotation is most pronounced in the patterns from [100] to [110], shown in Figure 5.7, where the first and last patterns are rotated 17° relative to each other. Figure 5.8 shows the lines indicating the common row of the patterns superimposed on each other. The in-plane rotation did not have any measurable effect on the calibration of the camera length.

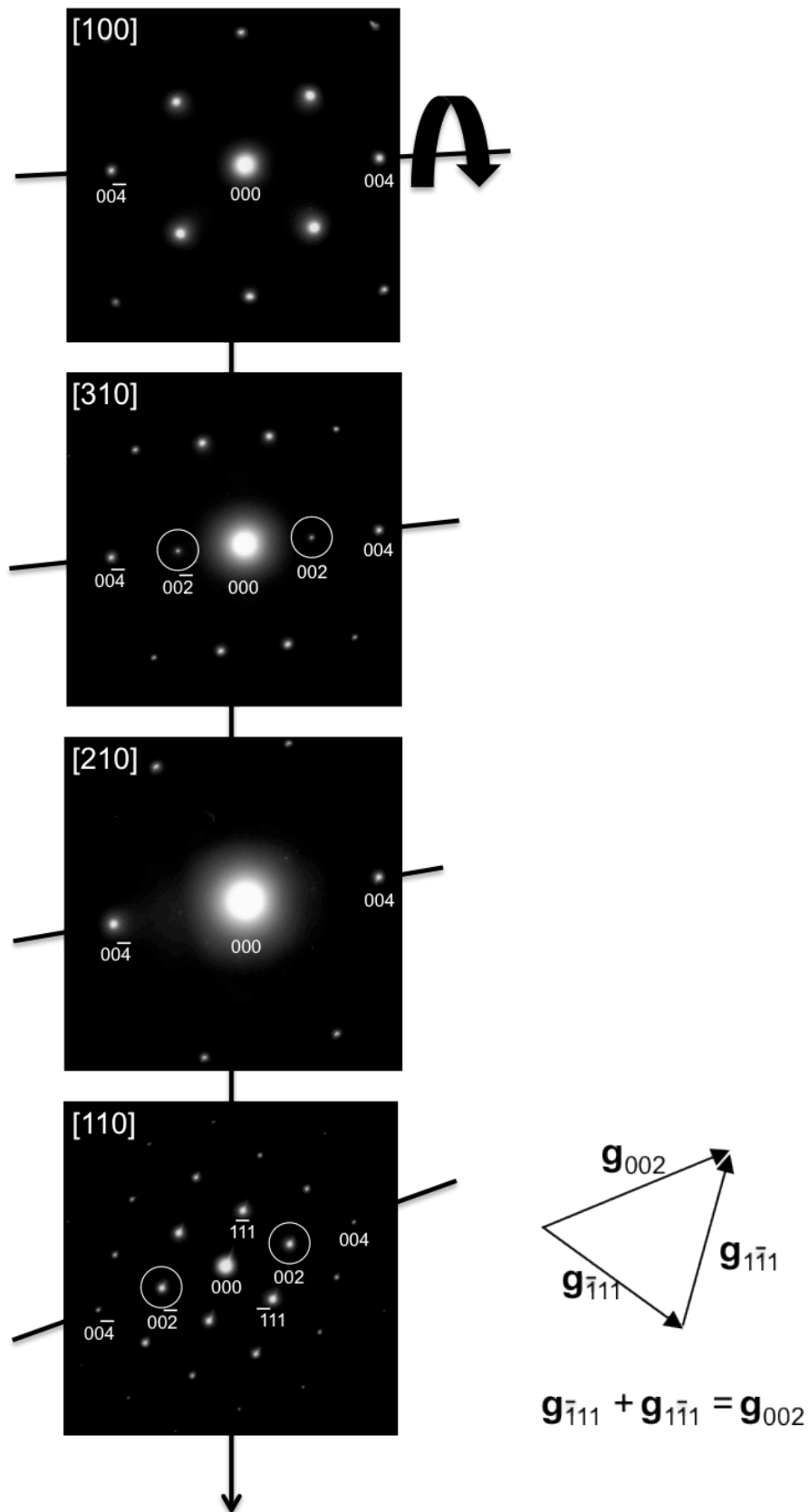


Figure 5.7: SADPs with common row $00l$. The kinematically forbidden diffraction spots, 002 and $00\bar{2}$ (circled), are visible in some projections due to dynamical effects (multiple scattering). The conditions of Umweganregung for the 002 reflection are shown in the figure in the lower right corner.

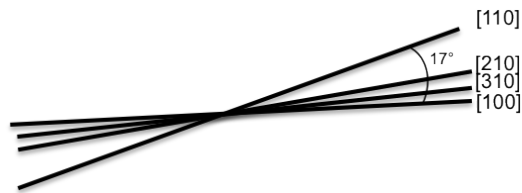


Figure 5.8: Relative rotation of diffraction patterns $[100]$ to $[110]$.

Due to the d glide plane of the $Fd\bar{3}m$ space group (cf. Section 3.2.4), the 002 (and equivalently 200 , 020 , $00\bar{2}$, etc.) diffraction spots are kinematically forbidden in the diffraction patterns for silicon. However, when the crystal is viewed along certain zone axes, the conditions for Umweganregung are satisfied for these reflections (cf. Section 4.3.1). The effect is visible in the $[310]$ and $[110]$ planes in Figure 5.7, and it is shown how the lattice vectors of the $\bar{1}11$ and $1\bar{1}1$ reflections in $[110]$ add to give the lattice vector of 002 .

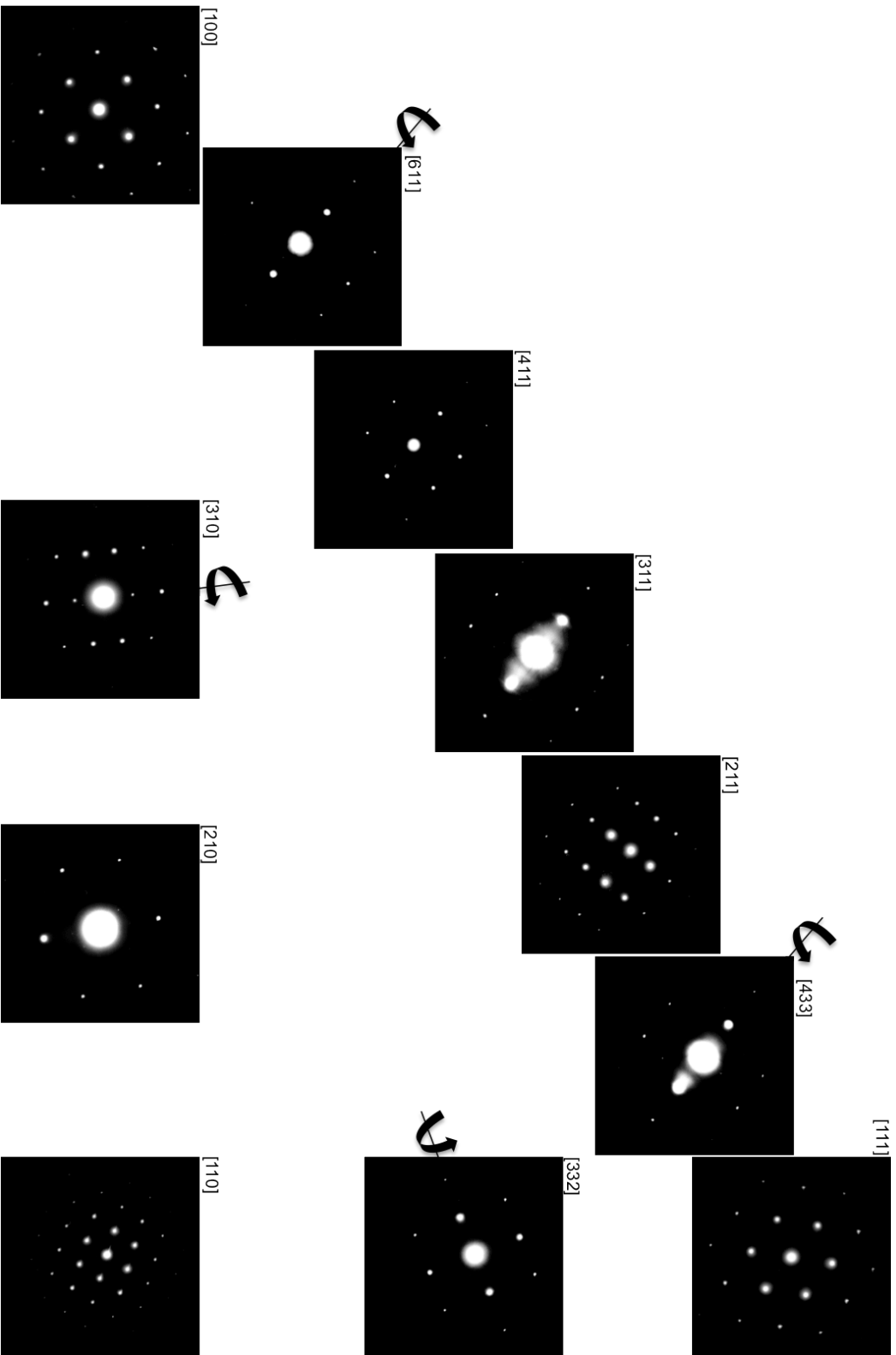


Figure 5.9: Tilt series of silicon confirming a cubic structure with space group $Fd\bar{3}m$ and lattice parameter $a = 5.43 \text{ \AA}$.

To visualize the structure, the 3D computer graphics program *Google Sketchup* [29] was utilized. Figure 5.10 illustrates the procedure of constructing the reciprocal lattice: A model of each of the projections from the tilt series is made individually, and planes with a common row are assembled and tilted about this row relative to one another based on the experimental tilt angles. The three-dimensional model of the reciprocal lattice of silicon can be seen in Figure 5.11. The kinematically forbidden diffraction spots that appeared in the tilt series are coloured black in the model, and the outline of the reciprocal unit cell is marked with a grey box.

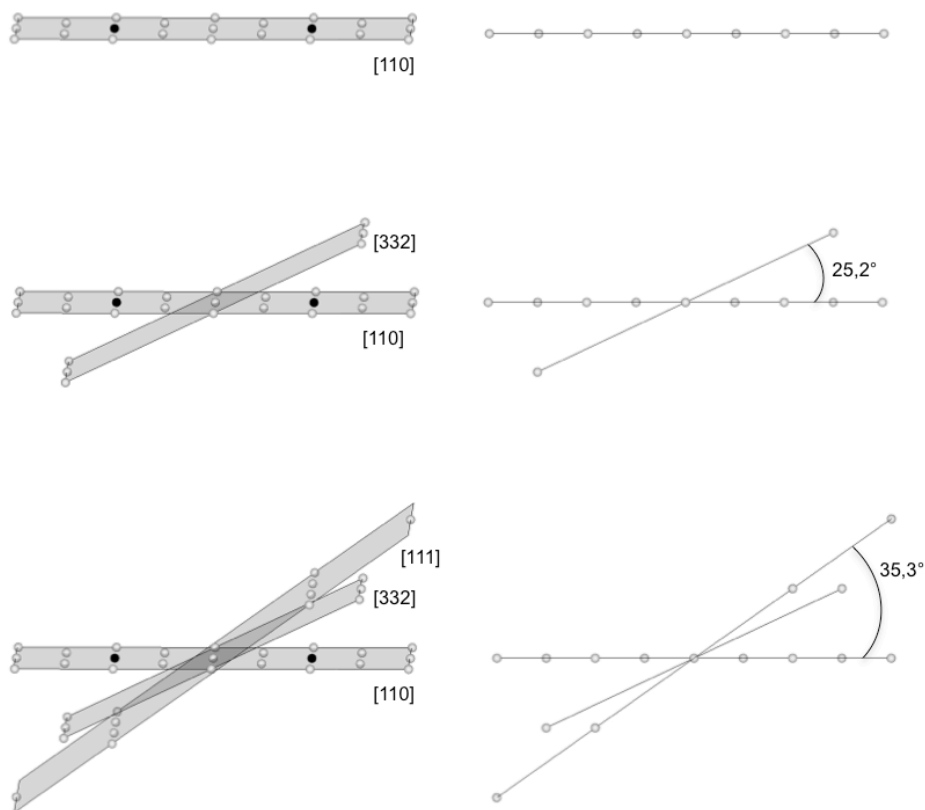


Figure 5.10: Procedure of constructing a model of the reciprocal lattice in Google Sketchup.

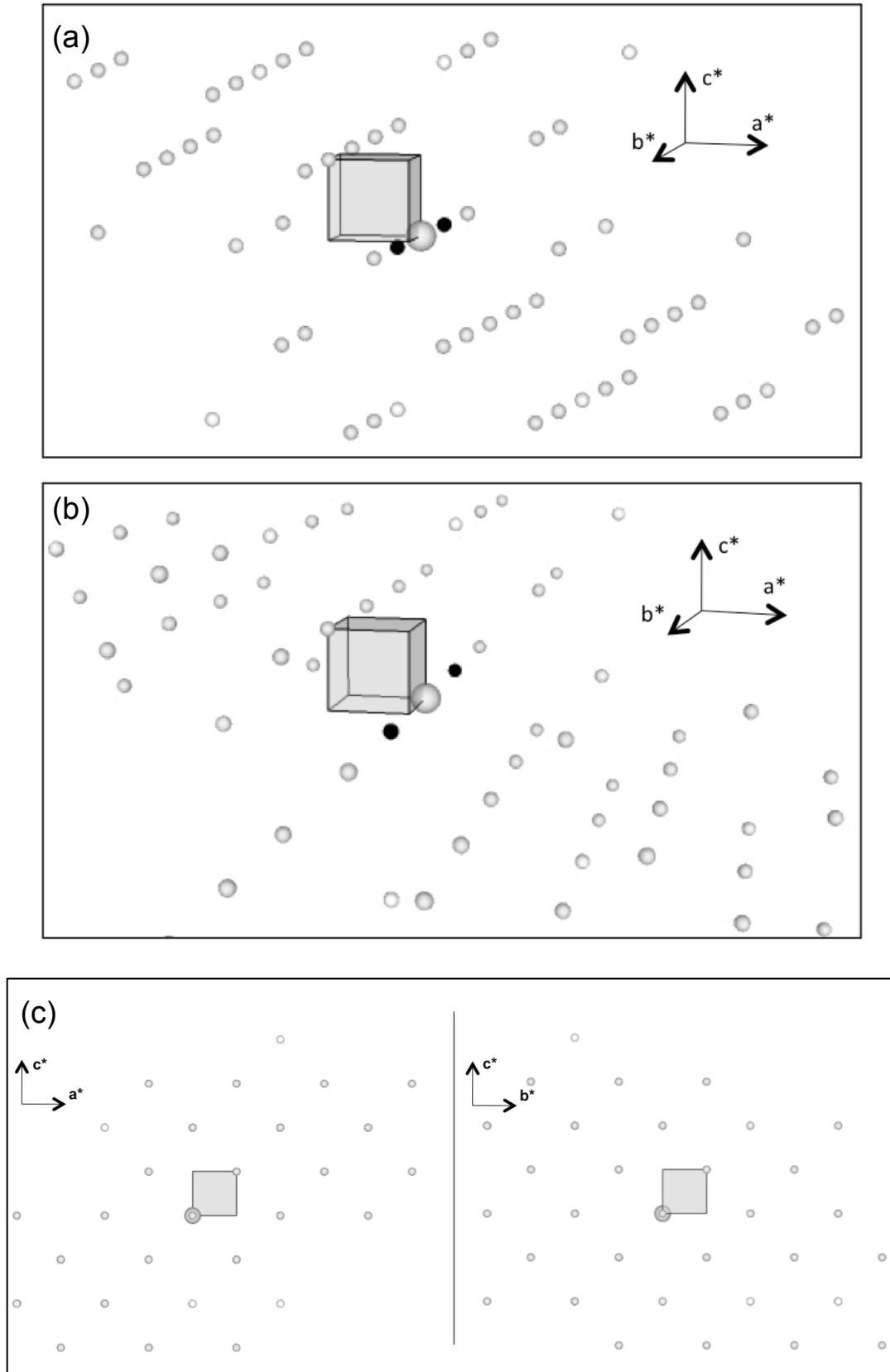


Figure 5.11: 3D models of the reciprocal lattice for silicon in (a) parallel view, (b) perspective view and (c) parallel view along the a^* and b^* axes. The kinematically forbidden diffraction spots that appeared in the tilt series are coloured black. The grey box marks the outline of the reciprocal unit cell.

5.1.6 Electron diffraction of NiLN3-1300

The sample of NiLN3-1300 was examined in the TEM by selected area electron diffraction. The sizes of the grains analysed ranged from 1-5 μm . EDS analysis was performed on each grain prior to the diffraction analysis in order to make sure the correct phase was being studied. In addition to several single images and short tilt series, three complete tilt series were recorded from three different grains, labelled A, B and C. The tilt series will be referred to as tilt series A, B and C, consistent with their respective grains. Tilt series A was recorded on the 2010F microscope, and tilt series B and C were recorded on the 2000FX microscope.

The d -values for three unrelated reflections were calculated for each diffraction pattern (cf. Section 5.1.1.1), and the reciprocal lattices of the structures were modelled in Google Sketchup based on the tilt series. From this model the lattice parameters could be determined, and the diffraction patterns were indexed and their zone axes calculated (cf. Section 3.3).

5.2 Compositional analysis with TEM and SEM

When the electron beam interacts with the specimen, different types of signals are generated, among them characteristic X-rays that can give quantitative chemical information about the sample. The technique of collecting and analysing these X-rays is called Energy Dispersive X-ray Spectroscopy (EDS, EDX, EDAX). The process of generating X-rays is illustrated in Figure 5.12: A core (inner shell) electron is knocked away by an incoming electron, leaving the atom in an excited state. An outer shell electron will fill the hole left behind by the core electron, and will lose an amount of energy equal to the energy difference of the core shell and outer shell. This energy is emitted as a characteristic X-ray. Continuum X-rays, or bremsstrahlung, arise when the incident electrons decelerates in the electric field associated with the atom, and is the main contributor to the background in EDS spectra.

Orbital energies are unique to each atomic element, and so the emitted x-rays give quantitative information about the elements present in the sample.

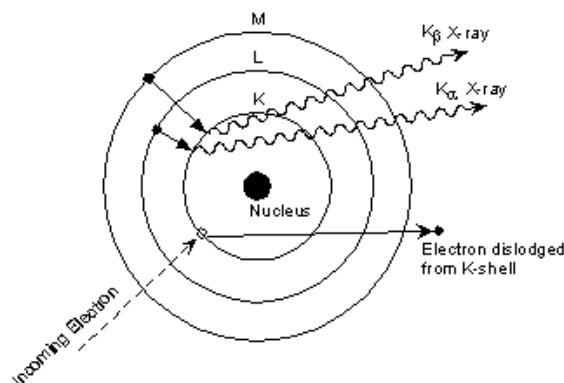


Figure 5.12: Principle of EDS (left) and example of EDS spectre (right) [30].

5.2.1 EDS spot analysis and element mapping with SEM

In addition to quantitative EDS analysis, the scanning electron microscope (SEM) can provide qualitative chemical information and information about the surface topography of the sample. Compared to the TEM, the microscope is operated at a relatively low voltage (typically 0.5 to 30 kV), and the electron beam is focused by electromagnetic lenses and scanned over the sample. Unlike the TEM, the signals detected in the SEM are the electrons that scatter from the surface of the sample. The processed information can be viewed on a computer display as images. The chemical information comes from backscattered electrons (BSE), which are the results of elastic scattering of the incoming electrons. The compositional images give information about the relative atomic density of the sample; heavier elements scatter more strongly (and therefore appear brighter in the images) than lighter elements. The topographic information comes from secondary electrons (SE), which are low-energy electrons (< 50 eV) produced by inelastic scattering.

The sampling volume in SEM depends upon many factors, but the acceleration voltage and density of the sample are the most important ones. As seen in the

schematic figure in Figure 5.13, the excitation volume is a balloon-shaped region penetrating into the sample, generally ranging from 1-5 μm [31]. This is significantly larger than the sampling volume in the TEM; as the TEM samples are very thin, only the “neck” of the balloon will interact with the sample, giving a much higher spatial resolution than in the SEM.

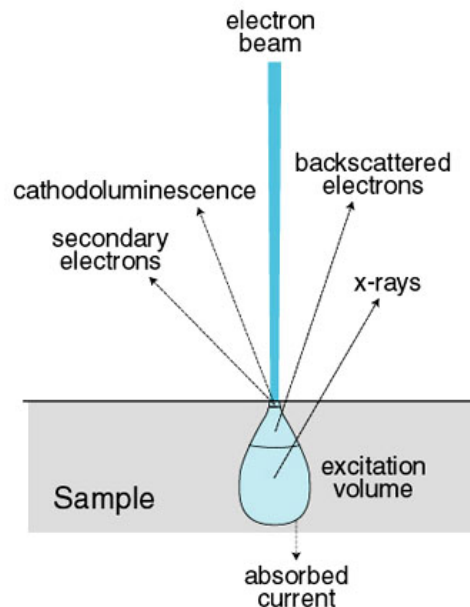


Figure 5.13: Schematic figure of excitation volume in the SEM. The general penetration depth of the beam is in the range 1-5 μm [31].

In the present study, a field emission gun scanning electron microscope (SEM; FEG Quanta 200 FEI) with an EDS (EDAX) detector was used. The TEM-sample of NiLN3-1300 was analysed. The EDS and BSE image revealed four different compositions in the sample (see Figure 5.14). To produce enough X-rays the analysis had to be performed away from the edge of the hole, but large areas (including the edge) was examined in the BSE mode, and there was not detected any large deviations in the distribution of the phases.

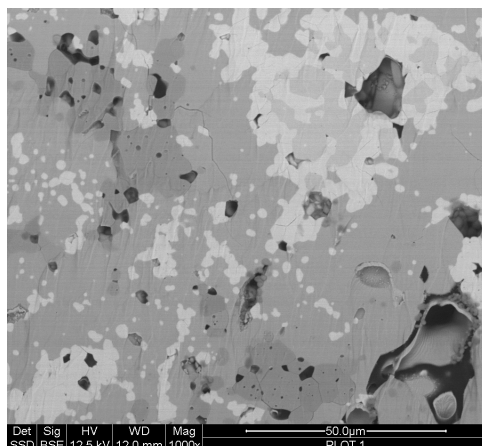


Figure 5.14: BSE image showing the NiLN3-1300 TEM sample.

Two EDS techniques were performed: Spot analysis and element mapping. For the spot analysis an acceleration voltage of 12.5 keV was used, as this was sufficient to obtain enough counts. Spots were chosen within the areas of different brightness in the BSE image, and spectra were recorded and quantified. Element mapping is a technique to qualitatively show the distribution and concentration of individual elements contained in the sample. The elements to be detected are selected beforehand, and the results are displayed in individual, single-colored images for each element. The distribution and brightness of the color indicates the concentration of that element – the brighter the color the higher the concentration.

For this mapping, the area of Figure 5.14 was scanned, and Ni, Nb, O, La and Ca (dopant) were selected for detection. The mapping was then run overnight (for about 15 hours) at an acceleration voltage of 20 keV. A higher acceleration voltage was chosen than for spot analysis in order to collect the data in a shorter amount of time.

5.2.2 EDS spot analysis with TEM

EDS spot analysis was performed with TEM by focusing the electron beam on a thin part of the grain of interest, and record an EDS spectrum. The grains analysed were in the range 1 – 5 μm , and since the probe sizes are in the

nanometre range, there was little to no risk of receiving signals from adjacent grains. The sampling volume is limited by the illuminated area and the specimen thickness, which means that very good spatial resolution can be achieved with a fine probe and a thin sample.

EDS analysis was performed with the 2000FX and the 2010F microscope, and the sample holder was tilted about 10° towards the detector (to improve the collection of X-rays). The grain from which tilt series A was recorded and three random grains were analysed in the 2010F. SADPs were also recorded from two of the last three grains. Both tilt series B and C were recorded on the 2000FX microscope, and EDS analysis was performed in the same session as the tilt series was recorded. However, these analyses were performed just to check that the desired phase was analysed, and not to properly quantify the elements present. The conditions during the EDS analysis (tilting of the stage, count time, dead time) were therefore not optimal. The quantified values were only noted for grain B. For grain C it was decided to do proper chemical analysis on the 2010F microscope since oxygen could be detected. However, a piece of the specimen with the grain broke off before the attempted analysis, and no EDS results for this grain were recorded.

6 Results and discussion

6.1 Compositional analysis

The EDS analysis in the SEM suggests the presence of NiO, LaNbO₄, LaNb₃O₉, as well as two Ni-Nb-O phases; One with Ni:Nb ratio close to 2 and the other with Ni:Nb-ratio close to 3. Figure 6.1 shows the result from the elemental mapping, and the quantified results from the spot analysis are listed in Table 6.1. The Ni:Nb ratios measured at position 5 and 7 differ by as much as 30 % in the two measurements, but neither the BSE image nor the elemental mapping images show any contrast between the two analysed areas. From these images there seems to be a uniform phase containing Ni, Nb and O together with the other three identified phases. SEM is considered a semi-quantitative analysis method [32], and the results may be influenced by several factors both regarding the instrumental conditions and the specimen itself.

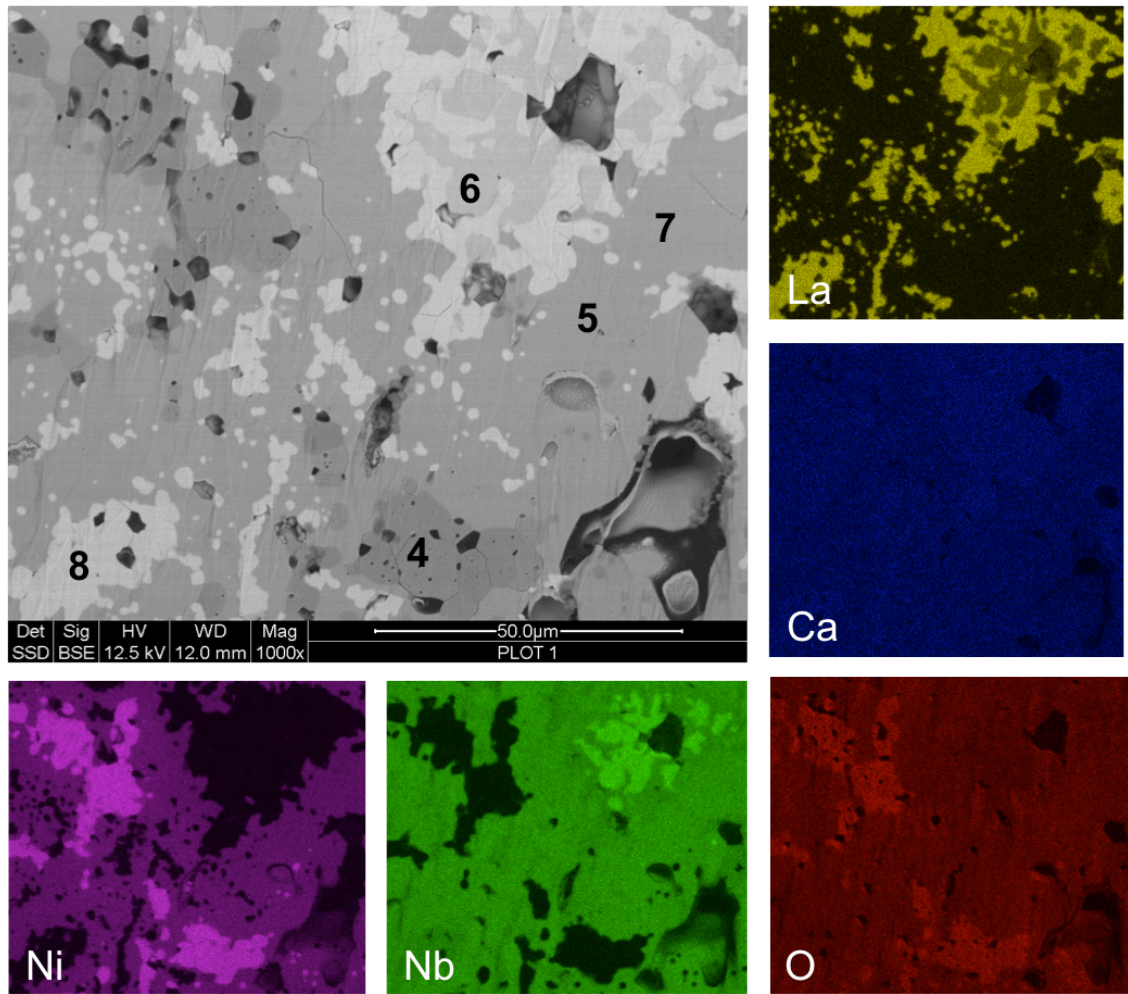


Figure 6.1: BSE image surrounded by colored elemental contrast images of the same area. The brighter the color the more concentration of the specified element. The numbers in the BSE image indicate positions for spot analysis.

Table 6.1: Quantified results from SEM EDS analysis.

Spot position	Ni	Nb	La	O	Ni:Nb ratio	Possible structure
4	34.65	02.80	-	26.21	12.4	NiO
5	38.28	13.11	-	31.37	2.92	?
6	3.02	6.96	2.36	12.22	0.43	LaNb ₃ O ₉
7	25.03	12.69	1.20	28.46	1.97	Ni ₄ Nb ₂ O ₉
8	7.74	12.79	11.75	27.86	0.61	LaNbO ₄

For the EDS analysis in the TEM, only nickel and niobium were selected for quantification. In the 2010F microscope, oxygen was also detected in all the grains but was not quantified. The results are listed in Table 6.2. The positions 2 and 3 are indicated in the TEM image in Figure 6.2 a. The image of the whole area (including position 1) is shown in the BSE image in Figure 6.2 b with positions 1, 2 and 3 indicated.

Table 6.2: Quantified results from TEM EDS analysis.

Instrument	Grain/spot position	Element [At%]		Ni:Nb ratio
		Ni	Nb	
TEM (2010F)	A	71.50 (± 0.80)	28.50 (± 0.91)	2.5
	1	73.27 (± 0.39)	26.73 (± 0.43)	2.7
	2	72.71 (± 0.39)	27.29 (± 0.43)	2.7
	3	75.25 (± 0.41)	24.75 (± 0.42)	3.0
TEM (2000FX)	B	77.10 (± 1.43)	22.99 (± 1.34)	3.4

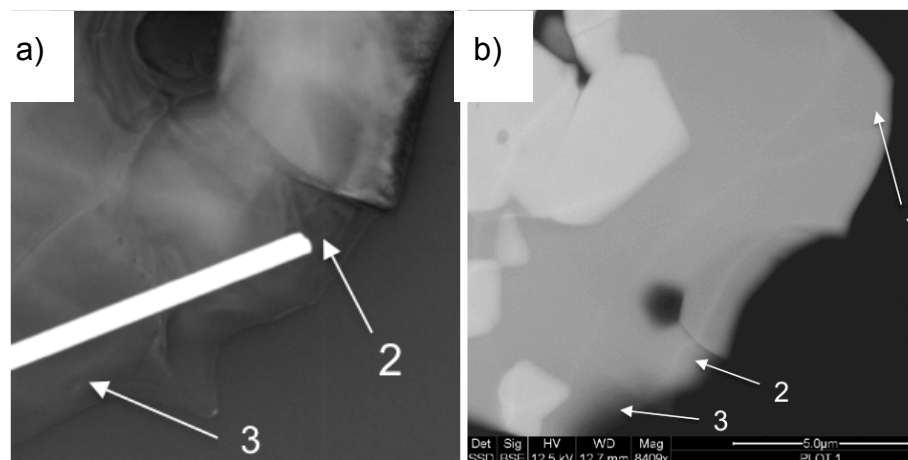


Figure 6.2: TEM image (a) of area containing spot analysis positions 1 and 2, and SEM BSE image (b) of area containing spot analysis positions 1, 2 and 3. The bright white line is the TEM indicator pointing at position 2.

The ratios from the grains analysed in the 2010F microscope are consistent with those from the EDS analysis in the SEM, and also with the compositional analysis performed by Magrasó et al. (cf. Section 2.1). The Ni:Nb ratio from grain B analysed in the 2000FX is relatively large compared to the rest, and the error in the amount of Ni and Nb is also larger (see the table). This may be due to the fact that the conditions during the EDS analysis (tilting of the stage, count

time, dead time) were not optimal (cf. Section 5.2.2), and the quantified result is therefore less reliable.

As can be seen in Figure 6.3, the diffraction patterns taken at position 1 and 2 are similar both to each other and to the diffraction pattern from the $[32\bar{1}]$ zone axis from tilt series B (cf. Section 6.2.2). The lattice distances for the three patterns are listed in Table 6.3, along with the measured distances, R_1 , R_2 and R_3 (cf. Section 5.1.1.1). The directions of the measured distances are indicated only in Figure 6.3 b, but apply to all three patterns. There are slight differences in the d -values, but diffraction focus and height can account for this discrepancy [33]. Also, the diffraction pattern from grain B was obtained in the 2000FX microscope, while the other two were obtained in the 2010F microscope. The diffraction patterns are most likely from the same type of structure, supporting the previous assumption about one single Ni-Nb-O phase.

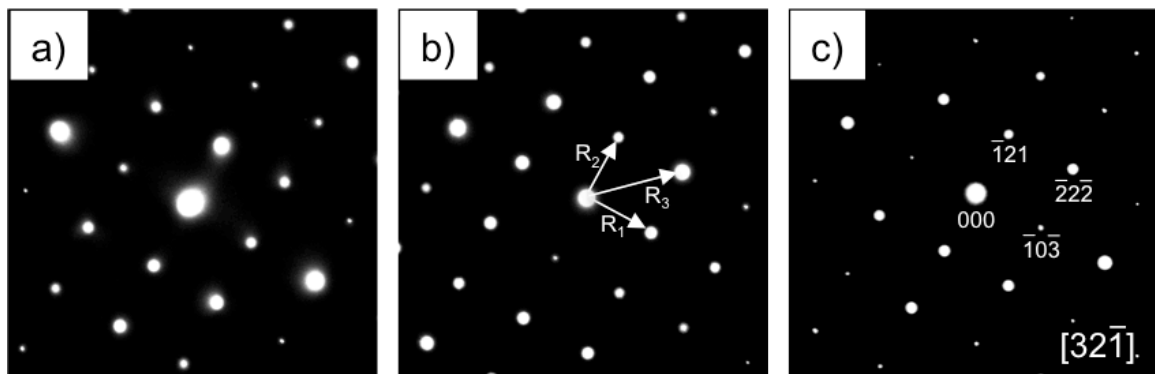


Figure 6.3: SADPs from spot position 1 (a) and 2 (b), and from the $[32\bar{1}]$ zone axis from tilt series B (c). The last pattern is rotated to match the orientation of the other two. The arrows in b indicate the measured distances R_1 , R_2 and R_3 used in the calculation of d -values.

Table 6.3: Measured R -values and lattice distances, d , from spot positions 1 and 2 and from the $[32\bar{1}]$ zone axis from tilt series B.

Grain/spot position	R_1 [cm]	R_2 [cm]	R_3 [cm]	d_1 [Å]	d_2 [Å]	d_3 [Å]
1	0.294	0.271	0.401	5.122	5.557	3.756
2	0.299	0.291	0.404	5.037	5.175	3.728
B	0.294	0.270	0.396	5.071	5.522	3.765

Although the EDS results from grain C was not put on record (cf. Section 5.2.2), it did confirm the presence of Ni, Nb and O, with a Ni:Nb ratio of 2-3 (all grains analysed were within this range, except for grain B [see above]). According to the elemental mapping in the SEM, the other phases present in the sample are NiO, LaNb₃O₉, and LaNbO₄. All of these have structures with lattices and lattice parameters that are very different and easily distinguishable from the one found by tilt series C (reference [12] and references therein). It is therefore most probable that tilt series C was recorded from a grain of a Ni-Nb-O phase.

6.2 Identifying the lattice - tilt series analysis

Based on the compositional analysis, there seems to be only one Ni-Nb-O phase present in the sample. However, the three tilt series A, B and C obtained from three different grains with similar compositions revealed three different structures.

The *d*-values from tilt series B and C were calculated using the calibrated camera length(s) for the 2000FX microscope from section 5.1.5.1. Zone axes and the theoretical angles between zone axes were calculated using equations (3.8), and (3.9), respectively.

6.2.1 Tilt series A

Figure 6.4 shows the SADPs of tilt series A, and the Google Sketchup model is shown in Figure 6.5. From the tilt series the reciprocal lattice was identified as orthorhombic, with lattice parameters $a = 5.04 \text{ \AA}$, $b = 9.00 \text{ \AA}$ and $c = 14.20 \text{ \AA}$. These are consistent with the lattice parameters reported for II-Ni₄Nb₂O₉ by Wichmann et al. (cf. Table 2.1). The experimental angles between the SADPs show reasonable agreement with the calculated values; both are listed in Table 6.4. To reach the $[20\bar{1}]$ zone axis the beam had to be tilted (cf. Section 5.1.2), which may account for the relatively large deviation of 4.1° between the experimental and calculated angles between the $[3\bar{1}\bar{2}]$ and $[20\bar{1}]$ zone axes.

Table 6.4: Calculated and experimental angles between the zone axes in tilt series A.

Zone axes	Experimental angles	Calculated angles
$[4\bar{1}\bar{1}]$ and $[3\bar{1}\bar{1}]$	8.6°	8.2°
$[3\bar{1}\bar{1}]$ and $[2\bar{1}\bar{1}]$	11.2°	11.0°
$[2\bar{1}\bar{1}]$ and $[3\bar{2}\bar{2}]$	7.2°	6.7°
$[3\bar{2}\bar{2}]$ and $[1\bar{1}\bar{1}]$	6.9°	7.5°
$[1\bar{1}\bar{1}]$ and $[1\bar{2}\bar{2}]$	8.7°	8.2°
$[1\bar{2}\bar{2}]$ and $[0\bar{1}\bar{1}]$	6.5°	8.6°
$[3\bar{3}\bar{1}]$ and $[2\bar{2}\bar{1}]$	8.9°	9.0°
$[2\bar{2}\bar{1}]$ and $[3\bar{3}\bar{2}]$	7.8°	8.0°
$[3\bar{3}\bar{2}]$ and $[4\bar{4}\bar{3}]$	3.4°	3°
$[4\bar{4}\bar{3}]$ and $[1\bar{1}\bar{1}]$	8.0°	8°
$[1\bar{1}\bar{1}]$ and $[2\bar{2}\bar{3}]$	10.4°	10.0°
$[2\bar{2}\bar{3}]$ and $[1\bar{1}\bar{2}]$	5.7°	5.8°
$[1\bar{1}\bar{1}]$ and $[3\bar{1}\bar{2}]$	16.6°	16.8°
$[3\bar{1}\bar{2}]$ and $[20\bar{1}]$	12.7° + beam tilt	16.8°

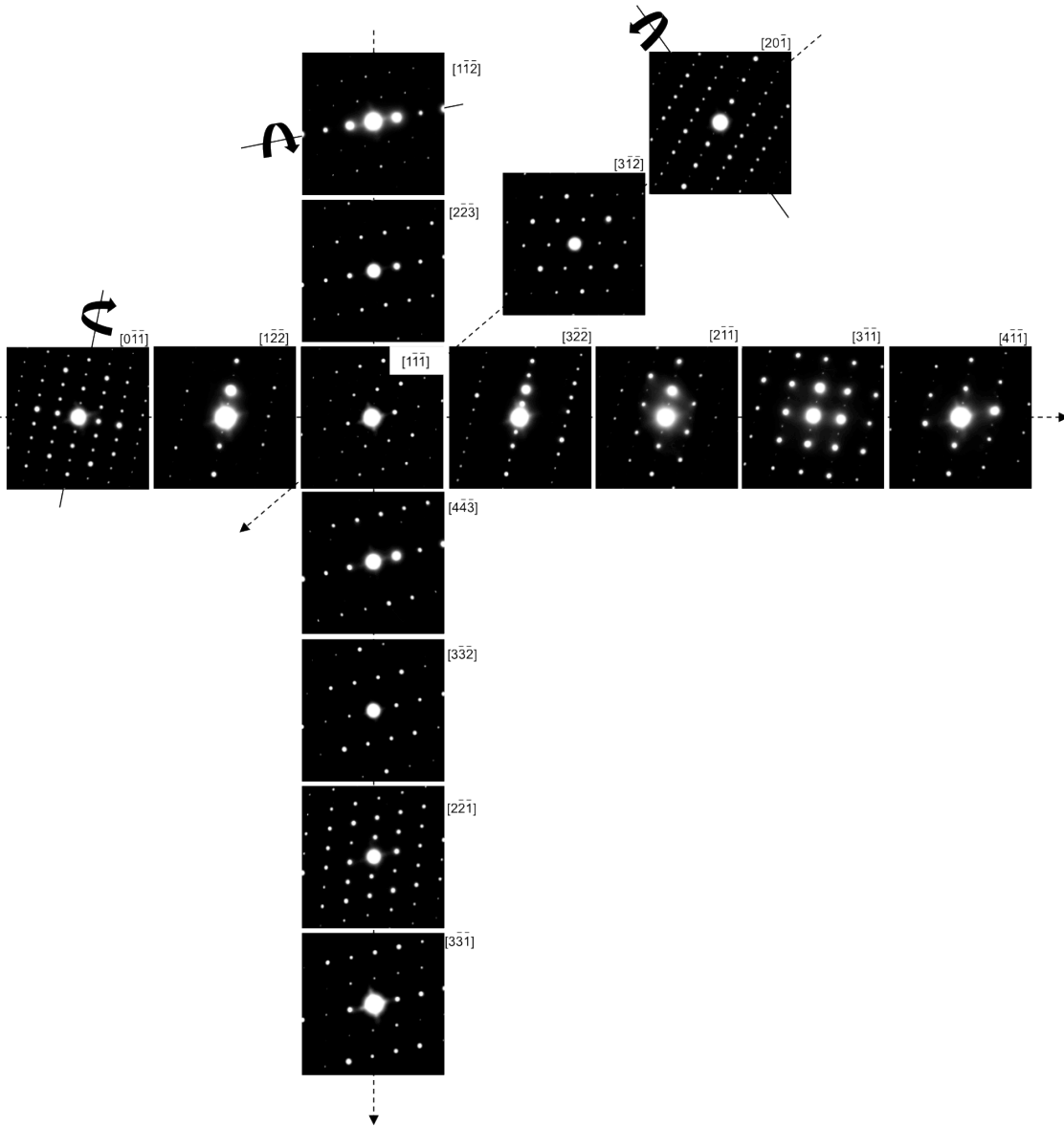


Figure 6.4: Tilt series A, revealing an orthorhombic lattice with lattice parameters $a = 5.04 \text{ \AA}$, $b = 9.00 \text{ \AA}$ and $c = 14.20 \text{ \AA}$. Diffraction patterns along the same dashed line are tilted about the same axis, which in turn is indicated by a solid line.

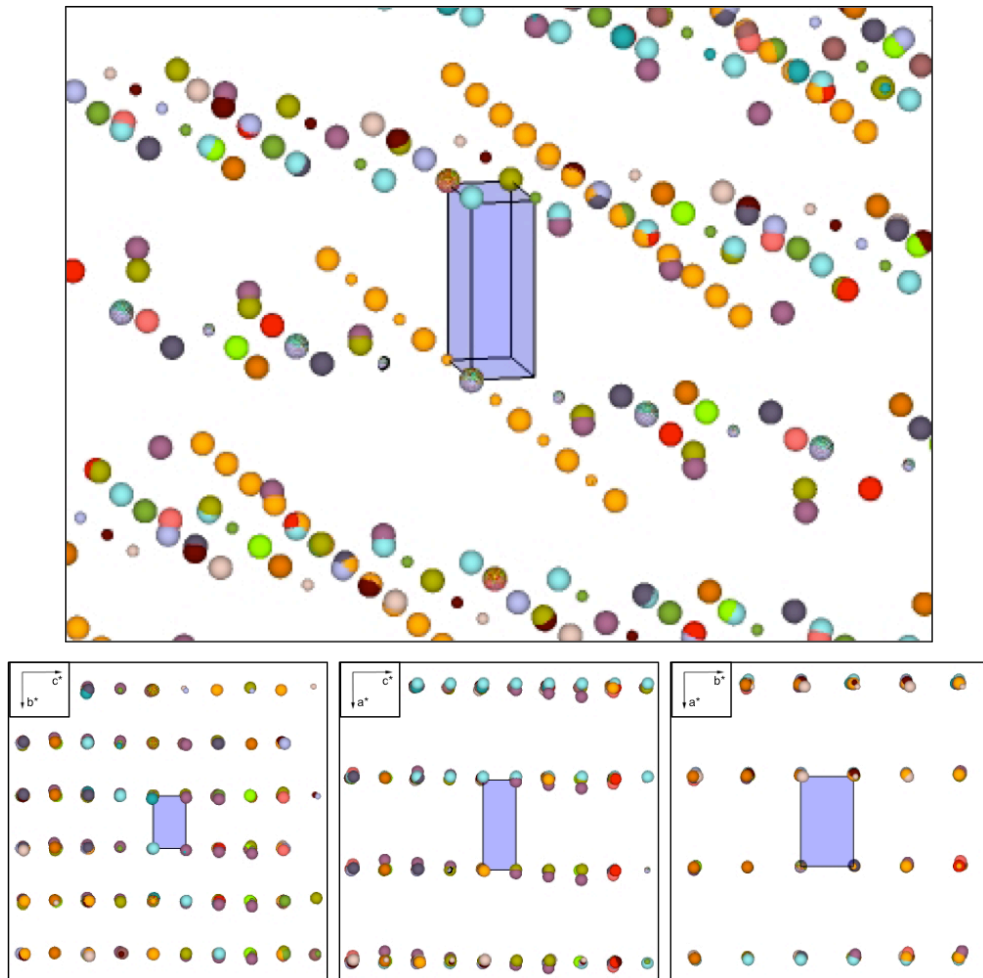


Figure 6.5: Top: Model of the reciprocal lattice from tilt series A. The blue box indicates the smallest unit in the orthorhombic lattice. Bottom three from left to right: Parallel view of the lattice along the a^* , b^* and c^* axes.

In Figure 6.6 a selection of the patterns from the tilt series shown in Figure 6.4 are magnified and indexed. The diffraction patterns reveal no systematic extinctions, although many of them have very low intensities. This should imply that the structure is primitive with no microscopic symmetry elements (cf. Section 3.2.3), consistent with space groups $Pmm2$ (no. 25) and $Pmmm$ (no. 47). However, further analysis is needed in order to evaluate if any of the reflections seen are due to dynamical effects (see section 4.3), which would imply the presence of glide planes and/or screw axes.

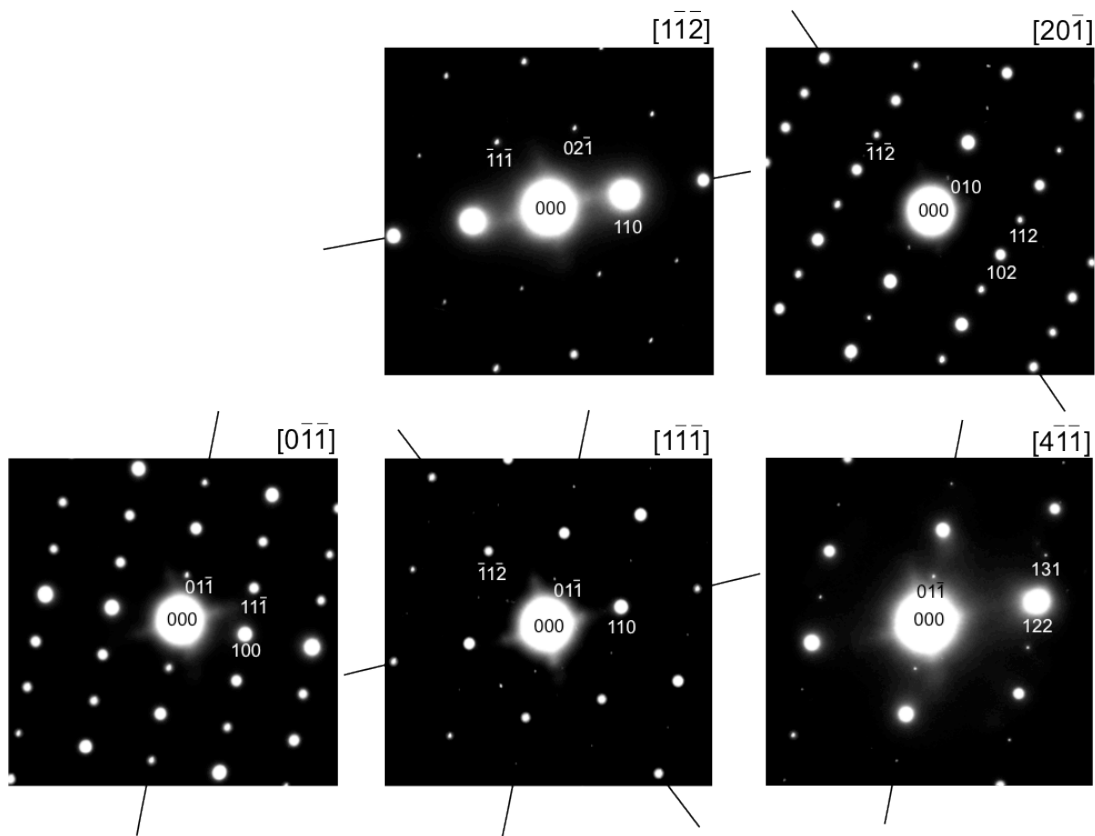


Figure 6.6: The diffraction patterns reveal no systematic extinctions, although many of them are very weak. The lines indicate which patterns are tilted about the same row.

In addition to the weak reflections indexed in the zero order Laue zone (ZOLZ) pattern (cf. Section 4.2) even weaker reflections are observed in the diffraction pattern from the $[4\bar{4}\bar{3}]$ zone axis (see Figure 6.7). These were at first suspected to be nearly extinct ZOLZ reflections, which would have resulted in a lattice with different parameters than the ones stated in the beginning of this section. However, they were identified as reflections from first order Laue zones (FOLZ). In the right picture in the figure, a Google Sketchup model of the reciprocal lattice with parameters $a = 5.04 \text{ \AA}$, $b = 9.00 \text{ \AA}$ and $c = 14.20 \text{ \AA}$ is viewed along the $hh0$ row (110, 220, etc.). The reflections of the $[4\bar{4}\bar{3}]$ zone axis are colored black. The grey region represents the reflections from both ZOLZ and FOLZ intersecting the Ewald sphere due to form effects. The reciprocal lattice points are elongated due to the thin sample (cf. Section 4.2).

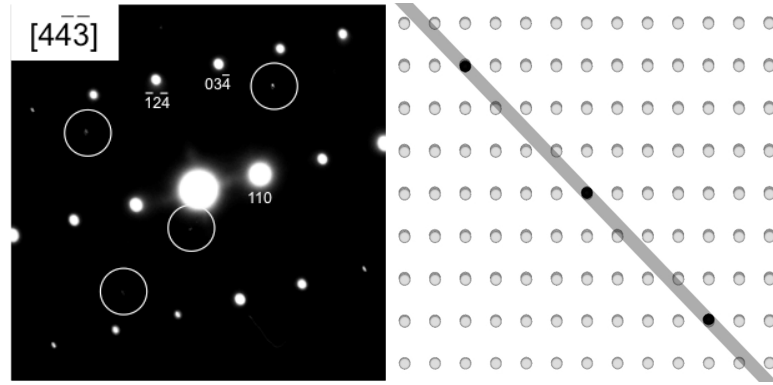


Figure 6.7: Left: Diffraction pattern from the $[4\bar{4}\bar{3}]$ zone axis. Some of the FOLZ reflections are circled. Right: View along the $hh0$ row (110, 220, etc.) of the $[4\bar{4}\bar{3}]$ zone axis (black dots) in a lattice with parameters $a = 5.04 \text{ \AA}$, $b = 9.00 \text{ \AA}$ and $c = 14.20 \text{ \AA}$.

6.2.2 Tilt series B

Figure 6.8 shows the SADPs of tilt series B, and the Google Sketchup model is shown in Figure 6.9. From the tilt series it was possible to identify an orthorhombic reciprocal lattice, with real space lattice parameters $a = 10.14 \text{ \AA}$, $b = 14.17 \text{ \AA}$ and $c = 17.51 \text{ \AA}$, consistent with previous reported structures by Bertaut et al. [15] and Burdese et al. [16] (cf. Section 2.2. The experimental and calculated angles between the SADPs are listed in Table 6.5.

Table 6.5: Calculated and experimental angles between the zone axes in tilt series B.

Zone axes	Experimental angles	Calculated angles
$[010]$ and $[36\bar{1}]$	21.9°	22.2°
$[36\bar{1}]$ and $[34\bar{1}]$	9.4°	9.3°
$[34\bar{1}]$ and $[32\bar{1}]$	19.4°	19.3°
$[32\bar{1}]$ and $[31\bar{1}]$	16.4°	17.0°
$[31\bar{1}]$ and $[30\bar{1}]$	23.3°	22.2°
$[30\bar{1}]$ and $[50\bar{1}]$	10.0°	10.9°
$[50\bar{1}]$ and $[100]$	18.6°	19.1°
$[100]$ and $[310]$	23.4°	25.3°
$[310]$ and $[210]$	9.8°	10.0°
$[210]$ and $[320]$	7.7°	8.1°
$[320]$ and $[110]$	11.3°	11.4°
$[110]$ and $[010]$	35.6°	35.2°

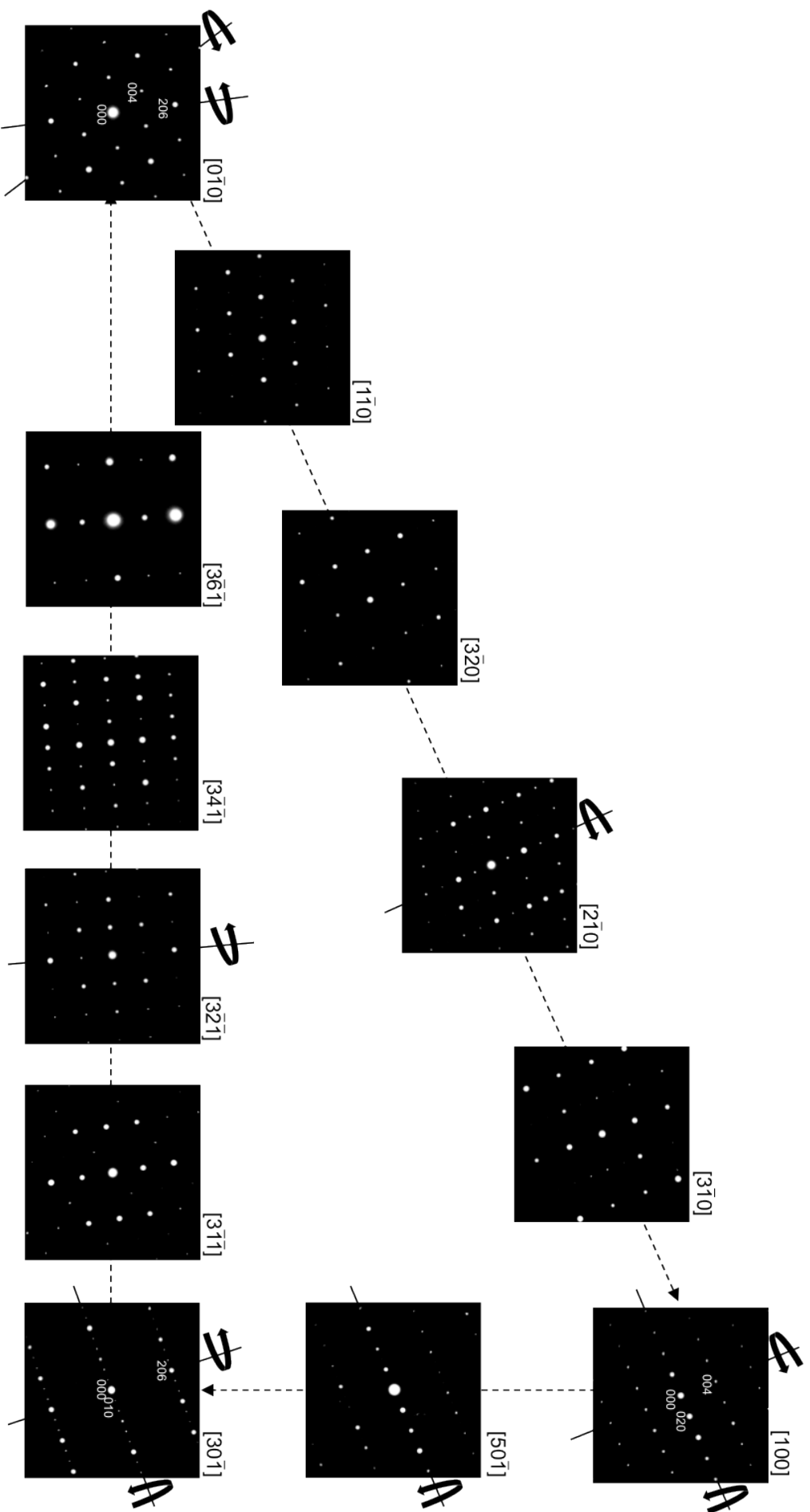


Figure 6.8: Tilt series B, consistent with an orthorhombic lattice with lattice parameters $a = 10.14 \text{ \AA}$, $b = 14.17 \text{ \AA}$ and $c = 17.51 \text{ \AA}$. Diffraction patterns along the same dashed line are tilted about the same axis, which in turn is indicated by a solid line.

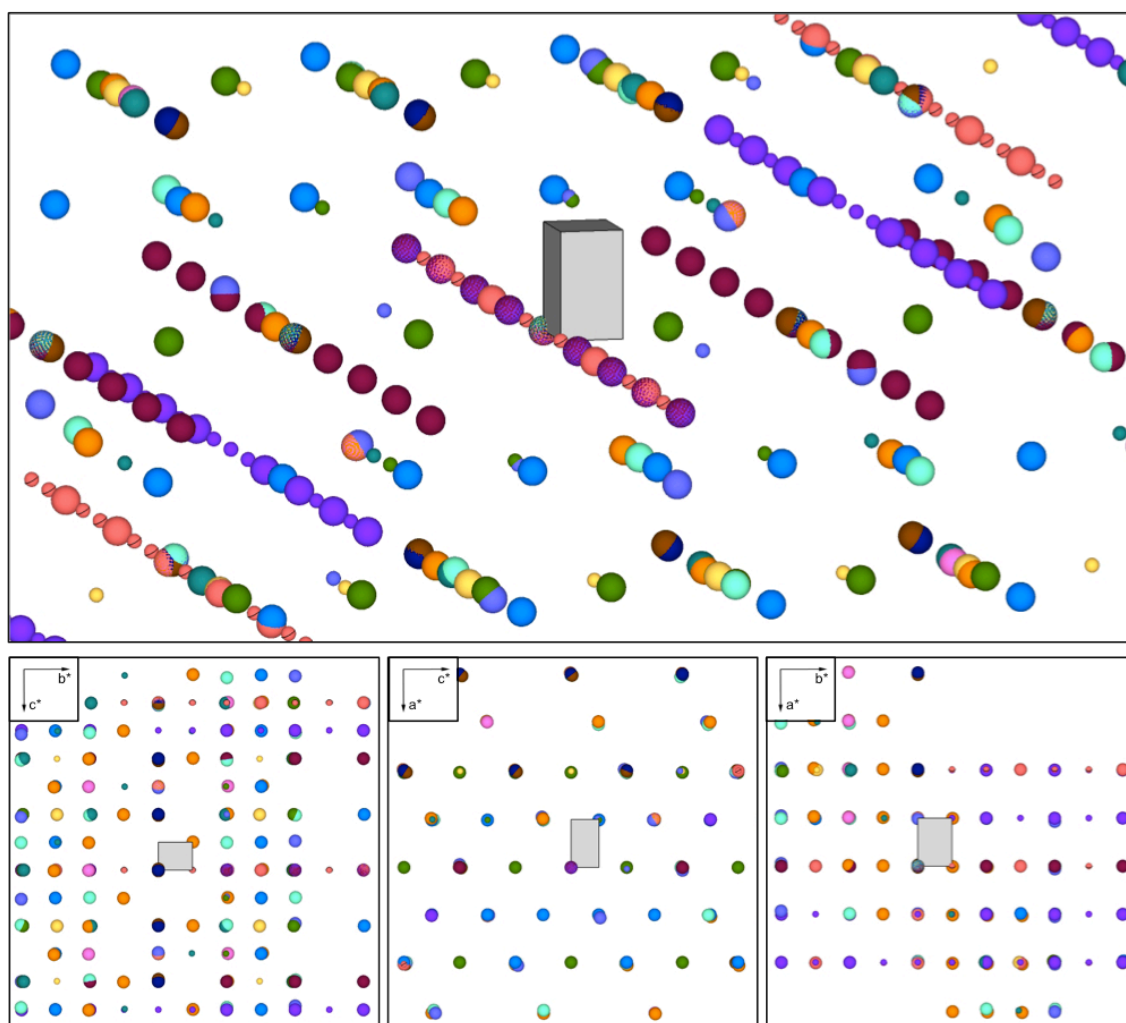


Figure 6.9: Top: Perspective view of the model of the reciprocal lattice from tilt series B. The grey box indicates the smallest unit in the orthorhombic lattice. Bottom three from left to right: Parallel view of the lattice along the a^* , b^* and c^* axes.

A selection of diffraction patterns from the tilts series are enlarged and indexed according to the orthorhombic lattice identified in Figure 6.10. Several extinctions are observed, and some reflections (such as 002, 010 and 130) can appear due to dynamical scattering (cf. Section 4.3). To investigate possible space groups, conditions limiting possible reflections have been considered. Several extinctions can be seen in the tilt series.

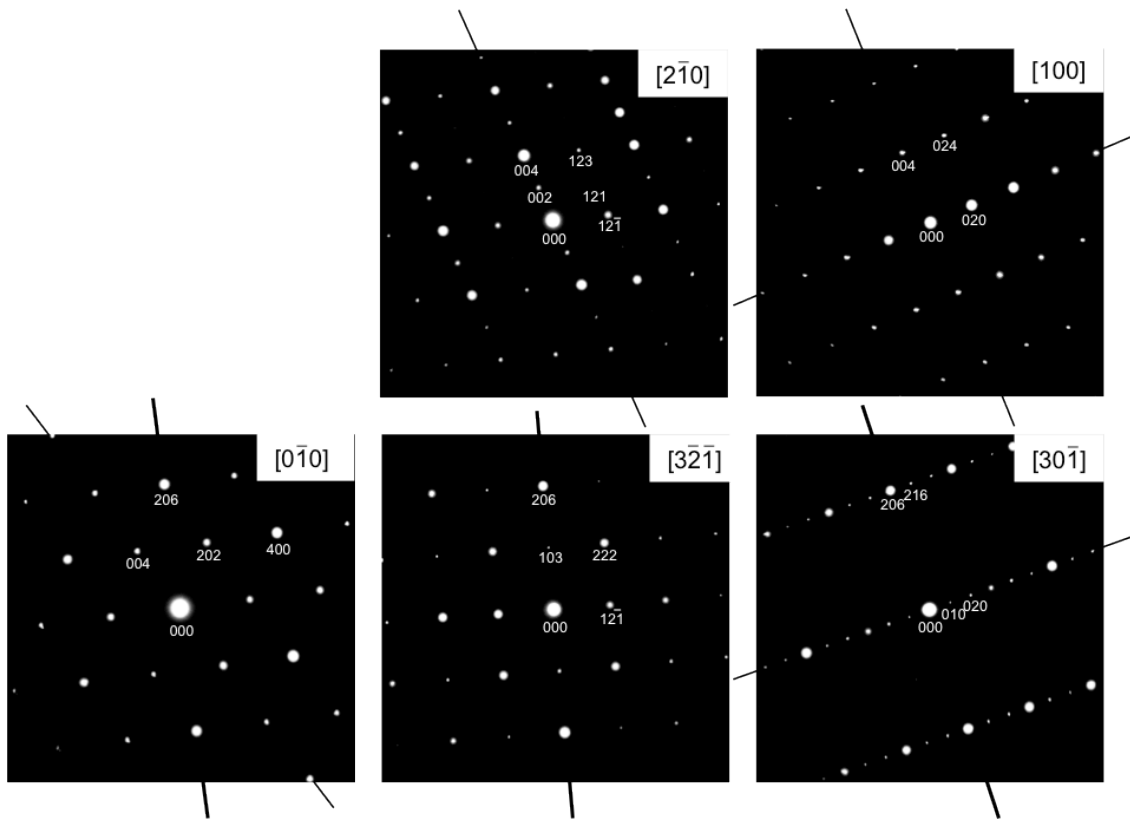


Figure 6.10: Indexed patterns from tilt series B according to a primitive lattice with lattice parameters $a = 10.14 \text{ \AA}$, $b = 14.17 \text{ \AA}$ and $c = 17.51 \text{ \AA}$.

From the zone axes $[100]$ and $[0\bar{1}0]$ seen in Figure 6.10, the observed conditions are $h0l: h + k = 4n$ and $0kl: k + l = 2n$. However, these conditions are not consistent with any of the orthorhombic space groups listed in ITC, and the current lattice can therefore not be correct. When comparing the 010 row of reflections in the patterns from the $[100]$ and $[30\bar{1}]$ zone axes, one can observe that the strong reflections in $[30\bar{1}]$ are the 003 and 006 reflections, while in $[100]$ the 003 reflections is absent and the 002 and 004 are the strong ones. Also, unexpected intensity similarities between very different types of reflections are observed (e.g. the intensities of the 400 and the $\bar{2}06$ reflections in Figure 6.10).

6.2.3 Tilt series C

Tilt series C revealed an orthorhombic lattice with lattice parameters $a = 5.51 \text{ \AA}$, $b = 7.61 \text{ \AA}$ and $c = 11.30 \text{ \AA}$. Figure 6.11 shows the SADPs of tilt series C, and the Google Sketchup model is shown in Figure 6.12. The experimental and calculated angles between the SADPs are listed in Table 6.6.

Table 6.6: Calculated and experimental angles between the zone axes in tilt series C.

Zone axes	Experimental angles	Calculated angles
[010] and [130]	13.7°	13.8°
[130] and [120]	6.2°	6.4°
[120] and [230]	6.2°	5.9°
[230] and [110]	10.2°	10.2°
[110] and [430]	8.2°	8.1°
[430] and [210]	11.2°	11.3°
[210] and [410]	15.4°	15.4°
[410] and [100]	19.8°	18.7°

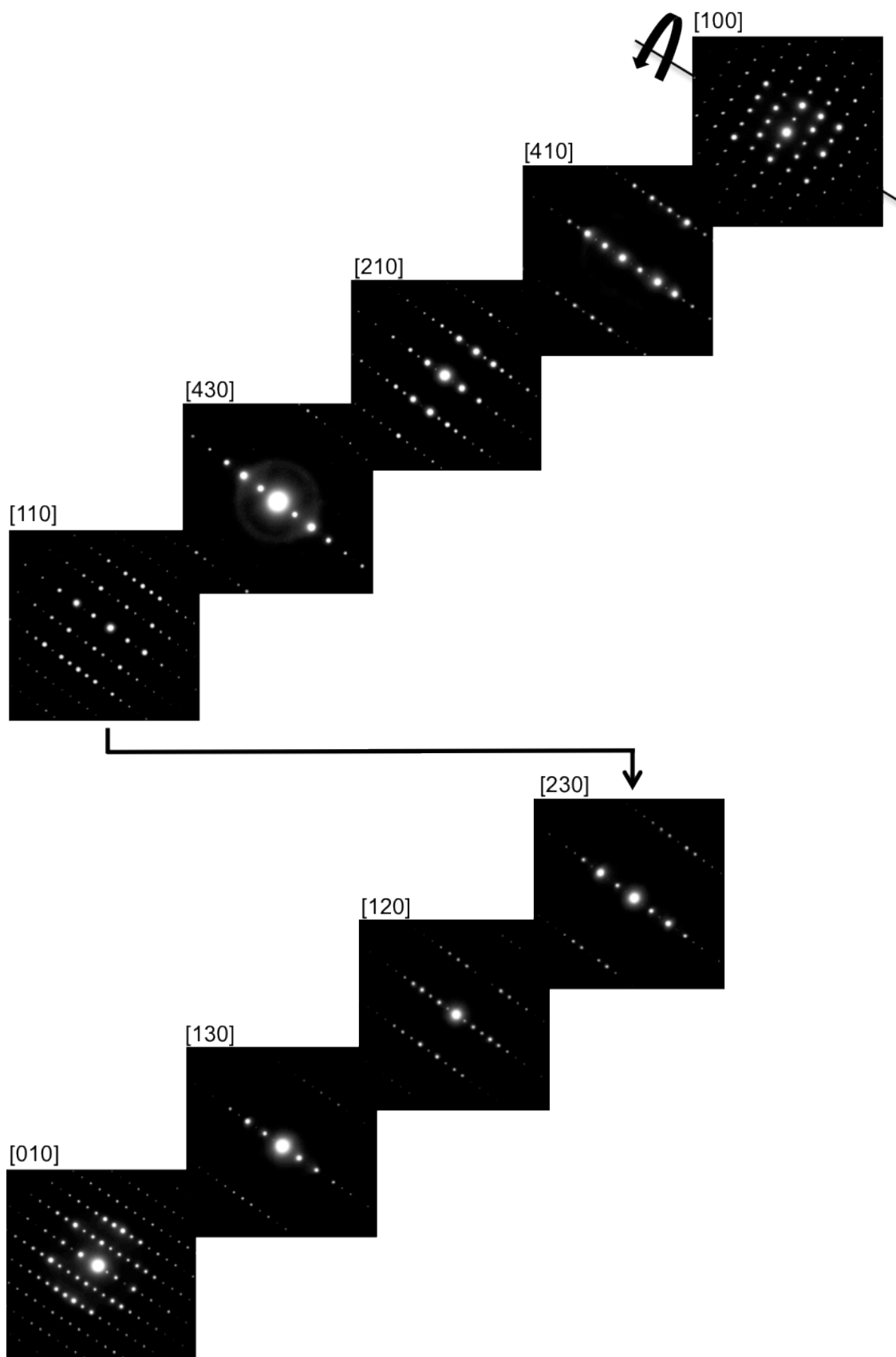


Figure 6.11: Tilt series C, revealing an orthorhombic lattice with lattice parameters $a = 5.51 \text{ \AA}$, $b = 7.61 \text{ \AA}$ and $c = 11.30 \text{ \AA}$.

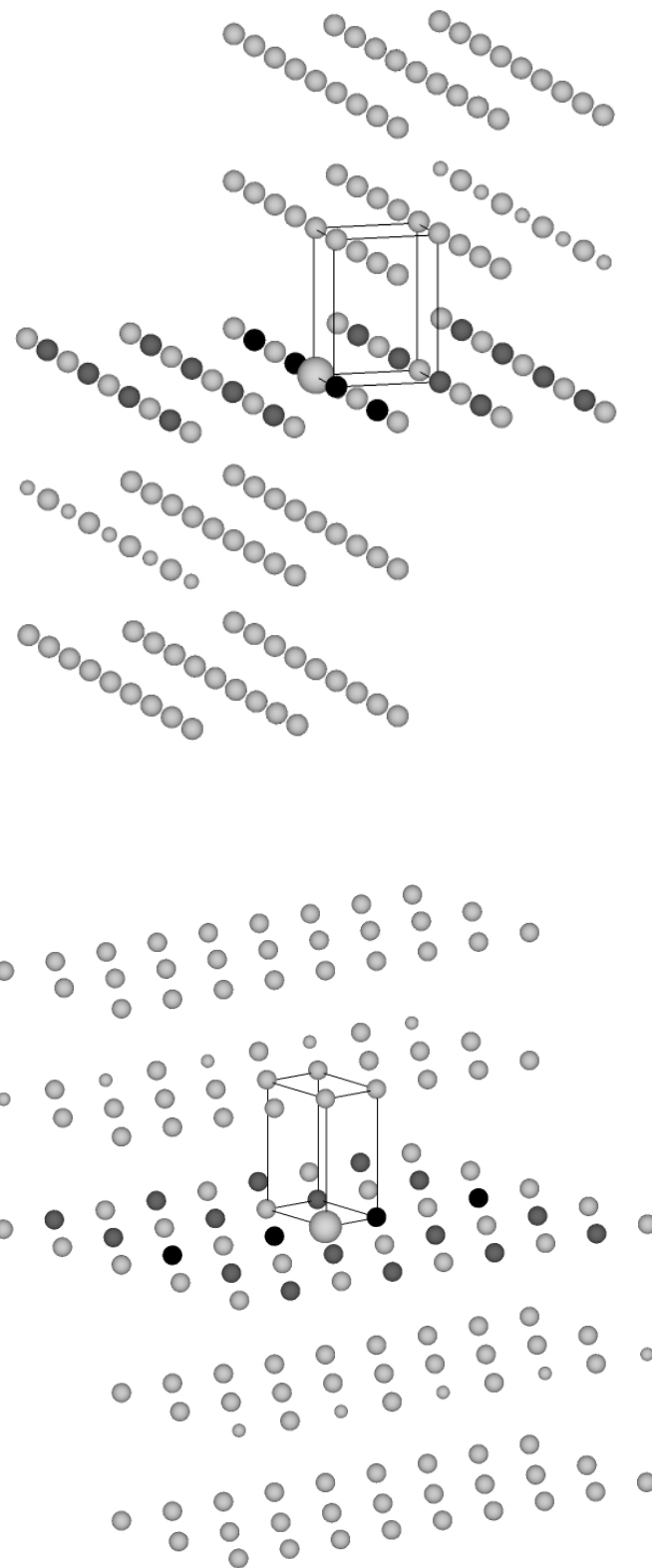


Figure 6.12: 3D models of the reciprocal lattice based on tilt series C, at slightly different angles. Kinematically forbidden diffraction spots that appeared in the tilt series are coloured black, and kinematically forbidden spots that did not appear are colored dark grey. The lines mark the edges of the reciprocal unit cell.

Figure 6.13 shows the indexed diffraction patterns from the $[010]$ and $[100]$ zone axes with common row $00l$. The $00l$ -reflections with odd values for l are extinct in $[100]$ (marked with an X in the figure), which means they are visible in $[010]$ due to dynamical scattering effects (cf. Section 4.3). The conditions for Umweganregung are satisfied in this pattern, as $\mathbf{g}_{101} + \mathbf{g}_{100} = \mathbf{g}_{001}$ (cf. Section 4.3.1). In the pattern from the $[100]$ zone axis, these conditions are not satisfied, as $0kl$ reflections with odd values for l ($011, 013, 015$ etc.) are also extinct.

The observed extinctions are consistent with the reflection conditions $00l: l = 2n$ and $0kl: l = 2n$. From these conditions, a c -glide normal to $[100]$ is present, and in addition a 2_1 screw axis parallel with $[001]$ may be present. No other extinctions were observed, and the lattice is therefore assumed to be primitive (cf. Section 3.2.3).

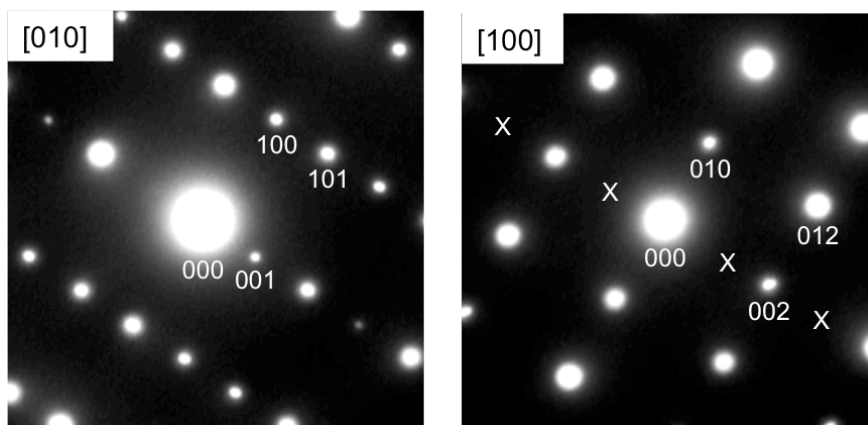


Figure 6.13: Indexed SADPs of the diffraction patterns from the $[010]$ and $[100]$ zone axes. The patterns are tilted about the $00l$ -row, and the absent reflections along this row are indicated with x in $[100]$.

The reflection conditions leave the following three possible space groups:

Pmc2₁ (no.26): Described by the non-standard setting *Pcm2₁* (cf. Section 3.2.1), the reflection conditions arise from the c -glide plane normal to $[100]$, and are also consistent with the 2_1 screw axis parallel with $[001]$.

Pma2 (no. 28): Described by the non-standard setting *Pc2m*, the reflection conditions arise from the c -glide plane normal to $[100]$.

Pmma (no. 51): Described by the non-standard setting *Pcmm*. The full symbol for the space group in this setting is $P\ 2/c\ 2/m\ 2_1/m$. The reflection conditions arise from the *c*-glide plane normal to [100], and are also consistent with the 2_1 screw axis parallel with [001].

6.3 Discussion

Although the compositional analysis suggests one Ni-Nb-O phase with Ni:Nb ratio 2-3, the electron diffraction analysis reveal three different structures. The lattice parameters for structures A, B and C are listed in Table 6.7, along with the relation among the axes within each structure.

Table 6.7: Lattice parameters from tilt series A, B and C.

Structure	<i>a</i>	<i>b</i>	<i>c</i>	Relations among axes		
A	5.04 Å	9.00 Å	14.20 Å	$(2a^2)^{1/2} \approx 1/2c$		
B	10.14 Å	14.17 Å	17.51 Å	$(2b^2)^{1/2} \approx 2a$		
C	5.51 Å	7.61 Å	11.30 Å	$c \approx 2a$	$(2a^2)^{1/2} \approx b$	$(2c^2)^{1/2} \approx 2b$

The axes of structure C does not seem to be related to the axes of the other two structures, but the axes in structure A and B are related as follows (subscripts refer to the appropriate structure):

$$a_B \approx 2a_A$$

$$c_A \approx b_B$$

$$c_B \approx 2b_A$$

In section 2.3, a diffraction pattern from preliminary electron diffraction analysis was compared to the two published structures for Ni₄Nb₂O₉, but did not match any of them. Comparing it with the diffraction patterns and *d*-values from the tilt series, it was found to match the diffraction pattern from the [100] zone axis from structure B (see Figure 6.14).

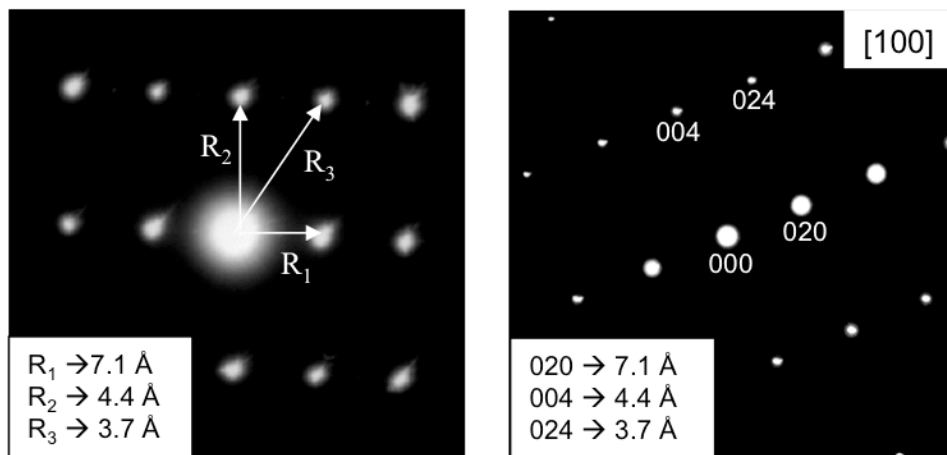


Figure 6.14: Left: Diffraction pattern from initial electron diffraction analyses. Right: Diffraction pattern from the $[100]$ zone axis of tilt series B. The d -values from the two patterns coincide.

As discussed in section 2.1, the refinement of $\text{II-Ni}_4\text{Nb}_2\text{O}_9$ (with space group $Pcan$, as reported by Wichmann et al. [cf. Section 2.2]) did not yield satisfying results, as the observed peaks did not match the refined structure. Closer examination of the XRD pattern showed that d -values extracted from the peak positions do coincide with the lattice parameters of $\text{II-Ni}_4\text{Nb}_2\text{O}_9$. With this information the refinement was given several tries, but the refined structure did not change much and could still not match the observed peaks. The d -values extracted from the XRD pattern are listed in Table 6.8 along with the lattice parameters for structures A, B, $\text{II-Ni}_4\text{Nb}_2\text{O}_9$ (reported by Wichmann et al.) and $\text{Ni}_4\text{Nb}_2\text{O}_9$ reported by Magrasó et al.

Table 6.8: Experimental lattice parameters from TEM (structures A and B) and XRD studies of the NiLN3-1300 sample, and the lattice parameters reported for $\text{Ni}_4\text{Nb}_2\text{O}_9$ by Wichmann et al. [18] and Magrasó et al. [12].

Lattice parameters	Experimental			$\text{Ni}_4\text{Nb}_2\text{O}_9$ (<i>Pcan</i>)	
	TEM Structure A	TEM Structure B	XRD peak positions	Reported by Wichmann et al.	Reported by Magrasó et al.
<i>a</i>	5.04 Å	<i>a</i> = 10.14	5.046 Å (2 x 2.523 Å)	5.055 Å	5.026 Å
<i>b</i>	9.00 Å	<i>c</i> = 17.51	8.770 Å (2 x 4.385 Å)	8.769 Å	8.758 Å
<i>c</i>	14.20 Å	<i>b</i> = 14.17	14.296 Å (4 x 3.574 Å)	14.304 Å	14.340 Å

As can be seen in the table, the lattice parameters of structure A are similar to those of II- $\text{Ni}_4\text{Nb}_2\text{O}_9$, and both structure A and B can in theory account for the peaks at positions 2.523 Å, 4.385 Å and 3.574 Å.

As mentioned in Section 2.1, there are two peaks, positioned at $d = 3.022$ Å and $d = 3.069$ Å, that cannot be accounted for by any of the refined structures (see Figure 2.5). These peaks may correspond to the 121 and 120 reflections from tilt series C, with d -values of 3.01 Å and 3.11 Å, respectively. The XRD pattern was examined to check for more peaks consistent with the structure from this tilt series, and a peak was found at position $d = 5.526$ Å that may correspond to lattice parameter $a = 5.51$ Å in structure C. More peaks were found that fit the d -values of this structure, but as the peaks are also consistent with II- $\text{Ni}_4\text{Nb}_2\text{O}_9$ and/or LaNbO_4 , they could not be used to confirm the tilt series. For many of the d -values from structure C there are little to no intensity.

Tilt series A did not reveal any systematic extinctions (cf. Section 6.2.1), but since the lattice parameters of the structure coincide with II- $\text{Ni}_4\text{Nb}_2\text{O}_9$, it was further analysed to see if the reflections violating the reflection conditions for *Pcan* could be present due to dynamic scattering of the electrons. The peaks corresponding to these reflections are absent in the XRD pattern, and as X-Ray scattering is purely kinematic this is expected if the reflection conditions for *Pcan* are valid (cf. Section 4.3). The space group *Pcan* include glide planes

which give rise to the following reflection conditions: $0kl: l = 2n$, $h0l: h = 2n$, $hk0: h + k = 2n$, $h00: h = 2n$, $0k0: k = 2n$ and $00l: l = 2n$ (cf. Section 3.2.3).

Inspection of the diffraction patterns from tilt series A shows that although some of the kinematically forbidden reflections satisfy the conditions for Umweganregung (cf. Section 4.3.1), not all of them do. Figure 6.15 shows the diffraction pattern from the $[1\bar{1}\bar{1}]$ zone axes. According to the reflection conditions of $Pcan$, the $01\bar{1}$ and 101 (and equivalent) reflections should be extinct. These sets of reflections cannot appear at the same time by dynamical scattering, as the conditions for Umweganregung will not be satisfied [34]. This excludes the space group $Pcan$ as a possible space group for structure A. The fact that one sees reflections with ED and not with XRD does not necessarily mean that the reflections appear due to dynamical effects. Electrons interact much stronger with matter, and weak reflections seen with ED can easily be overseen in an XRD spectrum. In addition, the amount of this phase may be negligible compared to the others present in the sample, not generating enough signals to produce visible peaks. Another possibility is that some of the reflections are in fact kinematically forbidden, and that the structure belongs to some other space group. However, from the data in the present project structure A is consistent with space groups $Pmm2$ and $Pmmm$ (cf. Section 6.2.1), and no further conclusions can be made at the present time.

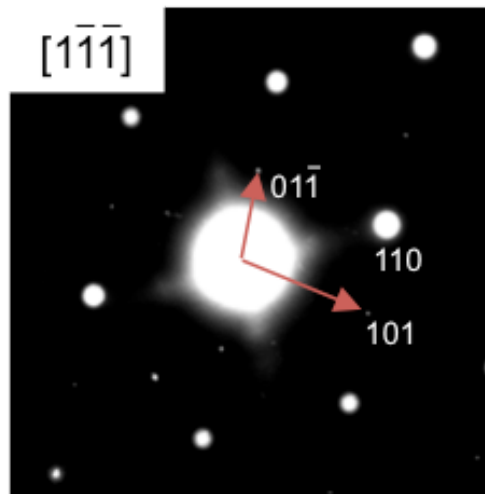


Figure 6.15: The diffraction pattern from zone axis $[1\bar{1}\bar{1}]$ from tilt series A. The red arrows represent reciprocal lattice vectors for reflections violating reflection conditions for space group $Pcan$.

As seen in section 6.2.2, the resulting lattice from tilt series B cannot be correct. This lattice has similar lattice parameters as those first determined for $\text{II-Ni}_4\text{Nb}_2\text{O}_9$ by Wichmann et al. [18]. However, they rejected this lattice in favor of the $Pcan$ structure of $\text{II-Ni}_4\text{Nb}_2\text{O}_9$ with lattice parameters $a = 5.0545 \text{ \AA}$, $b = 8.7688 \text{ \AA}$ and $c = 14.3041 \text{ \AA}$ (cf. Section 2.2), concluding that the doubling of two of the axes was due to twinning of these crystals. The twinning was not explained in detail. No twinning was observed in the images of the grains analyzed in the present study. However, the twin domains may be so small that high-resolution electron microscopy (HREM) is needed in order to observe them. The diffraction pattern from the $[0\bar{1}0]$ zone axis in Figure 6.10 can be explained as three individual crystals with primitive lattices sharing some of the same lattice points as illustrated in Figure 6.16. Tilting this reciprocal lattice 90° towards the $[100]$ projection would be consistent with the observations in this projection. However, the additional reflections along the 010 row in $[30\bar{1}]$ projection could imply a more complex structure. The time limit did not allow for further investigation.

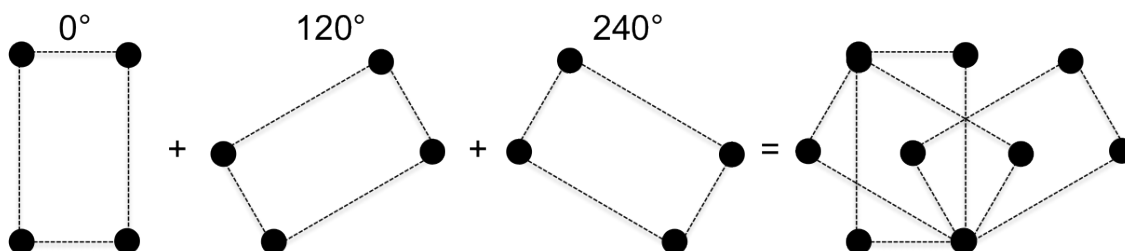


Figure 6.16: Principle of three-fold twinning of orthorhombic crystal. Projection along [001]. The short and long side of the rectangles are proportional to 5.0 Å and 8.8 Å, respectively.

As discussed in section 2.2, the only phase close to the composition determined by EDS is $\text{Ni}_4\text{Nb}_2\text{O}_9$ (according to Burdese et al. [16], see phase diagram in Figure 2.6). $\text{Ni}_4\text{Nb}_2\text{O}_9$ forms above 1300 °C, consistent with the studied phase. It is already shown by Wichmann et al. [17, 18] that $\text{Ni}_4\text{Nb}_2\text{O}_9$ may crystallize in two different structures depending on the cooling rate of the reaction products (cf. Section 2.2). If other experimental conditions also affect the type of crystallization, this may explain the different structures as Wichmann et al. used different precursors for the synthesis than Magrasó et al. Regarding the variations in the Ni:Nb ratio, this may be explained by different compositions of the different structures, which means other phases than $\text{Ni}_4\text{Nb}_2\text{O}_9$ form in the nearby region of this phase. Another possibility is that the structure(s) are flexible and can accommodate different ratios of Ni and Nb. Investigations of NiNb_2O_6 by Burdese et al. conclude that variations of lattice constants with composition are extremely small [16], and this may also be the case of $\text{Ni}_4\text{Nb}_2\text{O}_9$. In order to make any conclusions further examinations of the sample are necessary.

7 Conclusions

- Compositional analysis suggests four phases present in the sample NiLN3-1300: NiO, LaNbO₄, LaNb₃O₉ and a Ni-Nb-O phase with Ni:Nb ratio of 2-3.
- Electron diffraction analysis confirm three different structures, all with compositions Ni-Nb-O and Ni:Nb ratio of 2-3.
- Structure A is orthorhombic with lattice parameters $a = 5.04 \text{ \AA}$, $b = 9.00 \text{ \AA}$ and $c = 14.20 \text{ \AA}$. There are no observed extinctions, and the structure is thus consistent with space groups $Pmm2$ and $Pmmm$. Some of the reflections are very weak and may be visible due to dynamical scattering, and the structure may thus have higher symmetry than the suggested space groups. $Pcan$ is excluded as possible space group.
- Structure B was identified as orthorhombic with lattice parameters $a = 10.14 \text{ \AA}$, $b = 14.17 \text{ \AA}$ and $c = 17.51 \text{ \AA}$ according to tilt series B. However, the reflection conditions of this structure are not consistent with any of the orthorhombic space groups in ITC. Twinning of primitive crystals with lattice parameters as found in structure A may be part of the explanation.
- Structure B seems to be the most abundant of structures A, B and C, as diffraction patterns from several grains match this structure. Many of the peaks in the XRD pattern can be indexed according to this structure, but further investigation is necessary to make any further conclusions.
- Structure C is orthorhombic with lattice parameters $a = 5.51 \text{ \AA}$, $b = 7.61 \text{ \AA}$ and $c = 11.30 \text{ \AA}$. The observed extinctions are consistent with space groups $Pcm2_1$, $Pc2m$ and $Pcmm$.

8 Suggestion for further work

- Determination of the point group for each structure by convergent beam electron diffraction (CBED). Also systematic investigation of the sample to determine whether or not it contains more structures than the identified ones.
- Accurate determination of compositions in the sample by Electron Energy Loss Spectroscopy (EELS) and Electron Probe Micro Analysis (EPMA)
- Investigate atomic arrangement and look for twinned crystals by HREM.
- Structure refinement
- Synthesis of $\text{Ni}_4\text{Nb}_2\text{O}_9$ by the same synthesis route as Wichmann et al., determine the resulting structure(s) by the above mentioned methods and compare it with the sample in the present study.

9 References

- [1] IPCC, 2011: The IPCC Special Report on Renewable Energy Sources and Climate Change Mitigation (SRREN), (Edenhofer, O., Pichs-Madruga, R., Sokona, Y., Seyboth, K., Matschoss, P., Kadner, S., Zwickel, T., Eickemeier, P., Hansen, G., Schlömer, S., and von Stechow, C., eds.), Cambridge University Press, 2011.
- [2] Stambouli, A.B. and Djerroud, S., *Revue des Energies Renouvelables* (2011), **14**, 267.
- [3] Stambouli, A.B. and Traversa, E., *Renewable and Sustainable Energy Reviews* (2002), **6**, 433.
- [4] Magrasó, A., Fontaine, M.L., Larring, Y., Bredesen, R., Syvertsen, G.E., Lein, H.L., Grande, T., Huse, M., Strandbakke, R., Haugrud, R., and Norby, T., *Fuel Cells* (2011), **11**, 17.
- [5] Kreuer, K.D., *Annu. Rev. Mater. Res.* (2003), **33**, 333.
- [6] Haugrud, R. and Norby, T., *Solid State Ionics* (2006), **177**, 1129.
- [7] Haugrud, R. and Norby, T., *Nature Materials* (2006), **5**, 193.
- [8] Magraso, A., Haugrud, R., and Norby, T., *J. Am. Ceram. Soc.* (2010), **93**, 2650.
- [9] Tolchard, J.R., Lein, H.L., and Grande, T., *Journal of the European Ceramic Society* (2009), **29**, 2823.
- [10] Sunding, M.F., Kepaptsoglou, D.M., Diplas, S., Norby, T., and Gunnæs, A.E., *Surface and Interface Analysis* (2010), **42**, 568.
- [11] Syvertsen, G.E. et al., in press.
- [12] Magrasó, A. and Fontaine, M.-L., *Journal of Power Sources* (2011).
- [13] Wood, J.R., The University of Oslo, Oslo, 2007.
- [14] Bertaut, E.F., Corliss, L., and Forrat, F., *Comptes Rendus de l'Academie des Sciences* (1960), **251**, 1733.
- [15] Bertaut, E.F., Corliss, L., Forrat, F., Aleonard, R., and Pauthenet, R., *Journal of Physical and Chemical Solids* (1961), **21**, 234.
- [16] Burdese, A., Borlera, M.L., and Rolando, P., *Atti Accad. Sci. Torino: I Classe Sci. Fis. Mater. Nat.* (1964), **99**, 565.

- [17] Wichmann, R. and Müller-Buschbaum, H., *Zeitschrift für anorganische und allgemeine Chemie* (1985), **525**, 135.
- [18] Wichmann, R. and Müller-Buschbaum, H., *Zeitschrift für anorganische und allgemeine Chemie* (1986), **539**, 203.
- [19] FindIt, version 1.8.1, FIZ Karlsruhe, Inorganic Crystal Structure Database (ICSD).
- [20] Zou, J.M. and Mabon, J.C., Web-based Electron Microscopy Application Software: Web-EMAPS, *Microsc Microanal* 10(Suppl 2), version (2004), <http://emaps.mrl.uiuc.edu/>.
- [21] *International Tables for Crystallography*, (2006) Vol. A, Space-group symmetry
- [22] Docherty, R. and Roberts, K.J., *Computer Physics Communications* (1988), **51**, 423.
- [23] Double slit diffraction, <http://www.thestargarden.co.uk/images/163.Double_slit_waves.png> (15.11.2011).
- [24] Williams, D.B. and Carter, C.B., *Transmission Electron Microscopy*, Springer, New York, (2009)
- [25] Gjønnes, J. and Moodie, A.F., *Acta Crystallographica* (1965), **19**, 65.
- [26] The Barrett Research Group, Image of TEM, <<http://barrett-group.mcgill.ca/teaching/nanotechnology/nano02.htm>> (02.08.11).
- [27] Kelly, P.M., Wauchope, C.J., and Zhang, X., *Microscopy Research And Technique* (1994), **28**, 448.
- [28] Parrish, W., *Acta Crystallographica* (1960), **13**, 838.
- [29] @Last Software, *Google Sketchup*, version 8.0 (2010), 3D computer graphics, <http://www.sketchup.google.com>.
- [30] Nelson, P.S.A., <<http://www.tulane.edu/~sanelson/eens211/x-ray.htm>> (28.10.2011).
- [31] Wittke, J.H., *Electron interaction volume in the SEM*, 2008, <<http://www4.nau.edu/microanalysis/Microprobe-SEM/Signals.html>> (07.12.2011).
- [32] Personal communication with Magrasó, A., (2010-2011), e-mail: a.m.sola@smn.uio.no.
- [33] Personal communication with Kepaptsoglou, D.M., (2010-2011), e-mail: dmkepap@gmail.com.

[34] Personal communication with Gunnæs, A.E., (2010-2011), e-mail: a.e.gunnas@fys.uio.no.

Appendix A: Structural data

A.1 Cc2e (no. 42)

International Tables for Crystallography (2006). Vol. A, Space group 42, pp. 252–253.

$Fmm2$

C_{2v}^{18}

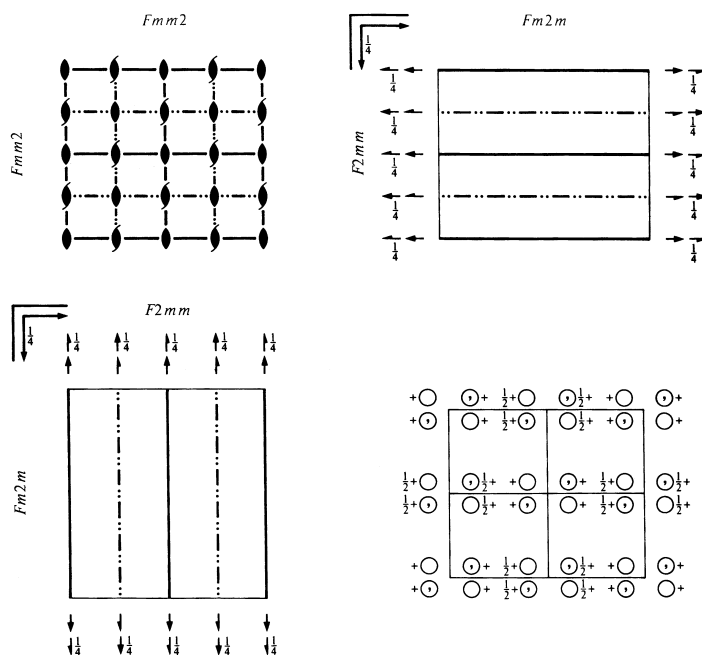
$mm2$

Orthorhombic

No. 42

$Fmm2$

Patterson symmetry $Fmmm$



Origin on $mm2$

Asymmetric unit $0 \leq x \leq \frac{1}{4}$; $0 \leq y \leq \frac{1}{2}$; $0 \leq z \leq 1$

Symmetry operations

For $(0,0,0)+$ set

(1) 1 (2) $2\ 0,0,z$ (3) $m\ x,0,z$ (4) $m\ 0,y,z$

For $(0,\frac{1}{2},\frac{1}{2})+$ set

(1) $i(0,\frac{1}{2},\frac{1}{2})$ (2) $2(0,0,\frac{1}{2})\ 0,\frac{1}{2},z$ (3) $c\ x,\frac{1}{2},z$ (4) $n(0,\frac{1}{2},\frac{1}{2})\ 0,y,z$

For $(\frac{1}{2},0,\frac{1}{2})+$ set

(1) $i(\frac{1}{2},0,\frac{1}{2})$ (2) $2(0,0,\frac{1}{2})\ \frac{1}{2},0,z$ (3) $n(\frac{1}{2},0,\frac{1}{2})\ x,0,z$ (4) $c\ \frac{1}{2},y,z$

For $(\frac{1}{2},\frac{1}{2},0)+$ set

(1) $i(\frac{1}{2},\frac{1}{2},0)$ (2) $2\ \frac{1}{2},\frac{1}{2},z$ (3) $a\ x,\frac{1}{2},z$ (4) $b\ \frac{1}{2},y,z$

Generators selected (1); $t(1,0,0)$; $t(0,1,0)$; $t(0,0,1)$; $t(0, \frac{1}{2}, \frac{1}{2})$; $t(\frac{1}{2}, 0, \frac{1}{2})$; (2); (3)

Positions

Multiplicity, Wyckoff letter, Site symmetry (0,0,0)+ $(0, \frac{1}{2}, \frac{1}{2})+$ $(\frac{1}{2}, 0, \frac{1}{2})+$ $(\frac{1}{2}, \frac{1}{2}, 0)+$

16 *e* 1 (1) x, y, z (2) \bar{x}, \bar{y}, z (3) x, \bar{y}, z (4) \bar{x}, y, z

Reflection conditions

General:

 $hkl : h+k, h+l, k+l = 2n$ $0kl : k, l = 2n$ $h0l : h, l = 2n$ $hk0 : h, k = 2n$ $h00 : h = 2n$ $0k0 : k = 2n$ $00l : l = 2n$

Special: as above, plus

8 *d* .*m*. $x, 0, z$ $\bar{x}, 0, z$

no extra conditions

8 *c* *m*. . $0, y, z$ $0, \bar{y}, z$

no extra conditions

8 *b* . . 2 $\frac{1}{2}, \frac{1}{2}, z$ $\frac{1}{2}, \frac{1}{2}, z$

 $hkl : h = 2n$

4 *a* *m* *m* 2 $0, 0, z$

no extra conditions

Symmetry of special projectionsAlong [001] *p2mm* $\mathbf{a}' = \frac{1}{2}\mathbf{a}$ $\mathbf{b}' = \frac{1}{2}\mathbf{b}$

Origin at 0, 0, z

Along [100] *p1m1* $\mathbf{a}' = \frac{1}{2}\mathbf{b}$ $\mathbf{b}' = \frac{1}{2}\mathbf{c}$ Origin at $x, 0, 0$ Along [010] *p11m* $\mathbf{a}' = \frac{1}{2}\mathbf{c}$ $\mathbf{b}' = \frac{1}{2}\mathbf{a}$

Origin at 0, y, 0

Maximal non-isomorphic subgroups

I [2] *F1m1* (*Cm*, 8) (1; 3)+
 [2] *Fm11* (*Cm*, 8) (1; 4)+
 [2] *F112* (*C2*, 5) (1; 2)+

IIa [2] *Aea2* (41) 1; 2; (1; 2) + $(0, \frac{1}{2}, \frac{1}{2})$; (3; 4) + $(\frac{1}{2}, 0, \frac{1}{2})$; (3; 4) + $(\frac{1}{2}, \frac{1}{2}, 0)$
 [2] *Bbe2* (*Aea2*, 41) 1; 2; (1; 2) + $(\frac{1}{2}, 0, \frac{1}{2})$; (3; 4) + $(0, \frac{1}{2}, \frac{1}{2})$; (3; 4) + $(\frac{1}{2}, \frac{1}{2}, 0)$
 [2] *Ama2* (40) 1; 4; (1; 4) + $(0, \frac{1}{2}, \frac{1}{2})$; (2; 3) + $(\frac{1}{2}, 0, \frac{1}{2})$; (2; 3) + $(\frac{1}{2}, \frac{1}{2}, 0)$
 [2] *Bbm2* (*Ama2*, 40) 1; 3; (1; 3) + $(\frac{1}{2}, 0, \frac{1}{2})$; (2; 4) + $(0, \frac{1}{2}, \frac{1}{2})$; (2; 4) + $(\frac{1}{2}, \frac{1}{2}, 0)$
 [2] *Bme2* (*Aem2*, 39) 1; 4; (1; 4) + $(\frac{1}{2}, 0, \frac{1}{2})$; (2; 3) + $(0, \frac{1}{2}, \frac{1}{2})$; (2; 3) + $(\frac{1}{2}, \frac{1}{2}, 0)$
 [2] *Aem2* (39) 1; 3; (1; 3) + $(0, \frac{1}{2}, \frac{1}{2})$; (2; 4) + $(\frac{1}{2}, 0, \frac{1}{2})$; (2; 4) + $(\frac{1}{2}, \frac{1}{2}, 0)$
 [2] *Amm2* (38) 1; 2; 3; 4; (1; 2; 3; 4) + $(0, \frac{1}{2}, \frac{1}{2})$
 [2] *Bmm2* (*Amm2*, 38) 1; 2; 3; 4; (1; 2; 3; 4) + $(\frac{1}{2}, 0, \frac{1}{2})$
 [2] *Ccc2* (37) 1; 2; (1; 2) + $(\frac{1}{2}, \frac{1}{2}, 0)$; (3; 4) + $(0, \frac{1}{2}, \frac{1}{2})$; (3; 4) + $(\frac{1}{2}, 0, \frac{1}{2})$
 [2] *Ccm2*, (*Cmc2*, 36) 1; 3; (1; 3) + $(\frac{1}{2}, \frac{1}{2}, 0)$; (2; 4) + $(0, \frac{1}{2}, \frac{1}{2})$; (2; 4) + $(\frac{1}{2}, 0, \frac{1}{2})$
 [2] *Cmc2*, (36) 1; 4; (1; 4) + $(\frac{1}{2}, \frac{1}{2}, 0)$; (2; 3) + $(0, \frac{1}{2}, \frac{1}{2})$; (2; 3) + $(\frac{1}{2}, 0, \frac{1}{2})$
 [2] *Cmm2* (35) 1; 2; 3; 4; (1; 2; 3; 4) + $(\frac{1}{2}, \frac{1}{2}, 0)$

IIb none**Maximal isomorphic subgroups of lowest index****IIc** [3] *Fmm2* ($\mathbf{a}' = 3\mathbf{a}$ or $\mathbf{b}' = 3\mathbf{b}$) (42); [3] *Fmm2* ($\mathbf{c}' = 3\mathbf{c}$) (42)**Minimal non-isomorphic supergroups****I** [2] *Fmmm* (69); [2] *I4mm* (107); [2] *I4cm* (108); [2] *I42m* (121)**II** [2] *Pmm2* ($\mathbf{a}' = \frac{1}{2}\mathbf{a}, \mathbf{b}' = \frac{1}{2}\mathbf{b}, \mathbf{c}' = \frac{1}{2}\mathbf{c}$) (25)

A.2 *Fdd2* (no. 43)

International Tables for Crystallography (2006). Vol. A, Space group 43, pp. 254–255.

Fdd2

C_{2v}^{19}

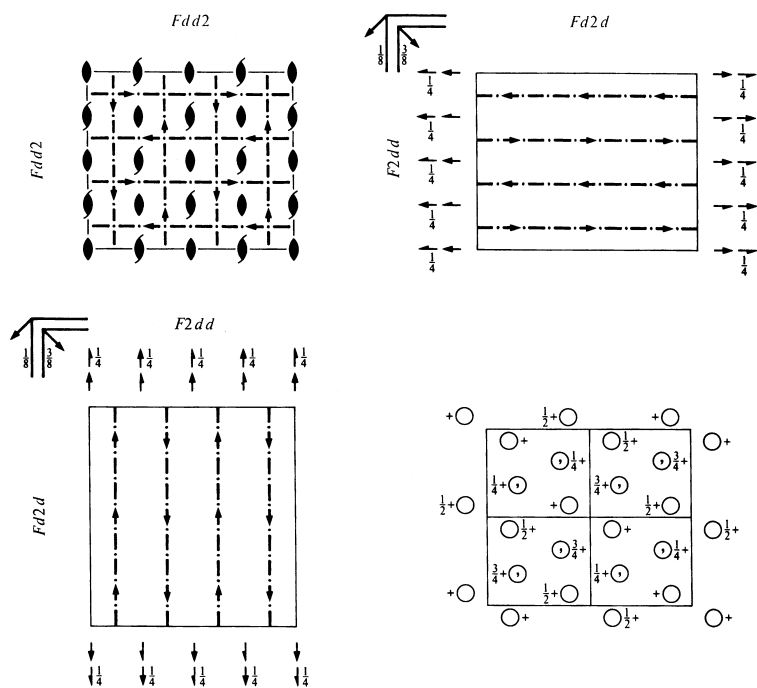
mm2

Orthorhombic

No. 43

Fdd2

Patterson symmetry *Fmmm*



Origin on 112

Asymmetric unit $0 \leq x \leq \frac{1}{4}; 0 \leq y \leq \frac{1}{4}; 0 \leq z \leq 1$

Symmetry operations

For $(0,0,0)+$ set

(1) 1 (2) $2\ 0,0,z$ (3) $d(\frac{1}{4},0,\frac{1}{4})\ x,\frac{1}{8},z$ (4) $d(0,\frac{1}{4},\frac{1}{4})\ \frac{1}{8},y,z$

For $(0,\frac{1}{2},\frac{1}{2})+$ set

(1) $t(0,\frac{1}{2},\frac{1}{2})$ (2) $2(0,0,\frac{1}{2})\ 0,\frac{1}{4},z$ (3) $d(\frac{1}{4},0,\frac{3}{4})\ x,\frac{3}{8},z$ (4) $d(0,\frac{3}{4},\frac{3}{4})\ \frac{1}{8},y,z$

For $(\frac{1}{2},0,\frac{1}{2})+$ set

(1) $t(\frac{1}{2},0,\frac{1}{2})$ (2) $2(0,0,\frac{1}{2})\ \frac{1}{4},0,z$ (3) $d(\frac{3}{4},0,\frac{3}{4})\ x,\frac{1}{8},z$ (4) $d(0,\frac{1}{4},\frac{3}{4})\ \frac{3}{8},y,z$

For $(\frac{1}{2},\frac{1}{2},0)+$ set

(1) $t(\frac{1}{2},\frac{1}{2},0)$ (2) $2\ \frac{1}{4},\frac{1}{4},z$ (3) $d(\frac{3}{4},0,\frac{1}{4})\ x,\frac{3}{8},z$ (4) $d(0,\frac{3}{4},\frac{1}{4})\ \frac{3}{8},y,z$

Generators selected (1); $t(1,0,0)$; $t(0,1,0)$; $t(0,0,1)$; $t(0, \frac{1}{2}, \frac{1}{2})$; $t(\frac{1}{2}, 0, \frac{1}{2})$; (2); (3)

Positions

Multiplicity, Wyckoff letter, Site symmetry	Coordinates				Reflection conditions
	$(0,0,0)+$	$(0, \frac{1}{2}, \frac{1}{2})+$	$(\frac{1}{2}, 0, \frac{1}{2})+$	$(\frac{1}{2}, \frac{1}{2}, 0)+$	General:
16 <i>b</i> 1	(1) x, y, z	(2) \bar{x}, \bar{y}, z	(3) $x + \frac{1}{2}, \bar{y} + \frac{1}{2}, z + \frac{1}{2}$	(4) $\bar{x} + \frac{1}{2}, y + \frac{1}{2}, z + \frac{1}{2}$	$hkl : h+k, h+l, k+l = 2n$ $0kl : k+l = 4n, k, l = 2n$ $h0l : h+l = 4n, h, l = 2n$ $hk0 : h, k = 2n$ $h00 : h = 4n$ $0k0 : k = 4n$ $00l : l = 4n$
8 <i>a</i> . . 2	0, 0, z	$\frac{1}{4}, \frac{1}{4}, z + \frac{1}{4}$			Special: as above, plus $hkl : h = 2n + 1$ or $h+k+l = 4n$

Symmetry of special projections

Along [001] *p2gg*
 $\mathbf{a}' = \frac{1}{2}\mathbf{a}$ $\mathbf{b}' = \frac{1}{2}\mathbf{b}$
 Origin at 0, 0, z

Along [100] *c1m1*
 $\mathbf{a}' = \frac{1}{2}\mathbf{b}$ $\mathbf{b}' = \frac{1}{2}\mathbf{c}$
 Origin at $x, 0, 0$

Along [010] *c11m*
 $\mathbf{a}' = \frac{1}{2}\mathbf{c}$ $\mathbf{b}' = \frac{1}{2}\mathbf{a}$
 Origin at 0, $y, 0$

Maximal non-isomorphic subgroups

I [2] *F1d1* (*Cc*, 9) (1; 3)+
 [2] *Fd11* (*Cc*, 9) (1; 4)+
 [2] *F112* (*C2*, 5) (1; 2)+

IIa none

IIb none

Maximal isomorphic subgroups of lowest index

IIc [3] *Fdd2* ($\mathbf{a}' = 3\mathbf{a}$ or $\mathbf{b}' = 3\mathbf{b}$) (43); [3] *Fdd2* ($\mathbf{c}' = 3\mathbf{c}$) (43)

Minimal non-isomorphic supergroups

I [2] *Fddd* (70); [2] *I4₁md* (109); [2] *I4₁cd* (110); [2] *I4₂d* (122)

II [2] *Pnn2* ($\mathbf{a}' = \frac{1}{2}\mathbf{a}, \mathbf{b}' = \frac{1}{2}\mathbf{b}, \mathbf{c}' = \frac{1}{2}\mathbf{c}$) (34)

A.3 *Pbcn* (no. 60)

International Tables for Crystallography (2006). Vol. A, Space group 60, pp. 294–295.

Pbcn

D_{2h}^{14}

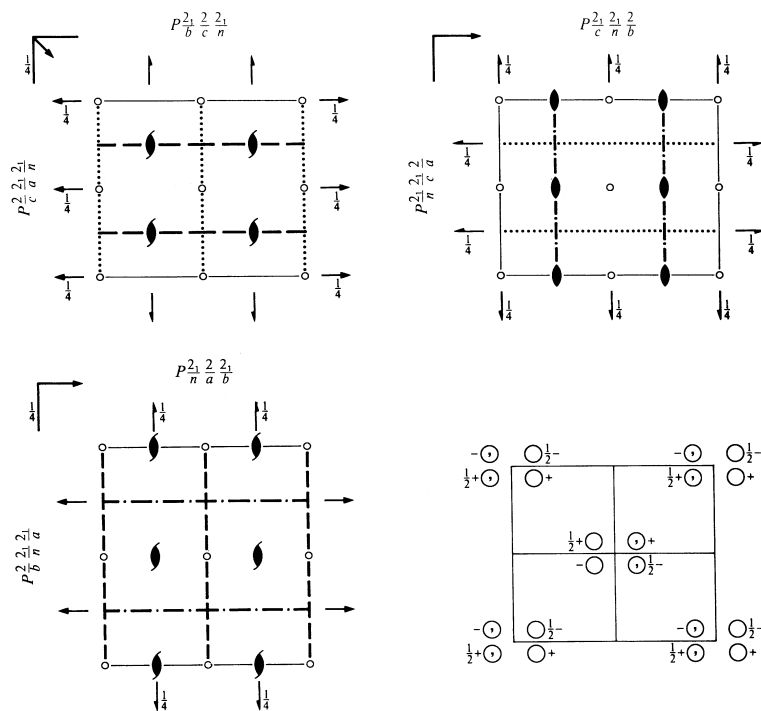
mmm

Orthorhombic

No. 60

$P 2_1/b 2/c 2_1/n$

Patterson symmetry *Pmmm*



Origin at $\bar{1}$ on $1c1$

Asymmetric unit $0 \leq x \leq \frac{1}{2}; 0 \leq y \leq \frac{1}{2}; 0 \leq z \leq \frac{1}{2}$

Symmetry operations

- | | | | |
|-------------------------|--|---------------------------|--|
| (1) 1 | (2) $2(0, 0, \frac{1}{2})$ $\frac{1}{2}, \frac{1}{2}, z$ | (3) $2 0, y, \frac{1}{4}$ | (4) $2(\frac{1}{2}, 0, 0)$ $x, \frac{1}{2}, 0$ |
| (5) $\bar{1}$ $0, 0, 0$ | (6) $n(\frac{1}{2}, \frac{1}{2}, 0)$ $x, y, \frac{1}{2}$ | (7) $c x, 0, z$ | (8) $b \frac{1}{2}, y, z$ |

Generators selected (1); $t(1,0,0)$; $t(0,1,0)$; $t(0,0,1)$; (2); (3); (5)

Positions

Multiplicity,
Wyckoff letter,
Site symmetry

Coordinates

Reflection conditions

		Coordinates				Reflection conditions
8	<i>d</i> 1	(1) x, y, z	(2) $\bar{x} + \frac{1}{2}, \bar{y} + \frac{1}{2}, z + \frac{1}{2}$	(3) $\bar{x}, y, \bar{z} + \frac{1}{2}$	(4) $x + \frac{1}{2}, \bar{y} + \frac{1}{2}, \bar{z}$	General: $0kl : k = 2n$ $h0l : l = 2n$ $hk0 : h + k = 2n$ $h00 : h = 2n$ $0k0 : k = 2n$ $00l : l = 2n$
		(5) $\bar{x}, \bar{y}, \bar{z}$	(6) $x + \frac{1}{2}, y + \frac{1}{2}, \bar{z} + \frac{1}{2}$	(7) $x, \bar{y}, z + \frac{1}{2}$	(8) $\bar{x} + \frac{1}{2}, y + \frac{1}{2}, z$	
4	<i>c</i> .2.	$0, y, \frac{1}{4}$	$\frac{1}{2}, \bar{y} + \frac{1}{2}, \frac{3}{4}$	$0, \bar{y}, \frac{3}{4}$	$\frac{1}{2}, y + \frac{1}{2}, \frac{1}{4}$	$hkl : h + k = 2n$
4	<i>b</i> $\bar{1}$	$0, \frac{1}{2}, 0$	$\frac{1}{2}, 0, \frac{1}{2}$	$0, \frac{1}{2}, \frac{1}{2}$	$\frac{1}{2}, 0, 0$	$hkl : h + k, l = 2n$
4	<i>a</i> $\bar{1}$	$0, 0, 0$	$\frac{1}{2}, \frac{1}{2}, \frac{1}{2}$	$0, 0, \frac{1}{2}$	$\frac{1}{2}, \frac{1}{2}, 0$	$hkl : h + k, l = 2n$

Symmetry of special projectionsAlong [001] *c2mm* $\mathbf{a}' = \mathbf{a}$ $\mathbf{b}' = \mathbf{b}$ Origin at $0, 0, z$ Along [100] *p2gm* $\mathbf{a}' = \frac{1}{2}\mathbf{b}$ $\mathbf{b}' = \mathbf{c}$ Origin at $x, 0, 0$ Along [010] *p2gm* $\mathbf{a}' = \frac{1}{2}\mathbf{c}$ $\mathbf{b}' = \mathbf{a}$ Origin at $0, y, 0$ **Maximal non-isomorphic subgroups**

I	[2] $P2_1cn$ ($Pna2_1, 33$)	1; 4; 6; 7
	[2] $Pb2n$ ($Pnc2, 30$)	1; 3; 6; 8
	[2] $Pbc2_1$ ($Pca2_1, 29$)	1; 2; 7; 8
	[2] $P2_12_1$ ($P2_12_1, 18$)	1; 2; 3; 4
	[2] $P112_1/n$ ($P2_1/c, 14$)	1; 2; 5; 6
	[2] $P2_1/b11$ ($P2_1/c, 14$)	1; 4; 5; 8
	[2] $P12/c1$ ($P2/c, 13$)	1; 3; 5; 7

IIa none**IIb** none**Maximal isomorphic subgroups of lowest index****IIc** [3] $Pbcn$ ($\mathbf{a}' = 3\mathbf{a}$) (60); [3] $Pbcn$ ($\mathbf{b}' = 3\mathbf{b}$) (60); [3] $Pbcn$ ($\mathbf{c}' = 3\mathbf{c}$) (60)**Minimal non-isomorphic supergroups****I** none

II [2] $Cmcm$ (63); [2] $Aema$ ($Cmce, 64$); [2] $Bbeb$ ($Ccce, 68$); [2] $Ibam$ (72); [2] $Pbmn$ ($\mathbf{c}' = \frac{1}{2}\mathbf{c}$) ($Pmna, 53$);
 [2] $Pbcb$ ($\mathbf{a}' = \frac{1}{2}\mathbf{a}$) ($Pcca, 54$); [2] $Pmca$ ($\mathbf{b}' = \frac{1}{2}\mathbf{b}$) ($Pbcm, 57$)

A.4 *Cmce* (no. 64)

International Tables for Crystallography (2006). Vol. A, Space group 64, pp. 302–303.

Cmce

D_{2h}^{18}

mmm

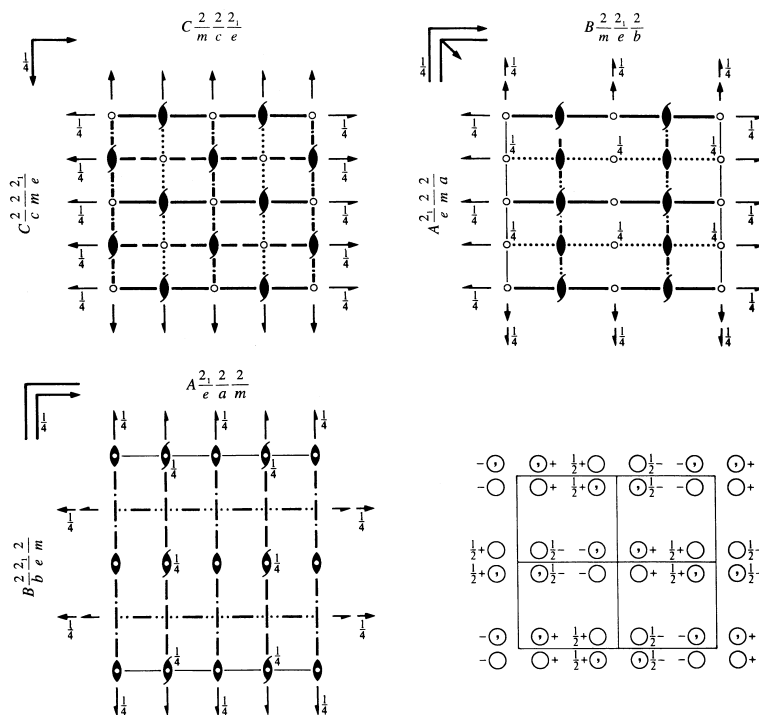
Orthorhombic

No. 64

$C 2/m 2/c 2_1/e$

Patterson symmetry *Cmmm*

Former space-group symbol *Cmca*; cf. Chapter 1.3



Origin at centre ($2/m$) at $2/mn1$

Asymmetric unit $0 \leq x \leq \frac{1}{2}$; $0 \leq y \leq \frac{1}{2}$; $0 \leq z \leq \frac{1}{2}$

Symmetry operations

For $(0, 0, 0)+$ set

- | | | | |
|-------------------------|--|--|-------------------|
| (1) 1 | (2) $2(0, 0, \frac{1}{2})$ $0, \frac{1}{2}, z$ | (3) $2(0, \frac{1}{2}, 0)$ $0, y, \frac{1}{2}$ | (4) 2 $x, 0, 0$ |
| (5) $\bar{1}$ $0, 0, 0$ | (6) b $x, y, \frac{1}{2}$ | (7) c $x, \frac{1}{2}, z$ | (8) m $0, y, z$ |

For $(\frac{1}{2}, \frac{1}{2}, 0)+$ set

- | | | | |
|---|--|--|--|
| (1) $i(\frac{1}{2}, \frac{1}{2}, 0)$ | (2) $2(0, 0, \frac{1}{2})$ $\frac{1}{2}, 0, z$ | (3) 2 $\frac{1}{2}, y, \frac{1}{2}$ | (4) $2(\frac{1}{2}, 0, 0)$ $x, \frac{1}{2}, 0$ |
| (5) $\bar{1}$ $\frac{1}{2}, \frac{1}{2}, 0$ | (6) a $x, y, \frac{1}{2}$ | (7) $n(\frac{1}{2}, 0, \frac{1}{2})$ $x, 0, z$ | (8) b $\frac{1}{2}, y, z$ |

Generators selected (1); $t(1,0,0)$; $t(0,1,0)$; $t(0,0,1)$; $t(\frac{1}{2}, \frac{1}{2}, 0)$; (2); (3); (5)

Positions

Multiplicity, Wyckoff letter, Site symmetry	Coordinates	Reflection conditions
	(0,0,0)+ $(\frac{1}{2}, \frac{1}{2}, 0)$ +	General:
16 g 1	(1) x, y, z (5) $\bar{x}, \bar{y}, \bar{z}$	$hkl : h+k=2n$ $0kl : k=2n$ $h0l : h, l=2n$ $hk0 : h, k=2n$ $h00 : h=2n$ $0k0 : k=2n$ $00l : l=2n$
	(2) $\bar{x}, \bar{y} + \frac{1}{2}, z + \frac{1}{2}$ (6) $x, y + \frac{1}{2}, \bar{z} + \frac{1}{2}$	Special: as above, plus
	(3) $\bar{x}, y + \frac{1}{2}, \bar{z} + \frac{1}{2}$ (7) $x, \bar{y} + \frac{1}{2}, z + \frac{1}{2}$	no extra conditions
	(4) x, \bar{y}, \bar{z} (8) \bar{x}, y, z	$hkl : h=2n$
8 f m..	0, y, z	$hkl : k+l=2n$
	$0, \bar{y} + \frac{1}{2}, z + \frac{1}{2}$	$hkl : k, l=2n$
	$0, y + \frac{1}{2}, \bar{z} + \frac{1}{2}$	$hkl : k+l=2n$
	$0, \bar{y}, \bar{z}$	$hkl : k+l=2n$
8 e .2.	$\frac{1}{2}, y, \frac{1}{2}$	
	$\frac{1}{2}, \bar{y} + \frac{1}{2}, \frac{1}{2}$	
	$\frac{1}{2}, y, \frac{1}{2}$	
	$\frac{1}{2}, \bar{y} + \frac{1}{2}, \frac{1}{2}$	
8 d 2..	x, 0, 0	
	$\bar{x}, \frac{1}{2}, \frac{1}{2}$	
	$\bar{x}, 0, 0$	
	$x, \frac{1}{2}, \frac{1}{2}$	
8 c $\bar{1}$	$\frac{1}{2}, \frac{1}{2}, 0$	
	$\frac{1}{2}, \frac{1}{2}, \frac{1}{2}$	
	$\frac{1}{2}, \frac{1}{2}, 0$	
	$\frac{1}{2}, \frac{1}{2}, \frac{1}{2}$	
4 b 2/m..	$\frac{1}{2}, 0, 0$	
	$\frac{1}{2}, \frac{1}{2}, \frac{1}{2}$	
4 a 2/m..	0, 0, 0	
	$0, \frac{1}{2}, \frac{1}{2}$	

Symmetry of special projections

Along [001] $p2mm$ $\mathbf{a}' = \frac{1}{2}\mathbf{a}$ $\mathbf{b}' = \frac{1}{2}\mathbf{b}$ Origin at 0, 0, z	Along [100] $p2gm$ $\mathbf{a}' = \frac{1}{2}\mathbf{b}$ $\mathbf{b}' = \mathbf{c}$ Origin at x, 0, 0	Along [010] $p2mm$ $\mathbf{a}' = \frac{1}{2}\mathbf{c}$ $\mathbf{b}' = \frac{1}{2}\mathbf{a}$ Origin at 0, y, 0
--	---	--

Maximal non-isomorphic subgroups

I	[2] $C2ce$ ($Aea2$, 41)	(1; 4; 6; 7)+
	[2] $Cm2e$ ($Aem2$, 39)	(1; 3; 6; 8)+
	[2] $Cmc2_1$ (36)	(1; 2; 7; 8)+
	[2] $C222_1$ (20)	(1; 2; 3; 4)+
	[2] $C12/c1$ ($C2/c$, 15)	(1; 3; 5; 7)+
	[2] $C112_1/e$ ($P2_1/c$, 14)	(1; 2; 5; 6)+
	[2] $C2/m11$ ($C2/m$, 12)	(1; 4; 5; 8)+
IIa	[2] $Pmnb$ ($Pnma$, 62)	1; 3; 6; 8; (2; 4; 5; 7) + $(\frac{1}{2}, \frac{1}{2}, 0)$
	[2] $Pbca$ (61)	1; 3; 5; 7; (2; 4; 6; 8) + $(\frac{1}{2}, \frac{1}{2}, 0)$
	[2] $Pbna$ ($Pbcn$, 60)	1; 2; 3; 4; (5; 6; 7; 8) + $(\frac{1}{2}, \frac{1}{2}, 0)$
	[2] $Pmca$ ($Pbcm$, 57)	1; 2; 7; 8; (3; 4; 5; 6) + $(\frac{1}{2}, \frac{1}{2}, 0)$
	[2] $Pbnb$ ($Pccn$, 56)	1; 2; 5; 6; (3; 4; 7; 8) + $(\frac{1}{2}, \frac{1}{2}, 0)$
	[2] $Pmcb$ ($Pbam$, 55)	1; 2; 3; 4; 5; 6; 7; 8
	[2] $Pbcb$ ($Pcca$, 54)	1; 4; 6; 7; (2; 3; 5; 8) + $(\frac{1}{2}, \frac{1}{2}, 0)$
	[2] $Pmna$ (53)	1; 4; 5; 8; (2; 3; 6; 7) + $(\frac{1}{2}, \frac{1}{2}, 0)$
IIb	none	

Maximal isomorphic subgroups of lowest index

IIc [3] $Cmce$ ($\mathbf{a}' = 3\mathbf{a}$) (64); [3] $Cmce$ ($\mathbf{b}' = 3\mathbf{b}$) (64); [3] $Cmce$ ($\mathbf{c}' = 3\mathbf{c}$) (64)

Minimal non-isomorphic supergroups

I none
II [2] $Fmmm$ (69); [2] $Pmcm$ ($\mathbf{a}' = \frac{1}{2}\mathbf{a}, \mathbf{b}' = \frac{1}{2}\mathbf{b}$) ($Pmma$, 51); [2] $Cmme$ ($\mathbf{c}' = \frac{1}{2}\mathbf{c}$) (67)

Appendix C: Quantitative EDS data from TEM

JEOL 2010F

Tilt series A

Quantitative Analysis					
Mon May 10 12:26:35 2010					
Filter Fit Method					
Chi-sqd = 7.05 Livetime = 6.0 Sec.					
Standardless Analysis					
Element	Net	Error			
	Counts	(1-Sigma)			
O -K	2973 +/-	128			
Ni-L	7782 +/-	183			
Nb-L	19529 +/-	353			
Ni-K	29668 +/-	330			
Nb-K	12536 +/-	399			
Metallurgical and Biological Thin Section Correction					
Acceleration Voltage =200 kV Take-off Angle = 41.60 deg					
Element	Counts	K-Rel	K-Std	Wt %	Atom %
		x,Ni	x,Ni		
Ni-K	29668	1.000	---	61.32	71.50
Nb-K	12536	1.493	---	38.68	28.50
Total				100.00	100.00

Grain 1

Wed Jun 01 17:02:01 2011

Filter Fit Method

Chi-sqd = 37.38 Livetime = 159.0 Sec.

Standardless Analysis

Element	Net	Error
	Counts	(1-Sigma)
Ni-K	95868 +/-	516
Ni-L	51503 +/-	273
Nb-K	37075 +/-	596
Nb-L	68990 +/-	504

Metallurgical and Biological Thin Section Correction

Acceleration Voltage =200 kV Take-off Angle = 41.60 deg

Element	Counts	K-Rel	K-Std	Wt %	Atom %
		x,Ni	x,Ni		
Ni-K	95868	1.000	---	63.40	73.27
Nb-K	37075	1.493	---	36.60	26.73
Total				100.00	100.00

Grain 2

Wed Jun 01 17:13:04 2011

Filter Fit Method

Chi-sqd = 133.35 Livetime = 185.0 Sec.

Standardless Analysis

Element	Net	Error
	Counts (1-Sigma)	
Ni-K	100601 +/-	533
Ni-L	59024 +/-	298
Nb-K	40031 +/-	630
Nb-L	75357 +/-	526

Metallurgical and Biological Thin Section Correction

Acceleration Voltage =200 kV Take-off Angle = 41.60 deg

Element	Counts	K-Rel	K-Std	Wt %	Atom %
		x,Ni	x,Ni		
Ni-K	100601	1.000	---	62.74	72.71
Nb-K	40031	1.493	---	37.26	27.29
Total				100.00	100.00

Grain 3

Wed Jun 01 17:45:50 2011

Filter Fit Method

Chi-sqd = 36.83 Livetime = 159.3 Sec.

Standardless Analysis

Element	Net	Error
	Counts (1-Sigma)	
Ni-K	91823 +/-	503
Ni-L	52485 +/-	275
Nb-K	32026 +/-	543
Nb-L	60232 +/-	470

Metallurgical and Biological Thin Section Correction

Acceleration Voltage =200 kV Take-off Angle = 41.60 deg

Element	Counts	K-Rel	K-Std	Wt %	Atom %
	x,Ni	x,Ni			
Ni-K	91823	1.000	---	65.76	75.25
Nb-K	32026	1.493	---	34.24	24.75
Total				100.00	100.00